CEDAR-GPP: spatiotemporally upscaled estimates of gross primary productivity incorporating CO_2 fertilization

Yanghui Kang[1,2,3], Maoya Bassiouni[1,2], Max Gaber[1,4], Xinchen Lu[1,2], Trevor F. Keenan[1,2]

[1] Department of Environmental Science, Policy, and Management, University of California, Berkeley, Berkely, CA 94720, USA

[2] Climate and Ecosystem Sciences Division, Lawrence Berkeley National Laboratory, Berkeley, CA 94720, USA

[3] Department of Biological Systems Engineering, Virginia Tech, Blacksburg, VA 24061, USA

[4] Department of Geosciences and Natural Resource Management, University of Copenhagen, Copenhagen, 1350, Denmark.

Correspondence: Yanghui Kang (yanghuikang@vt.edu)
Trevor Keenan (trevorkeenan@berkeley.edu)

Abstract: Gross primary productivity (GPP) is the largest carbon flux in the Earth system, playing a crucial role in removing atmospheric carbon dioxide and providing carbohydrates needed for ecosystem metabolism. Despite the importance of GPP, however, existing estimates present significant uncertainties and discrepancies. A key issue is the underrepresentation of the CO_2 fertilization effect, a major factor contributing to the increased terrestrial carbon sink over recent decades. This omission could potentially bias our understanding of ecosystem responses to climate change.

Here, we introduce CEDAR-GPP, the first global machine-learning-upscaled GPP product that incorporates the direct CO_2 fertilization effect on photosynthesis. Our product is comprised of monthly GPP estimates and their uncertainty at 0.05° resolution from 1982 to 2020, generated using a comprehensive set of eddy covariance measurements, multi-source satellite observations, climate variables, and machine learning models. Importantly, we used both theoretical and data-driven approaches to incorporate the direct CO_2 effects. Our machine learning models effectively predict monthly GPP ($R^2 \sim 0.72$), the mean seasonal cycles ($R^2 \sim 0.77$), and spatial variabilities ($R^2 \sim 0.63$) based on cross-validation at flux sites. After incorporating the direct CO_2 effects, predicted long-term

29   GPP trend across global flux towers substantially increases from 3.1 gC m^{-2} year^{-1} to 4.5 – 5.4 gC m^{-2}

30   year^{-1}, which aligns more closely with the 7.7 gC m^{-2} year^{-1} trend detected from eddy covariance data.

31   While the global patterns of annual mean GPP, seasonality, and interannual variability generally align

32   with existing satellite-based products, CEDAR-GPP demonstrates higher long-term trends globally

33   after incorporating CO_2 fertilization and reflected a strong temperature control on direct CO_2 effects.

34   The estimated global GPP trend is 0.57 – 0.76 PgC year^{-1} from 2001 to 2018 and 0.32 – 0.34 PgC year^{-1}

35   ^{1} from 1982 to 2020. Estimating and validating GPP trends in data-scarce regions, such as the tropics,

36   remains challenging, underscoring the importance of ongoing ground-based monitoring and

37   advancements in modeling techniques. CEDAR-GPP offers a comprehensive representation of GPP

38   temporal and spatial dynamics, providing valuable insights into ecosystem-climate interactions. The

39   CEDAR-GPP product is available at https://zenodo.org/doi/10.5281/zenodo.8212706 (Kang et al.,

40   2024).

1. Introduction

Terrestrial ecosystem photosynthesis, known as Gross Primary Productivity (GPP), is the primary source of food and energy for the Earth system and human society (Keenan and Williams, 2018). Through photosynthesis, terrestrial ecosystems also mitigate climate change, by removing thirty percent of anthropogenic carbon emissions from the atmosphere each year (Friedlingstein et al., 2023). However, due to the lack of direct measurements at the global scale, our understanding of photosynthesis and its spatiotemporal dynamics is limited, leading to considerable disagreements among various GPP estimates (Anav et al., 2015; O'Sullivan et al., 2020; Smith et al., 2016; Yang et al., 2022). Addressing these uncertainties is crucial for improving the predictability of ecosystem dynamics under climate change (Friedlingstein et al., 2014).

Over the past three decades, global networks of eddy covariance flux towers collected *in situ* carbon flux measurements that allow for accurate estimates of GPP, providing valuable insights into photosynthesis dynamics under various environmental conditions (Baldocchi, 2020; Beer et al., 2010). To quantify and understand GPP at scales and locations beyond the ~ 1km^2 flux tower footprints, machine learning has been employed with gridded satellite and climate datasets to upscale site-based measurements and produce wall-to-wall GPP maps (Dannenberg et al., 2023; Joiner and Yoshida, 2020; Jung et al., 2011; Tramontana et al., 2016; Xiao et al., 2008; Yang et al., 2007; Zeng et al., 2020). This "upscaling" approach provides data-driven and observation-based quantifications without prescribed functional relations between GPP and its climatic or environmental drivers. It offers unique empirical constraints of ecosystem carbon dynamics, complementing those derived from process-based and semi-process-based approaches such as terrestrial biosphere models or the Light Use Efficiency (LUE) models (Beer et al., 2010; Gampe et al., 2021; Jung et al., 2017; Schwalm et al., 2017). In recent years, the growth of global and regional flux networks, coupled with increasing efforts in data standardization, has offered new opportunities for the advancement of upscaling frameworks, enabling comprehensive quantifications of terrestrial photosynthesis (Joiner and Yoshida, 2020; Nelson et al., 2024; Pastorello et al., 2020).

Effective machine learning upscaling depends on a complete set of input predictors that fully explain GPP dynamics. Upscaled datasets have primarily relied on satellite-observed greenness indicators, such as vegetation indices, Leaf Area Index (LAI), the fraction of absorbed photosynthetically active radiation (fAPAR), which effectively capture canopy-level GPP dynamics related to leaf area changes (Joiner and Yoshida, 2020; Ryu et al., 2019; Tramontana et al., 2016).

However, important aspects of leaf-level physiology, such as those controlled by climate factors, are often omitted in major upscaled datasets, preventing accurate characterization of GPP responses to climate change (Bloomfield et al., 2023; Stocker et al., 2019). In particular, none of the previous upscaled datasets have considered the direct effect of atmospheric CO_2 on leaf-level photosynthesis, which is a key factor contributing to at least half of the enhanced land carbon sink observed over the past decades (Keenan et al., 2016, 2023; Ruehr et al., 2023; Walker et al., 2021). This omission can lead to incorrect inferences regarding long-term trends in various components of the terrestrial carbon cycle (De Kauwe et al., 2016).

Multiple independent lines of evidence from the atmospheric inversion (Wenzel et al., 2016), atmospheric $^{13}C/^{12}C$ measurements (Keeling et al., 2017), ice core records of carbonyl sulfide (Campbell et al., 2017), glucose isotopomers (Ehlers et al., 2015), as well as free-air CO_2 enrichment experiments (FACE) (Walker et al., 2021), suggest a widespread positive effect of elevated atmospheric CO_2 on GPP from site to global scales. Increasing atmospheric CO_2 *directly* stimulates the biochemical rate or the light use efficiency (LUE) of leaf-level photosynthesis, known as the direct CO_2 fertilization effect (CFE). Enhanced photosynthesis could lead to greater net carbon assimilation, contributing to an increase in total leaf area. This expansion, contributing to a higher light interception, further enhances canopy-level photosynthesis (i.e. GPP), which is referred to as the indirect CFE. The direct CFE has been found to dominate GPP responses to CO_2 compared to the indirect effect, from both theoretical and observational analyses (Chen et al., 2022; Haverd et al., 2020).

Satellite-based estimates have shown an increasing global GPP trend in the past few decades largely attributable to CO_2-induced increases in LAI (Chen et al., 2019; De Kauwe et al., 2016; Piao et al., 2020; Zhu et al., 2016). However, previous upscaled GPP datasets, as well as most LUE models such as the MODIS GPP product, have failed to consider the direct CO_2 effects on leaf-level biochemical processes (Jung et al., 2020; Zheng et al., 2020). Consequently, these products likely underestimated the long-term trend of global GPP, leading to large discrepancies when compared to process-based models, which typically consider both direct and indirect CO_2 effects (Anav et al., 2015; De Kauwe et al., 2016; Keenan et al., 2023; O'Sullivan et al., 2020). Notably, recent improvements in LUE models have included the CO_2 response and show improved long-term changes in GPP globally (Zheng et al., 2020), yet, this important mechanism is still missing in GPP products upscaled from *in situ* eddy covariance flux measurements based on machine learning models.

103 To improve the quantification of GPP spatial and temporal dynamics and provide a robust
104 representation of long-term dynamics in global photosynthesis, we developed the CEDAR-GPP[1] data
105 product. CEDAR-GPP was upscaled from global eddy covariance carbon flux measurements using
106 machine learning along with a broad range of multi-source satellite observations and climate variables.
107 In addition to incorporating direct CO_2 fertilization effects on photosynthesis, we also account for
108 indirect effects via greenness indicators and include novel satellite datasets such as solar-induced
109 fluorescence (SIF), Land Surface Temperature (LST) and soil moisture to explain variability under
110 environmental stresses. We provide monthly GPP estimations and associated uncertainties at 0.05°
111 resolution derived from ten model setups. These setups differ by the temporal range depending on
112 satellite data availability, the method for incorporating the direct CO_2 fertilization effects, and the
113 partitioning approach used to derive GPP from eddy covariance measurements. Short-term model
114 setups are primarily based on data derived from MODIS satellites generating GPP estimates from
115 2001 to 2020, while long-term estimates span 1982 to 2020 using combined Advanced Very High
116 Resolution Radiometer (AVHRR) and MODIS data. We used two approaches to incorporate the
117 direct CO_2 fertilization effects, including direct prescription with eco-evolutionary theory and machine
118 learning inference from the eddy-covariance data. Additionally, we provid a baseline configuration
119 that did not incorporate the direct CO_2 effects. Uncertainties in GPP estimation were quantified using
120 bootstrapped model ensembles. We evaluated the machine learning models' skills in predicting
121 monthly GPP, seasonality, interannual variability, and trend against eddy covariance measurements,
122 and compared the CEDAR-GPP spatial and temporal variability to existing satellite-based GPP
123 estimates.

124 2. Data and Methods

125 2.1 Eddy covariance data

126 We obtained monthly eddy covariance GPP measurements from 2001 to 2020 from the
127 FLUXNET2015 (Pastorello et al., 2020), AmeriFlux FLUXNET
128 (https://ameriflux.lbl.gov/data/flux-data-products/), and ICOS Warm Winter 2020 (Warm Winter
129 2020 Team, 2022) datasets. All data were processed with the ONEFLUX pipeline (Pastorello et al.,
130 2020). Following previous upscaling efforts (Tramontana et al., 2016), we selected monthly GPP data

---

[1] CEDAR stands for upsCaling Ecosystem Dynamics with ARtificial intelligence

with at least 80% of high-quality hourly or half-hourly data for temporal aggregation. High-quality data refers to GPP derived from measured or high-quality gap-filled Net Ecosystem Exchange (NEE) data. We further excluded large negative GPP values, setting a cutoff of -1 gC m^{-2} day^{-1}. We utilized GPP estimates from both the night-time (GPP_REF_NT_VUT) and day-time (GPP_REF_DT_VUT) partitioning approaches. We classified flux tower sites according to the C3 and C4 plant categories reported in metadata and related publications when available and used a C4 plant percentage map (Still et al., 2003) otherwise. This classification information is included in Supplementary Text S1. Our analysis encompassed 233 sites, predominantly located in North America, Western Europe, and Australia (Figure 1). A list of the sites is provided in Appendix A. Despite their uneven geographical distribution, these sites effectively cover a diverse range of climatic conditions and are representative of global biomes (Figure 1c, 1d). In total, our dataset included over 18000 site-months. Note that we did not include eddy covariance data before 2001, since it was limited to only a few sites with only four sites containing data before 1996. This scarcity might introduce biases in the machine learning models, particularly in the relationship between GPP and CO$_2$, leading to unreliable extrapolations across space and time in the long-term predictions.
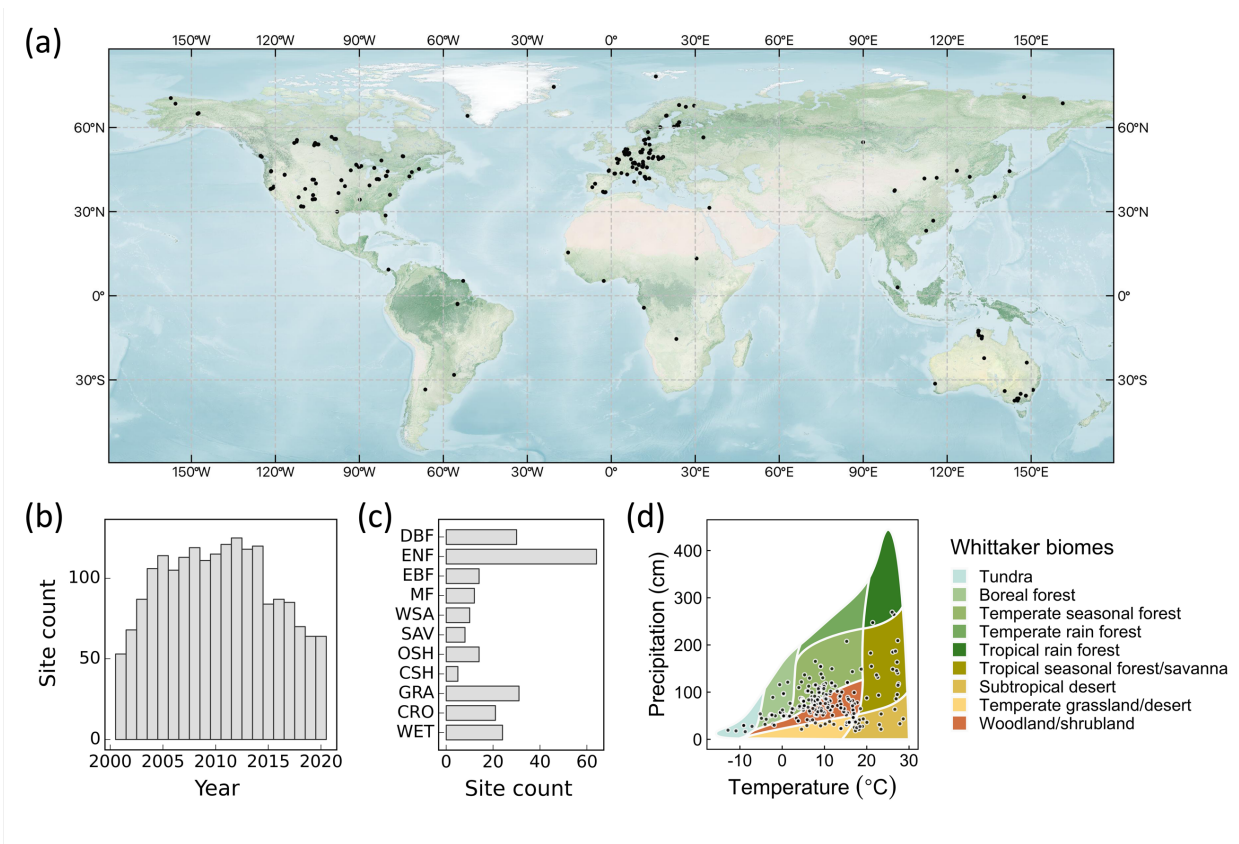
147 Figure 1. (a) Spatial distribution of eddy covariance sites used to generate the CEDAR-
148 GPP product. (b) Annual site counts. (c) Site counts by biomes. ENF: evergreen
149 needleleaf forests, EBF: evergreen broadleaf forests, DBF: deciduous broadleaf forests,
150 MF: mixed forests, WSA: woody savannas, SAV: savannas, OSH: open shrublands,
151 CSH: closed shrublands, GRA: grasslands, CRO: croplands, WET: wetlands. (d) Sites
152 distributions in the annual temperature and precipitation space. Whittaker biome
153 classification is shown as a reference of natural vegetation based on long-term climatic
154 conditions. It does not directly indicate the actual biome associated with each site. The
155 base map in (a) was obtained from the NASA Earth Observatory map by Joshua
156 Stevens using data from NASA's MODIS Land Cover, the Shuttle Radar Topography
157 Mission (SRTM), the General Bathymetric Chart of the Oceans (GEBCO), and
158 Natural Earth boundaries. Whittaker biomes were plotted using the "plotbiomes" R
159 package (Ștefan and Levin, 2018).

2.2 Global input datasets

161   We compiled an extensive set of covariates from gridded climate reanalysis data, multi-source

162 satellite datasets including optical, thermal, and microwave observations, as well as categorical

163 information on land cover, climate zone, and C3/C4 classification. The datasets that we compiled

164 offer comprehensive information about GPP dynamics and its responses to climatic variabilities and

165 stresses. Table 1 lists the datasets and associated variables used to generate CEDAR-GPP.

166 Table 1. Datasets used in different model setups to generate the CEDAR GPP product. Refer to Table
167 S1 for a list of specific variables from each dataset.

Category	Dataset	Temporal coverage	Spatial resolution	Temporal resolution	Usage in model setups		Reference
					Short-term	Long-term	
Climate	ERA5-Land	1950 – present	0.1°	Monthly	✓	✓	(Sabater, 2019)
	ESRA Global Monitoring Laboratory Atmospheric Carbon Dioxide	1976 – present	-	Monthly	✓	✓	(Thoning et al., 2021)
Satellite-based datasets	MODIS Nadir BRDF-adjusted reflectance (MCD43C4v006)	2000 – present	0.05°	Daily	✓		(Schaaf and Wang, 2015)
	MODIS Terra and Aqua LAI/fPAR (MCD15A3H, MOD15A2H, v006)	2000 – present	500m	4-day, 8-day	✓		(Myneni et al., 2015a, b)
	MODIS Terra and Aqua LST (MYD11A1, MOD11A1, v006)	2000 – present	1 km	Daily	✓		(Wan et al., 2015b, a)
	BESS_Rad	2000 – 2020	0.05°	Daily	✓		(Ryu et al., 2018)
	Continuous-SIF (from OCO-2 and MODIS)	2000 – 2020	0.05°	4-day	✓		(Zhang, 2021)
	ESA CCI Soil Moisture Combined Passive and Active v06.1	1979 – 2021	0.25°	Daily	✓		(Gruber et al., 2019)
	GIMMS LAI4g	1982 – 2021	0.0833°	Half-month		✓	(Cao et al., 2023)
	GIMMS NDVI4g	1982 – 2021	0.0833 °	Half-month		✓	(Li et al., 2023b)
Static categorical datasets	MODIS Land Cover (MCD12Q1v006)	Average status used between 2001 and 2020	500m	-	✓	✓	(Friedl and Sulla-Menashe, 2019)
	Koppen-Geiger Climate Classification	present	1 km	-	✓	✓	(Beck et al., 2018)
	C4 percentage map	present	1°	-	✓	✓	(Still et al., 2003, 2009)

168

169

2.2.1 Climate variables

We obtained air temperature, vapor pressure deficit, precipitation, potential evapotranspiration, and skin temperature from the EAR5-Land reanalysis dataset (Sabater, 2019) (Table 1; Table S1). We applied a three-month lag to precipitation, to reflect the memory of soil moisture and represent the root zone water availability. Averaged monthly atmospheric CO_2 concentrations were calculated as an average of records from the Mauna Loa Observatory and South Pole Observation stations, retrieved from NOAA's Earth System Research Laboratory (Thoning et al., 2021).

2.2.2 Satellite datasets

We assembled a broad collection of satellite-based observations of vegetation greenness and structure, LST, solar radiation, solar-induced fluorescence (SIF), and soil moisture (Table 1, Table S1).

We used three MODIS version 6 products: surface reflectance, LAI/fAPAR, and LST. Surface reflectance from optical to infrared bands (band 1 to 7) was sourced from the MODIS Nadir BRDF-adjusted reflectance (NBAR) daily dataset (MCD43C4) (Schaaf and Wang, 2015). From these data, we derived vegetation indices, including NIRv (Badgley et al., 2019), kNDVI (Camps-Valls et al., 2021), NDVI, Enhanced Vegetation Index (EVI), Normalized Difference Water Index (NDWI) (Gao, 1996), and the green chlorophyll index (CIgreen) (Gitelson, 2003). We also used snow percentages from the NBAR dataset. We used the 4-day LAI and fPAR composite derived from Terra and Aqua satellites (MCD15A3H) (Myneni et al., 2015a; Yan et al., 2016a, b) from July 2002 onwards and the MODIS 8-day LAI and fPAR dataset from Terra only (MOD15A2H) prior to July 2002 (Myneni et al., 2015b). We used day-time and night-time LST from the Aqua satellite (MYD11A1) (Wan et al., 2015b), with the Terra-based LST product (MOD11A1) used after July 2002 (Wan et al., 2015a). Terra LST was bias-corrected with the differences in the mean seasonal cycles between Aqua and Terra following Walther et al. (2022).

We used the PKU GIMMS NDVI4g dataset (Li et al., 2023b) and PKU GIMMS LAI4g (Cao et al., 2023) datasets available from 1982 to 2020. PKU GIMMS NDVI4g is a harmonized time series that includes AVHRR-based NDVI from 1982 to 2003 (with biases and corrections mitigated through inter-calibration with Landsat surface reflectance images) and MODIS NDVI from 2004 onward. PKU GIMMS LAI4g consisted of consolidated AVHRR-based LAI from 1982 to 2003 (generated using machine learning models trained with Landsat-based LAI data and NDVI4g) and reprocessed MODIS LAI (Yuan et al., 2011) from 2004 onwards.

200   We utilized photosynthetically active radiation (PAR), diffusive PAR, and shortwave

201   downwelling radiation from the BESS_Rad dataset (Ryu et al., 2018). We obtained the continuous-

202   SIF (CSIF) dataset (Zhang, 2021; Zhang et al., 2018) produced by a machine learning algorithm trained

203   using OCO-2 SIF observations and MODIS surface reflectance. We used surface soil moisture from

204   the ESA CCI soil moisture combined passive and active product (version 6.1) (Dorigo et al., 2017;

205   Gruber et al., 2019).

206   2.2.3   Other categorical datasets

207   We used plant functional type (PFT) information derived from the MODIS Land Cover product

208   (MCD12Q1) (Friedl and Sulla-Menashe, 2019). We followed the International Geosphere-Biosphere

209   Program classification scheme but merged several similar categories to maximize the amount of eddy

210   covariance sites/observations available for each category. Closed shrublands and open shrublands are

211   combined into a shrubland category. Woody savannas and savannas are combined into savannas. We

212   generated a static PFT map by taking the mode of the MODIS land cover time series between 2001

213   – 2020 at each pixel to mitigate uncertainties from misclassification in the MODIS dataset.

214   Nevertheless, changes in vegetation structure induced by land use and land cover change are reflected

215   in the dynamics surface reflectance and LAI/fAPAR datasets we used. We used the Koppen-Geiger

216   main climate groups (tropical, arid, temperate, cold, and polar) (Beck et al., 2018). We also utilized a

217   C4 plant percentage map to account for different photosynthetic pathways when incorporating CO_2

218   fertilization (Still et al., 2003, 2009). The C4 percentage dataset was constant over time.

219   2.2.4   Data preprocessing

220   We implemented a three-step preprocessing strategy for the satellite datasets: 1) quality control,

221   2) gap-filling, and 3) spatial and temporal aggregation. Firstly, we selected high-quality data based on

222   the quality control flags of the satellite products when available. For the MODIS NBAR dataset

223   (MCD43C3), we used data with 75% or more high-resolution NBAR pixels retrieved with full

224   inversions for each band. For MODIS LST, we selected the best quality data from the quality control

225   bitmask as well as data where retrieved values had an average emissivity error of no more than 0.02.

226   For MODIS LAI/fAPAR, we used retrievals from the main algorithm with or without saturation. We

227   used all available data in ESA-CCI soil moisture due to the presence of substantial data gaps. In the

228   gap-filling step, missing values in satellite datasets were temporally filled at the native temporal

229   resolution, following a two-step protocol adapted from Walther et al (2021). Short temporal gaps were

230   first filled with medians from a moving window, and the remaining gaps were filled with the mean

231 seasonal cycle. For datasets with a high temporal resolution, including MODIS NBAR (daily),
232 LAI/fPAR (4-day), BESS (4-day), CSIF (4-day), ESA-CCI (daily), temporal gaps no longer than 5 days
233 (8 days for 4-day resolution products) were filled with medians of 15-day moving windows in the first
234 step. An exception is MODIS LST (daily), for which we used a shorter moving window of 9 days due
235 to rapid changes in surface temperature. GIMMS LAI4g and NDVI4g data were only filled with mean
236 seasonal cycle due to their low temporal resolution (half-month). This is because vegetation structure
237 could experience significant changes at half-month intervals, and gap-filling using temporal medians
238 within moving windows could introduce considerable uncertainties and potentially over-smooth the
239 time series.

240 Finally, all the datasets were aggregated to a monthly time step and 0.05-degree spatial resolution.
241 We employed the conservative resampling approach using the xESMF python package (Zhuang et al.,
242 2023). To generate the machine learning model training data, we extracted values from the nearest
243 0.05 degree pixel relative to the site locations within the gridded dataset.

244
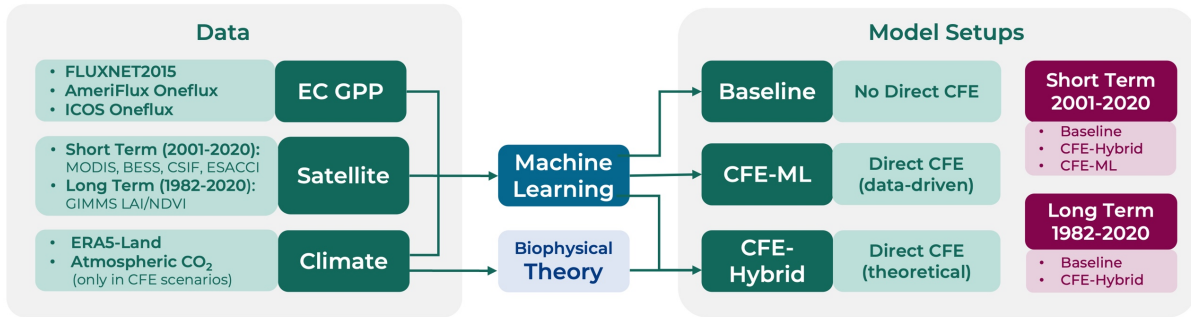
245 Figure 2. Schematic overview of the CEDAR-GPP model setups.

2.3 Machine learning upscaling

2.3.1 CEDAR-GPP model setups

248 We trained machine learning models with eddy covariance GPP measurements as targets and
249 climate/satellite variables as input features. We created ten model setups to produce different global
250 monthly GPP estimates (Figure 2; Table 2). The model setups were characterized by the temporal
251 range depending on input data availability, the configuration of CO_2 fertilization effects, and the
252 partitioning approach used to derive the GPP from eddy covariance measurements.

253 The short-term (ST) model configuration produced GPP from 2001 to 2020, and the long-term
254 (LT) configuration spanned 1982 to 2020. Each temporal configuration uses a different set of input
255 variables depending on their availability. Inputs for the short-term configuration included MODIS,

CSIF, BESS PAR, ESA-CCI soil moisture, ERA5-Land, as well as PFT and Koppen Climate zone as categorical variables with one-hot encoding. The long-term used GIMMS NDVI4g and LAI4g data, ERA5-land, PFT and Koppen climate. ESA CCI soil moisture datasets were excluded from the long-term model setups due to concerns about the product quality in the early years when the number and quality of microwave satellite data were limited (Dorigo et al., 2015). A detailed list of input features for each setup is provided in Table S1.

Regarding the direct CO_2 fertilization effects (CFE), we established a "Baseline" configuration that did not incorporate these effects, a "CFE-Hybrid" configuration that incorporated the effects via eco-evolutionary theory, and a "CFE-ML" configuration that inferred the direct effects from eddy covariance data using machine learning. Detailed information about these approaches is provided in Sec. 2.3.2. Furthermore, separate models were trained for GPP target variables from the night-time (NT) and daytime (DT) partitioning approaches.

Table 2 lists the characteristics of ten model setups. Due to the limited availability of eddy covariance observations before 2001, we did not apply the CFE-ML approach to the long-term setups. The CFE-ML model, when trained on data from 2001 to 2020 with atmospheric CO_2 ranging from 370 to 412 ppm, would not accurately predict GPP response to CO_2 for the period 1982 – 2000 when the CO2 levels were markedly lower (340 – 369 ppm). This is because machine learning models, especially tree-based models, could not extrapolate beyond the range of the training data.

Table 2. Specifications of the CEDAR-GPP model setups.

Model Setup Name	Temporal range	Direct CO_2 Fertilization Effects		GPP Partitioning Method
		Configuration	Method	
ST_Baseline_NT	Short-term (ST) 2001 – 2020	Baseline	Not incorporated	Night-time (NT)
ST_Baseline_DT				Day-time (DT)
ST_CFE-Hybrid_NT		CFE-Hybrid	Theoretical	NT
ST_CFE-Hybrid_DT				DT
ST_CFE-ML_NT		CFE-ML	Data-driven	NT
ST_CFE-ML_DT				DT
LT_Baseline_NT	Long-term (LT) 1982 – 2020	Baseline	Not incorporated	NT
LT_Baseline_DT				DT
LT_CFE-Hybrid_NT		CFE-Hybrid	Theoretical	NT
LT_CFE-Hybrid_DT				DT

2.3.2 CO_2 fertilization effect

We established three configurations regarding the direct CO_2 fertilization effects on photosynthesis. In the baseline configuration, we trained machine learning models with eddy

279 covariance GPP measurements, input climate and satellite features, but excluding CO_2 concentration.

280 As such, the models only include indirect CO_2 effects from the satellite-based proxies of vegetation

281 greenness or structure representing changes in canopy light interception, and they do not consider the

282 direct effect of CO_2 on leaf-level photosynthetic rates (or light use efficiency, LUE). Our baseline

283 model is therefore directly comparable to other satellite-derived GPP products that only account for

284 indirect CO2 effects (Joiner and Yoshida, 2020; Jung et al., 2020).

285 In the CFE-ML configuration, we added monthly CO_2 concentration into the feature set in

286 addition to those incorporated in the baseline models. Models inferred the functional relationship

287 between GPP and CO_2 from the eddy covariance data. They thus encompass both CO_2 fertilization

288 pathways – direct effects on LUE and indirect effects from the satellite-based proxies of vegetation

289 greenness and structure.

290 In the CFE-Hybrid configuration, we applied biophysical theory to estimate the response of

291 LUE to elevated CO_2, i.e. the direct CFE (Appendix A). First, we estimated a reference GPP, where

292 LUE was not affected by any increase in atmospheric CO_2, by applying the CFE-ML model with a

293 constant atmospheric CO_2 concentration equal to the 2001 level while keeping all other variables

294 temporally dynamic. Then, the impacts of CO_2 on LUE were prescribed onto the reference GPP

295 estimates using a theoretical CO_2 sensitivity function of LUE according to the optimal coordination

296 theory (Appendix A). The theoretical CO_2 sensitivity function represents a CO_2 sensitivity that is

297 equivalent to that of the electron-transport-limited (light-limited) photosynthetic rate. When light is

298 limited, elevated CO_2 suppresses photorespiration leading to increased photosynthesis at a lower rate

299 than when photosynthesis is limited by CO_2 (Lloyd and Farquhar, 1996; Smith and Keenan, 2020).

300 Thus, the CFE-Hybrid scenario provides a conservative estimation of the direct CO_2 effects on LUE.

301 Note that the theoretical sensitivity function describes the fractional change in LUE due to direct CO_2

302 effects relative to a reference period (i.e. 2001). Therefore, we used the CFE-ML model to establish

303 this reference GPP by fixing the CO_2 effects to the 2001 level, rather than simply using the GPP from

304 the Baseline model in which the direct CO_2 effects were not represented. Long-term trends from the

305 reference and the Baseline models are consistent.

306 For both CFE-ML and CFE-Hybrid scenarios, we made another conservative assumption that

307 C4 plants do not benefit from elevated CO_2, despite potential increases in photosynthesis during

308 water-limited conditions due to enhanced water use efficiency (Walker et al., 2021). Data from flux

309 tower sites dominated by C4 plants were removed from our training set, so the machine learning

310 models inferred CO_2 fertilization only from flux tower sites dominated by C3 plants. When applying

311 models globally, we assumed the reference GPP values (with constant atmospheric CO_2 concentration

312 equal to the 2001 level) to represent C4 plants, and GPP estimates from CFE-ML or CFE-Hybrid

313 models were applied in proportion to the percentage of C3 plants in a grid cell.

314 ### 2.3.3   Machine learning model training and validation

315 We employed the state-of-the-art XGBoost machine learning model, known for its high

316 accuracy in regression problems across various domains, including environmental and ecological

317 predictions (Berdugo et al., 2022; Chen and Guestrin, 2016; Kang et al., 2020). XGBoost is a scalable

318 and parallelized implementation of the gradient boosting technique that iteratively trains an ensemble

319 of decision trees, with each iteration targeting to minimize the residuals from the last iteration. A

320 notable merit of XGBoost is its ability to make predictions in the presence of missing values, a

321 common issue in remote sensing datasets. Without relying on prior assumptions about the functional

322 forms or statistical distributions, the model is also robust to multi-collinearity between the predictors

323 in our dataset, particularly for the variables derived from MODIS data.

324 We used five-fold cross-validation for model evaluation. Training data was randomly split into

325 five groups (folds), with each fold held out for testing while the rest four folds were used for model

326 training. We imposed two restrictions on fold splitting: each flux site was entirely assigned to a fold to

327 test model performance over unseen locations; the random sampling was stratified based on PFT to

328 ensure coverage of the full range of PFTs in both training and testing. We also used a nested-cross-

329 validation strategy, during which we performed a randomized search of hyperparameters using three-

330 fold cross-validation within the training set. The nested-cross-validation was aimed to reduce the risk

331 of overfitting and improve the robustness of the evaluation.

332 We assessed the models' ability to capture the temporal and spatial characteristics of GPP,

333 including monthly GPP, mean seasonal cycles, monthly anomalies, and cross-site variability. Model

334 performance was assessed separately for each model setup (Table 2) and summarized by PFT and

335 Koppen climate zone. Mean seasonal cycles were calculated as the mean monthly GPP over the site

336 observation period, and monthly anomalies were the residuals of monthly GPP after subtracting mean

337 seasonal cycles. Monthly GPP averaged over years for each site was used to assess cross-site variability.

338 Goodness-of-fit metrics include RMSE, bias, and coefficient of determination (R^2).

339 To evaluate the models' ability to capture long-term GPP trends, we aggregated the monthly

340 GPP to annual values following Chen et al. (2022) , which detected the CO_2 fertilization effect across

341 global eddy covariance sites. For sites with at least five years of observations, GPP anomalies were

computed by subtracting the multi-year mean GPP from the annual GPP for each site. Anomalies were aggregated across sites to achieve a single multi-site GPP anomaly per year. We excluded a site-year if less than 11 months of data was available and used linear interpolation to fill the remaining temporal gaps. This resulted in 81 sites used in the GPP trend evaluation. We used the Sen slope and Mann-Kendall test to examine the GPP trends from 2002 to 2019, excluding 2001 and 2020, due to the limited number of available sites with more than five years of data. We further assessed the aggregated annual trend by grouping the sites based on plant functional types and the Koppen climate zones. Categories with less than six long-term sites available were excluded from the analysis, which includes EBF and Tropics.

To further analyze GPP responses to CO_2 in the CFE-ML models, we leveraged two explainable machine learning approaches: ALE (Accumulated Local Effects) (Apley and Zhu, 2020; Baniecki et al., 2021) and SHAP (SHapley Additive exPlanations) (Lundberg and Lee, 2017). SHAP is a model interpretation method derived from game theory, providing a value for each feature's contribution to a prediction, elucidating how each feature impacts the model's output in a specific instance. Conversely, ALE quantifies the average effect of a feature across the data, isolating its impact by aggregating local effects and avoiding the biases associated with correlated features.

2.3.4   Product generation and uncertainty quantification

In the CEDAR-GPP product, we generated GPP estimates from each of the ten model setups, by applying the model to global gridded datasets within the corresponding temporal range (Table 2). GPP estimates were named after the corresponding model setups. We used bootstrapping to estimate prediction uncertainties. For each model setup, we generated 30 bootstrapped sample sets of eddy covariance data, which were then used to train an ensemble of 30 XGBoost models. The bootstrapping was performed at the site level, and each bootstrapped sample set contained around 140 to 150 unique sites, 17000 to 19000 site months covering all PFTs. The relative PFT composition in the bootstrapped sample sites was consistent with the full dataset. Hyperparameters of the XGBoost models used in the final product generation were described in Supplementary Text S2. The 30 models trained with bootstrapped samples generated an ensemble of 30 GPP values. We provided the ensemble GPP mean and used standard deviation to indicate uncertainties, for each of the ten model setups.

2.4 Product inter-comparison

We compared the global spatial and temporal patterns of CEDAR-GPP with other major satellite-based GPP products, including three machine learning upscaled and two LUE-based datasets. We obtained two FLUXCOM products (Jung et al., 2020), the latest version of FLUXCOM-RS (FLUXCOM-RSv006) available from 2001 to 2020 based on remote sensing (MODIS collection 6) datasets only, as well as the FLUXCOM-RS+METEO ensemble available between 1979 to 2018 and based on the climatology of remote sensing observations and ERA5 forcings (hereafter FLUXCOM-ERA5). We used FluxSat (Joiner and Yoshida, 2020), available from 2001 to 2019, which is an upscaled dataset based on MODIS NBAR surface reflectance and PAR from Modern-Era Retrospective analysis for Research and Applications 2 (MERRA-2). Importantly, FluxSat does not incorporate climate forcings. We used the MODIS GPP product (MOD17) available since 2001, which was generated based on MODIS fAPAR and LUE as a function of air temperature and vapor pressure deficit but not atmospheric CO_2 concentration (Running et al., 2015). We also used the rEC-LUE products, available from 1982 to 2018 and based on a revised LUE model that incorporated the effect of atmospheric CO_2 concentration and the fraction of diffuse PAR on LUE (Zheng et al., 2020). Additionally, to evaluate GPP trends, we compared our product against three process-based models forced by remote sensing data – BEPS (Leng et al., 2024), BESSv2 (Li et al., 2023a), and PML V2 (Zhang et al., 2019). These products estimate GPP by scaling leaf-level biochemical photosynthesis models to the canopy level, using satellite-derived vegetation structural variables such as LAI. All three products incorporate the direct CO_2 effects within their biochemical photosynthesis models.

All datasets were resampled to 0.1 ° spatial resolution, and a common mask for the vegetated land area was applied. We evaluated global mean annual GPP, mean seasonal cycle, interannual variability, and trend among different datasets, comparing them over a common time period determined by their data availability. Global total GPP was computed by scaling the global area-weighted average GPP flux with the global land area (122.4 million km^2) following Jung et al. (2020). Mean seasonal cycle was defined as above (Sec. 2.3.3). We used the standard deviation of annual GPP to indicate the magnitude of interannual variability, the Sen slope to indicate the GPP annual trend, and the Mann-Kendall test for the statistical significance of trends.

3. Results

3.1 Evaluation of model performance

3.1.1 Overall performance

The short-term and long-term models explain approximately 72% and 67%, respectively, of the variation in monthly GPP across global eddy covariance sites (Figure 3a). The long-term models consistently yield lower performance than the short-term models, likely due to differences in the satellite remote sensing datasets used, as the short-term models benefited from richer information from surface reflectance of individual bands, LST, CSIF, as well as soil moisture, while the long-term model only exploited NDVI and LAI. The models with different CFE configurations and target GPP variables (i.e. partitioning approaches) have similar performance in predicting monthly GPP (Figure 3b, Table S2). All models exhibit minimal bias of less than 0.1.

Model performance in terms of the different temporal and spatial characteristics of monthly GPP is variable (Figure 3c-h). The models are most successful at predicting mean seasonal cycles, with the short-term and long-term models explaining around 77% and 72% of the variability, respectively (Figure 3c-d). The short-term and long-term models capture 63% and 54% , respectively, of the spatial variabilities in multi-year mean GPP across global sites (i.e., cross-site variability) (Figure 3g-h). However, all models underestimate monthly anomalies across the sites, with R^2 values below 0.12 (Figure 3e-f). Patterns from the DT setups do not significantly differ from those of the NT setups (Figure S1, Table S2). Model performance also varies across sites, and models are more advantageous in explaining mean seasonal cycles than monthly anomalies in most sites (Figure S2).
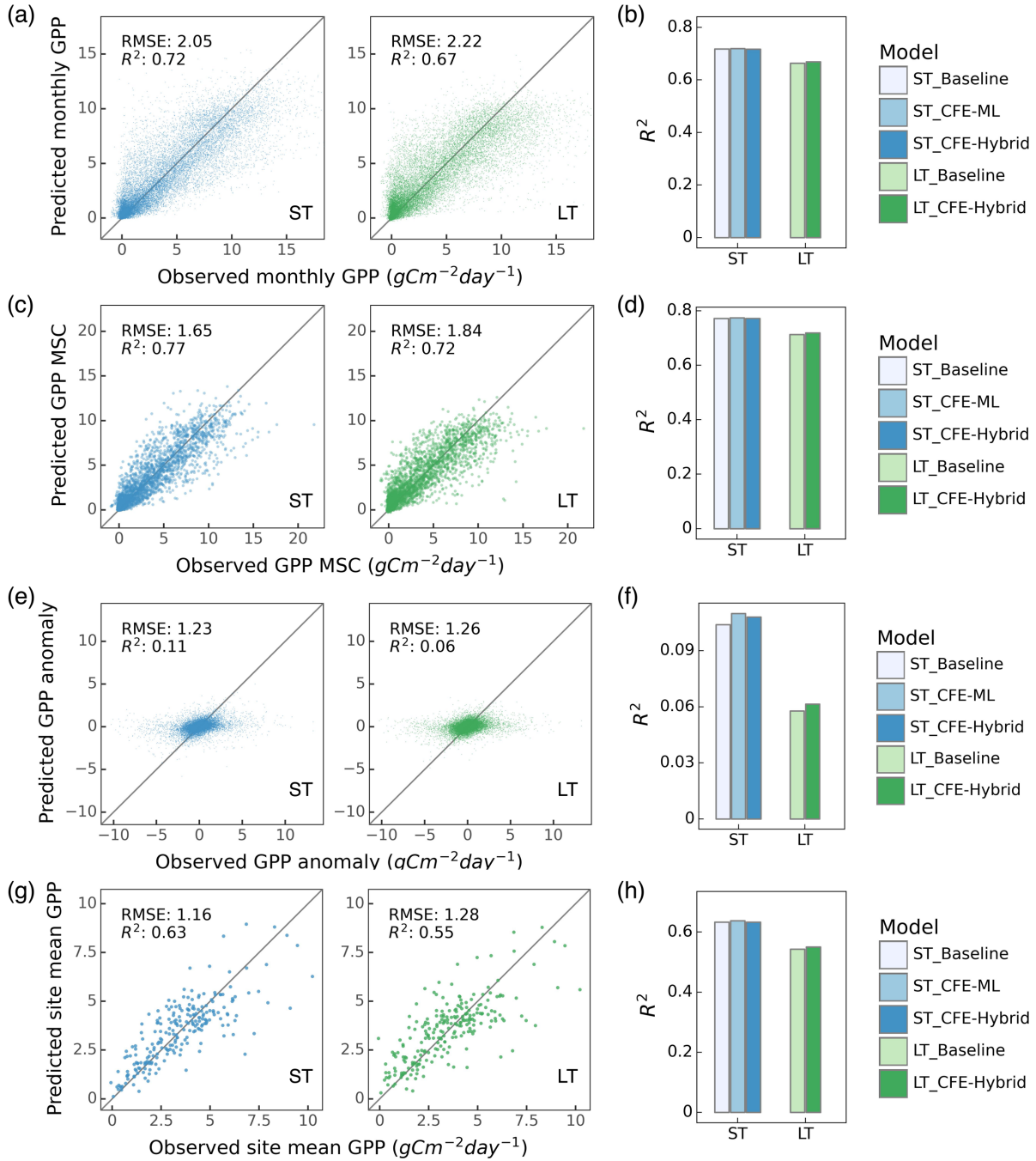
Figure 3. Machine learning model performance in predicting monthly GPP and its spatial and temporal variability. Only NT models are shown and DT results are provided in Supplementary Figure S1. Scatter plots illustrated relationships between model predictions and observations for monthly GPP (a), mean seasonal cycles (MSC) (c), monthly anomaly (e), and cross-site variability (g) for ST_CFE-Hybrid_NT (left, blue) and LT_CFE-Hybrid_NT (right, green) models. Corresponding bar plots show the R² values for five NT model setups in predicting monthly GPP (b), MSC (d), monthly anomaly (f), and cross-site variability (h).

429   3.1.2   Performance by biome and climate zone

430   The predictive ability of our models varies across different PFTs and Koppen climate zones

431   (Figure 4). Here we present results from the CFE-Hybrid LT and ST models based on NT partitioning

432   and note that patterns for the other CFE configurations and the DT GPP were similar (Figure S3, S4,

433   S5).

434   Model performance in terms of monthly GPP is the highest for deciduous broadleaf forests,

435   mixed forests, and evergreen needleleaf forests, with R^2 values above 0.76. Model accuracies are also

436   high for savannas and grasslands, followed by croplands and wetlands, with R^2 values between 0.48

437   and 0.76. Model accuracies are lowest in evergreen broadleaf forests and shrublands, with R^2 values

438   as low as 0.13. Across climate zones, models achieve the highest accuracy in predicting monthly GPP

439   in cold climates with R^2 around 0.73 – 0.78, followed by tropics and temperate zones ($R^2 \sim 0.47$ –

440   0.65). The short-term models have the lowest performance in polar regions with an R^2 value of around

441   0.37, and the long-term models have the lowest performance in arid regions with an R^2 value of 0.28.

442   Interestingly, short-term and long-term models exhibit substantial differences in arid regions and

443   shrublands marked by strong seasonality and interannual variabilities.

444   Model performance in terms of mean seasonal cycles across PFTs and climate zones follows

445   patterns for monthly GPP, while disparities emerge for performance in terms of GPP anomaly and

446   cross-site variability (Figure 4, Figure S3, S4, S5). The short-term model shows the highest predictive

447   power in explaining monthly anomalies in arid regions with an R^2 value of 0.48, where savanna and

448   shrublands sites are primarily located. Model performance in all other climate zones is significantly

449   lower. The short-term model also demonstrates good performance in capturing anomalies in

450   deciduous broadleaf forests. The long-term model's relative performance between PFTs and climate

451   zones is mostly consistent with that of the short-term model, with lower accuracy in shrublands when

452   compared to the short-term model.

453   Models demonstrate the highest accuracy in predicting cross-site variability in savannas,

454   grasslands, evergreen needleleaf forests, and evergreen broadleaf forests ($R^2 > 0.36$) and the lowest

455   accuracy in deciduous broadleaf forests, mixed forests, and croplands ($R^2 < 0.1$). The short-term

456   model additionally shows good performance in shrublands and wetlands ($R^2 > 0.36$), whereas the

457   long-term model fails to capture any variability for shrublands. In terms of climate zones, models are

458   most successful at explaining the variabilities within tropical and cold climate zones ($R^2 > 0.50$), the

459   short-term model has moderate performance in temperature and polar regions ($R^2 \sim 0.22$), and the

460   long-term model has low performance for both temperate and arid regions with R^2 values below 0.16.
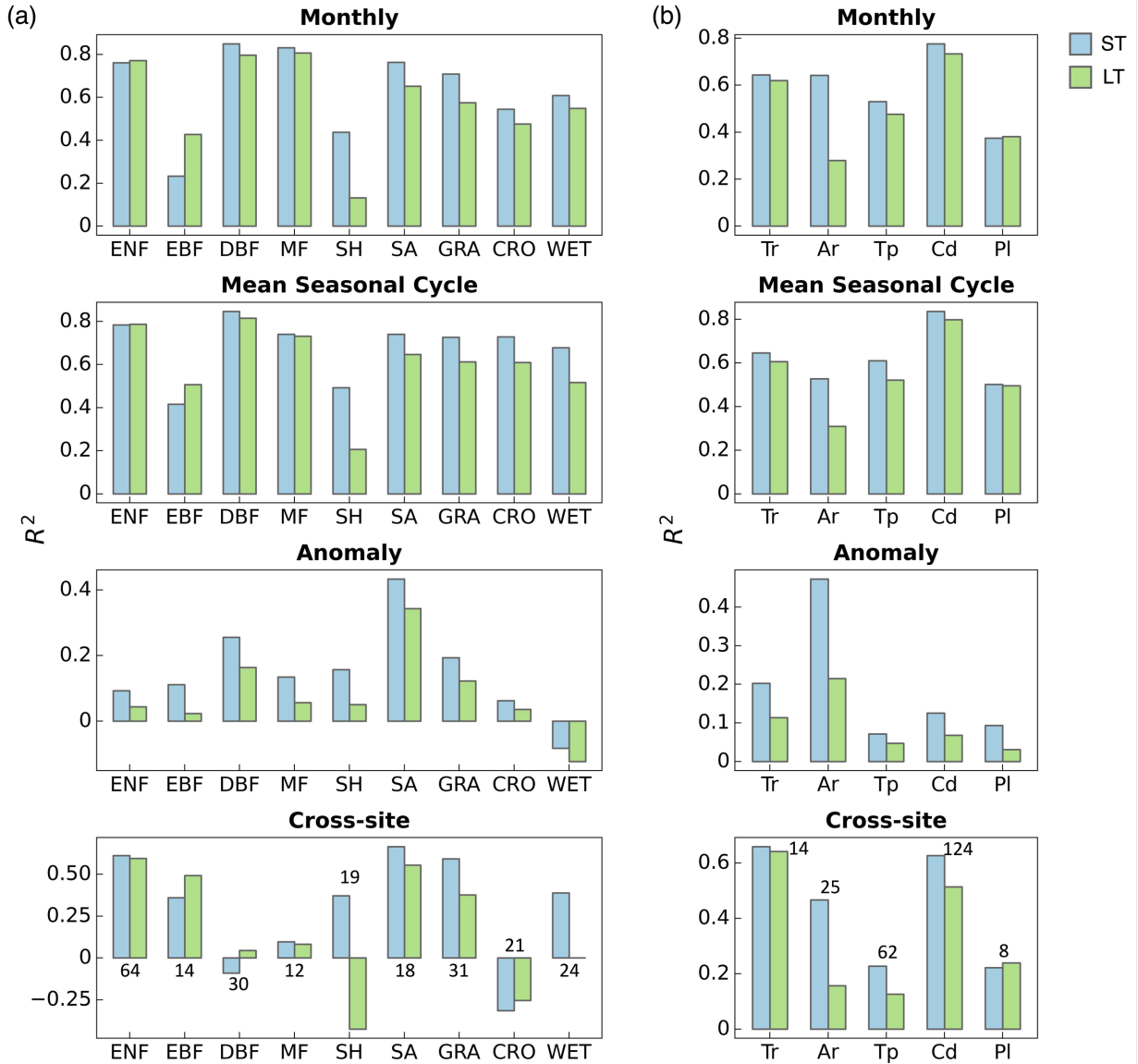
Figure 4. Performance of the ST_CFE-Hybrid_NT (blue) and LT_CFE-Hybrid_NT (green) models on GPP spatiotemporal estimation by plant functional types (a) and climate zones (b). The cross-site panels included the number of sites within each category. Color indicates short-term (ST) or long-term (LT) models. ENF: evergreen needleleaf forest, EBF: evergreen broadleaf forest, DBF: deciduous broadleaf forest, MF: mixed forest, SH: shrubland, SA: savanna, GRA: grassland, CRO: cropland, WET: wetland. Tr: tropical, Ar: arid, Tp: temperate, Cd: cold, Pl: polar. The performance of DT models is displayed in Supplementary Figure S3.

3.1.3 Prediction of long-term trends

Eddy covariance derived GPP presents a substantial increasing trend across flux sites between 2002 and 2019 (Figure 5a, Figure S6a). The eddy covariance GPP from the night-time partitioning

473   approach indicates an overall trend of 7.7 gC m^{-2} $year^{-2}$. In contrast, the ST_ Baseline_NT model

474   predictes a more modest overall trend of 3.1 gC m^{-2} $year^{-2}$ across the flux sites, primarily reflecting the

475   indirect CO_2 effect manifested through the growth of LAI. Both the ST_CFE-ML_NT and ST_CFE-

476   hybrid_NT models predicte much higher trends of 5.4 and 4.5 gC m^{-2} $year^{-2}$ respectively, representing

477   an improvement from the Baseline model by 74% and 45%, aligning more closely to eddy covariance

478   observations. Similarly, the LT_CFE-Hybrid_NT model shows an improved trend estimation than

479   the LT_Baseline_NT model. All trends were statistically significant ($p < 0.05$).

480   Aggregated eddy covariance GPP experiences increasing trends of varied magnitudes across different

481   climate zones and plant functional types (Figure 5b,c; Figure S6b,c). While the machine learning

482   models generally do not fully capture the enhancement in GPP for most categories, the CFE-ML

483   and/or CFE-hybrid models consistently outperform the Baseline models in both ST and LT setups.

484   The CFE-ML setup predicts a higher trend than CFE-hybrid in most cases, suggesting that the data-

485   driven approach captures more dynamics not represented in the theoretical model, which is based on

486   conservative assumptions regarding the CO_2 sensitivity of photosynthesis (see Sect. 2.3.2 and

487   Appendix A). The choice of remote sensing data (ST vs. LT configurations) does not lead to

488   substantial differences in the predicted GPP trend. Most long-term flux sites (at least 10 years of

489   records) with a significant trend experienced an increase in GPP, and the CFE-ML and/or CFE-

490   hybrid models align closer to eddy covariance data than the Baseline models (Figure S7). Additionally,

491   we found a considerably higher trend in eddy covariance GPP measurements derived from the day-

492   time versus night-time partitioning approach, potentially associated with uncertainties in GPP

493   partitioning methods (Figure S6). Yet, machine learning model predicted trends are not strongly

494   affected by GPP partitioning methods.
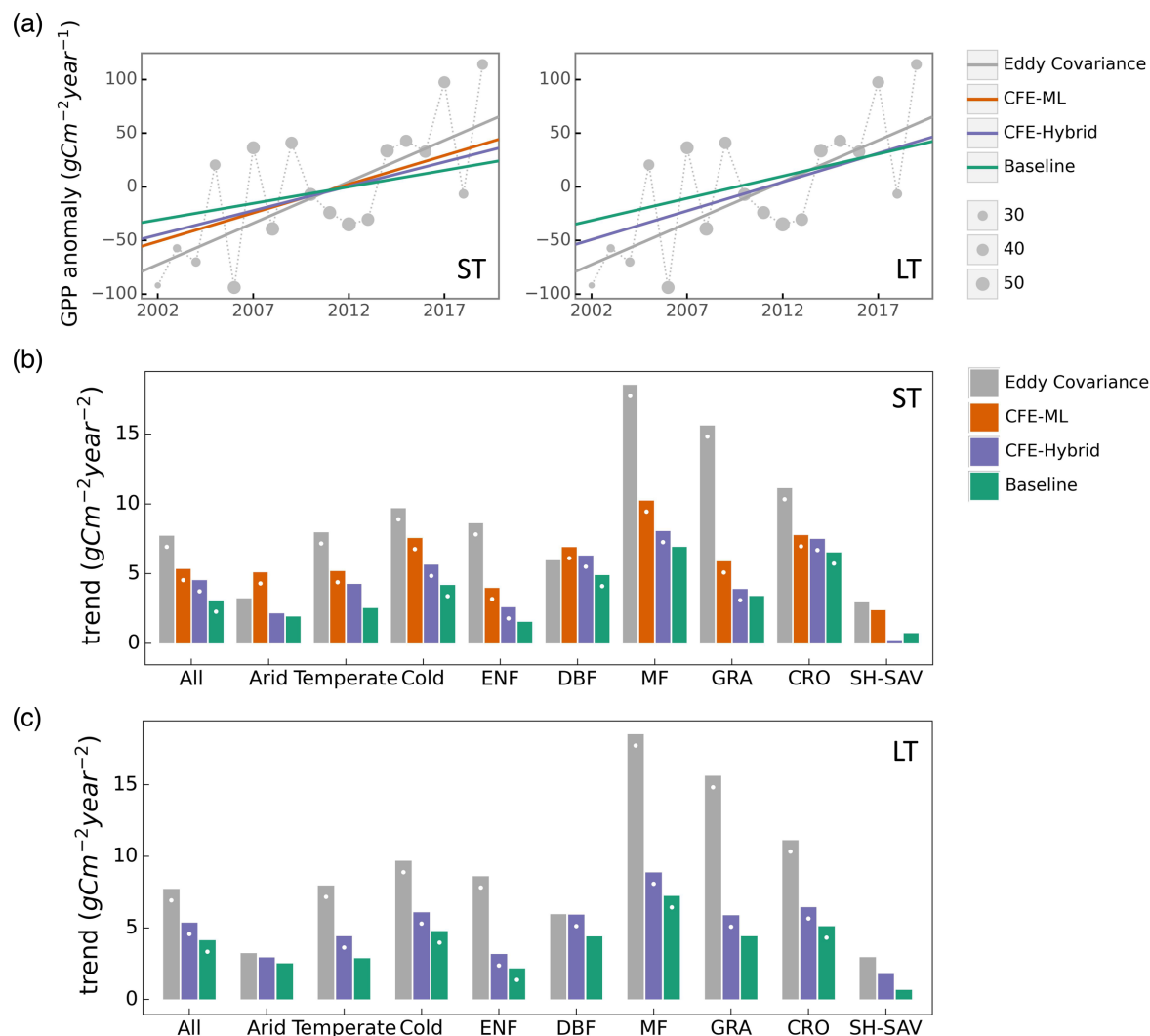
Figure 5. Comparison of observed and predicted GPP (from NT models only) trends across eddy covariance flux towers. (a) Aggregated annual GPP anomaly from 2002 to 2019 and trend lines from eddy covariance (EC) data, and three CFE model setups (short-term, night-time partitioning) for ST (left) and LT (right) models. The size of grey circle markers is proportional to the number of sites. (b) Comparison of annual GPP trends from eddy covariance measurements and the short-term (ST) CEDAR-GPP model setups by plant functional types and climate zones. (c) Comparison of annual GPP trends from eddy covariance measurements and the long-term (LT) CEDAR-GPP model setups by plant functional types and climate zones. In (b) and (c), Categories with less than 6 sites, including Tropics and EBF, were not shown. While dots on the bars indicate statistically significant trends with p-value < 0.1. Results for the DT models are shown in Supplementary Figure S3.

The differences in estimated GPP trends between the Baseline and CFE models underscore the significant long-term GPP changes driven by the direct CO_2 effect. Using explainable machine learning

510 approaches – ALE and SHAP, we further assessed the CFE-ML models for quantifying the direct
511 CO_2 effect. Both approaches revealed a consistently positive influence of CO_2 on GPP, aligning with
512 biophysical theories (Figure S8). Compared to the effects from light (PAR) and vegetation structures
513 (e.g. NIRv), the impacts of CO_2 are considerably smaller, which explains the minimal differences in
514 overall model accuracy between the Baseline and CFE models.

515 Finally, we evaluated CEDAR-GPP using independent eddy covariance data (11 sites, Table S3)
516 that was not involved in model training and obtained from the OzFlux FluxNet dataset (Ozflux, 2024).
517 Among these sites, only two - AU-Cpr (Tropical) and AU-Stp (Aird) - with more than five years of
518 records exhibit a GPP trend with p-value less than 0.3. CEDAR-GPP shows strong consistency with
519 the observed trend (Figure S9). Additionally, CEDAR-GPP achieves reasonable accuracy in predicting
520 monthly GPP ($R^2 \sim 0.73 – 0.75$), mean seasonal cycle ($R^2 \sim 0.74 – 0.78$), and monthly anomalies (R^2
521 $\sim 0.26 – 0.50$) (Table S4, Figure S10), closely aligning with the cross-validation results.

3.2 Evaluation of GPP spatial and temporal dynamics

523 We compared CEDAR-GPP estimates with other upscaled or LUE-based datasets regarding
524 the mean annual GPP (Sect. 3.2.1), GPP seasonality (Sect. 3.2.2), interannual variability (Sect. 3.2.3),
525 and annual trends (Sect. 3.2.4). CEDAR-GPP model setups generally show similar patterns in mean
526 annual GPP, seasonality, and interannual variability, therefore, in corresponding sections, we present
527 the CFE-Hybrid model setups as representative examples for comparisons with other datasets, unless
528 otherwise stated. Supplementary figures include comparisons involving CEDAR-GPP estimates from
529 all model setups.

3.2.1 Mean annual GPP

531 Global patterns of mean annual GPP are generally consistent among CEDAR-GPP model
532 setups, FLUXCOM, FLUXSAT, MODIS, and rEC-LUE, with few noticeable regional differences
533 (Figure 6, Figure S11). Differences among CEDAR-GPP model setups are minimal and only evident
534 between the NT and DT setups in the tropics (Figure 6b-c, Figure S11). CEDAR-GPP short-term
535 datasets show highest consistency with FLUXSAT in terms of mean annual GPP magnitudes (2001 –
536 2018) and latitudinal variations, although FLUXSAT presents slightly higher GPP values in the tropics
537 compared to CEDAR-GPP (Figure 6b). Mean annual GPP magnitudes for FLUXCOM-RS006 and
538 MODIS are lower globally than CEDAR-GPP and FLUXSAT, with the most pronounced differences
539 observed in the tropical areas. Among the long-term datasets (CEDAR-GPP LT, FLUXCOM-ERA5,

and rEC-LUE), mean annual GPP (1982 – 2018) exhibits greater disparities in the northern mid-latitudes than in the tropics and southern hemisphere (Figure 6c). CEDAR-GPP aligns more closely with FLUXCOM-ERA5 than with rEC-LUE, with the latter showing lower annual mean GPP globally, particularly between 20ºN to 50º N.
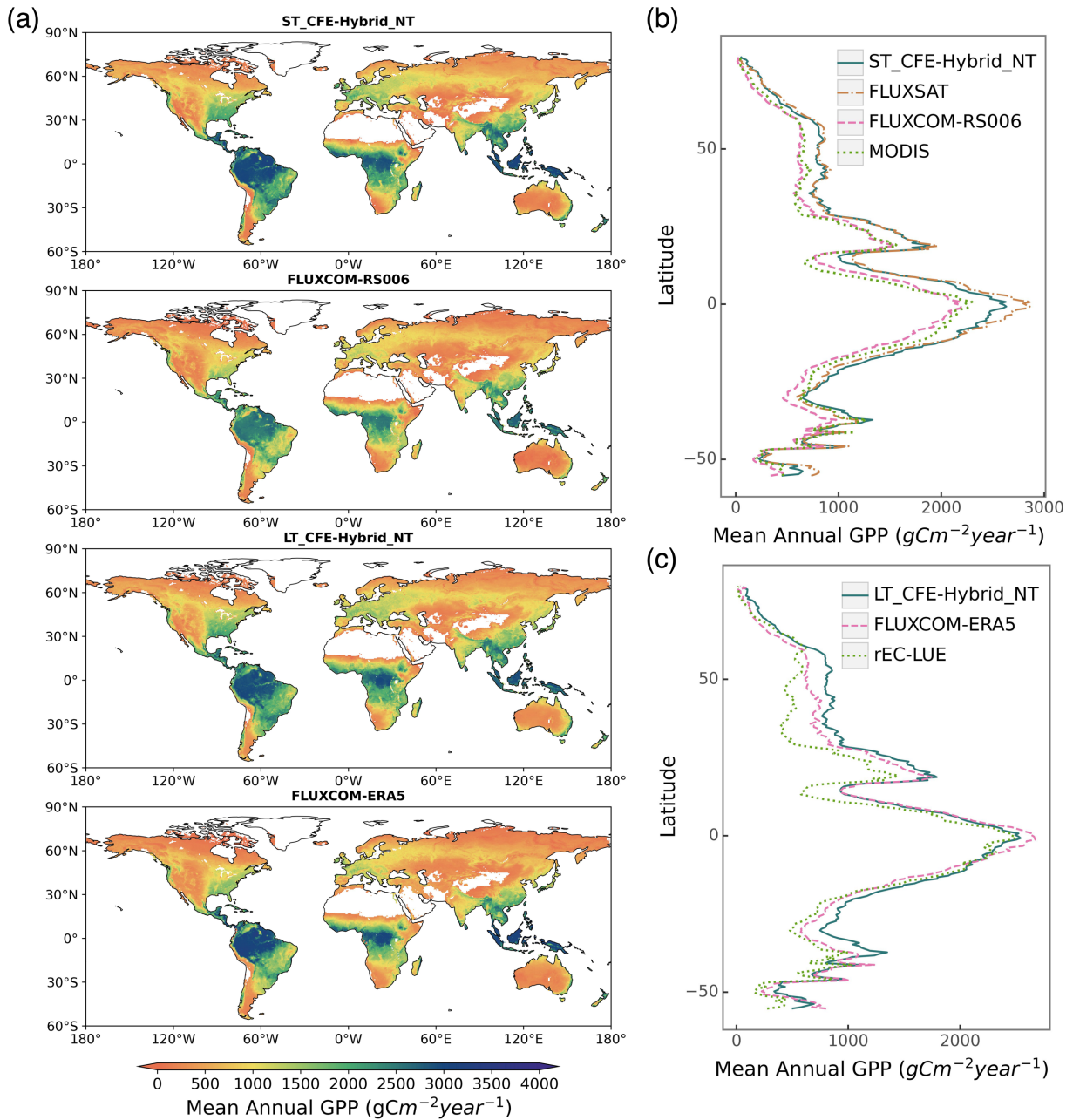
Figure 6. Global distributions of mean annual GPP from CEDAR-GPP and other machine learning upscaled and LUE-based reference datasets. (a) Global patterns of mean annual GPP from two short-term datasets including ST_CFE-Hybrid_NT, and FLUXCOM-RS006, and two long-term datasets including LT_CFE-Hybrid_NT, and FLUXCOM-ERA5. (b) Latitudinal distributions of mean annual GPP from short-term

550   datasets (ST_CFE-Hybrid_NT, FLUXSAT, FLUXCOM-RS006, and MODIS). (c)
551   Latitudinal distributions of mean annual GPP from long-term datasets (LT_CFE-
552   Hybrid_NT, FLUXCOM-ERA5, and rEC-LUE). Mean annual GPP was computed
553   between 2001 and 2018 for short-term datasets and between 1982 and 2018 for long-
554   term datasets.

555 3.2.2   Seasonal variability

556   CEDAR-GPP agrees with other GPP datasets on seasonal variabilities (average between 2001

557 and 2018) at the global scale, characterized by a peak in GPP in July and a nadir between December

558 and January (Figure 7, Figure S12). At the global scale, CEDAR-GPP is most closely aligned with

559 FLUXSAT in GPP seasonal magnitude and amplitude, while both FLUXCOM and MODIS display

560 a relatively less pronounced magnitude.

561   In boreal and temperate regions of the Northern Hemisphere, all datasets agree on seasonal

562 GPP variation, with only minor variances in the magnitude of peak GPP. In Southern Hemisphere

563 temperate regions, datasets demonstrate similar seasonality, though with greater variability in peak

564 amplitudes compared to the Northern Hemisphere. The largest disparities are found in the South

565 American tropical areas, where seasonal variation is less prominent. Here, FLUXSAT shows a distinct

566 bi-modal pattern with peaks in March-April and September-October. CEDAR-GPP and FLUXCOM-

567 ERA5 aligns with the second peak, but exhibit a less pronounced first peak. Interestingly, the DT

568 setups of CEDAR-GPP show slightly higher peaks in March-April in this region (Figure S13). MODIS,

569 in contrast, indicates an inverse seasonal pattern with a small peak from June to August. Across all

570 regions, CEDAR-GPP's seasonality aligns more closely with FLUXSAT and FLUXCOM-ERA5 than

571 with other datasets. Differences among the ten CEDAR-GPP model setups are minimal, except for

572 small variations in GPP magnitude in some tropical areas between NT and DT setups (Figure S13).
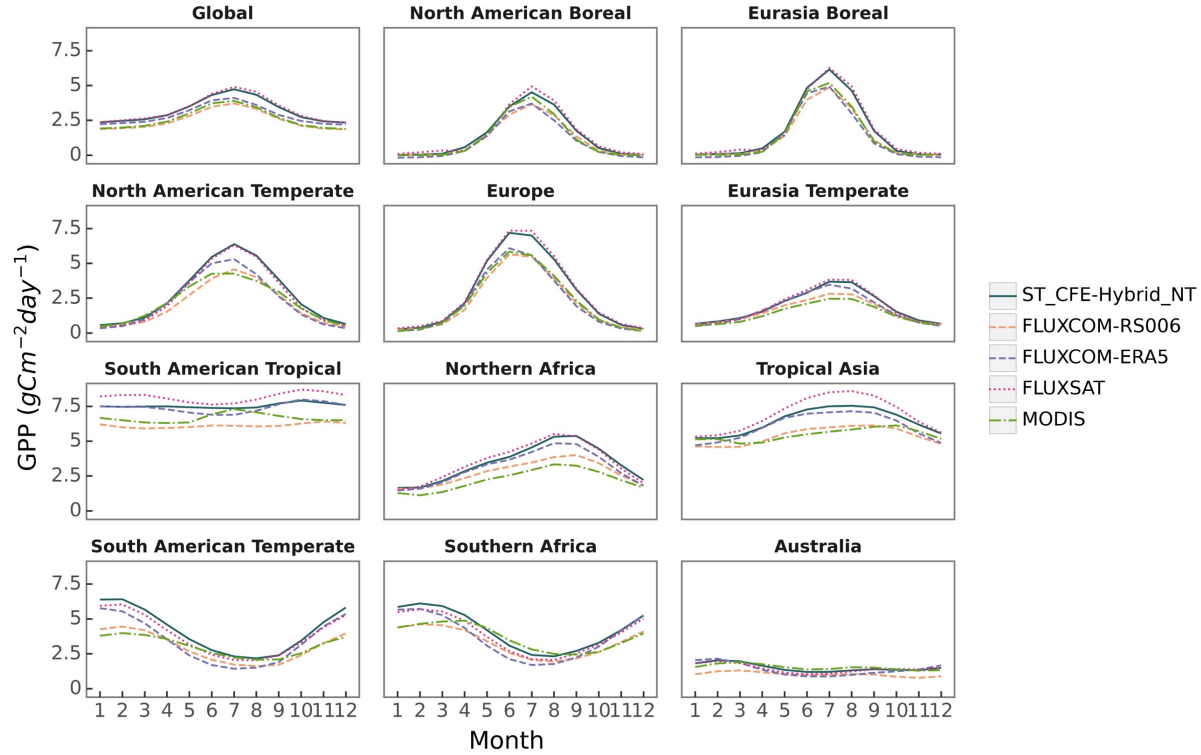
Figure 7. Comparison of global and regional GPP mean seasonal cycle between different datasets on a global scale. Monthly means were averaged from 2001 to 2018 for all datasets. Geographic boundaries of the 11 TransCom land regions were obtained from the CarbonTracker (CT2022) dataset and shown in Figure S19.

3.2.3 Interannual variability

We found distinct spatial patterns in GPP interannual variability between upscaled and LUE-based datasets and a high level of agreement within each category, with the exception of FLUXCOM-ERA5, which show minimal interannual variability globally (Figure 8, Figure S14). All datasets agree on the presence of GPP interannual variability hotspots in eastern and southern South America, central North America, southern Africa, and western Australia. These hotspots primarily correspond to arid and semi-arid areas characterized by grasslands, shrubs, and croplands (Figure 9). CEDAR-GPP is highly consistent with FLUXSAT, and both datasets also display relatively high interannual variability in the dry subhumid areas of Europe, predominantly covered by croplands. FLUXCOM-RS006 mirrors the relative spatial patterns of CEDAR-GPP and FLUXSAT, albeit at lower magnitudes. The LUE-based datasets (MODIS and rEC-LUE) predict a much higher interannual variability than the upscaled datasets in the tropical areas, particularly in evergreen broadleaf forests and woody savannas (Figure 8, Figure 9). These datasets also depict slightly higher interannual variability for other types of forests, including evergreen needleleaf forests and deciduous broadleaf

592 forests, compared to the upscaled datasets. The lack of interannual variability in FLUXCOM-ERA5

593 is attributable to the use of mean seasonal cycles of remotely sensed vegetation greenness indicators

594 rather than their dynamic time series. Ten CEDAR-GPP model setups present consistent patterns in

595 interannual variability, and differences were minimal (Figure S14).

596
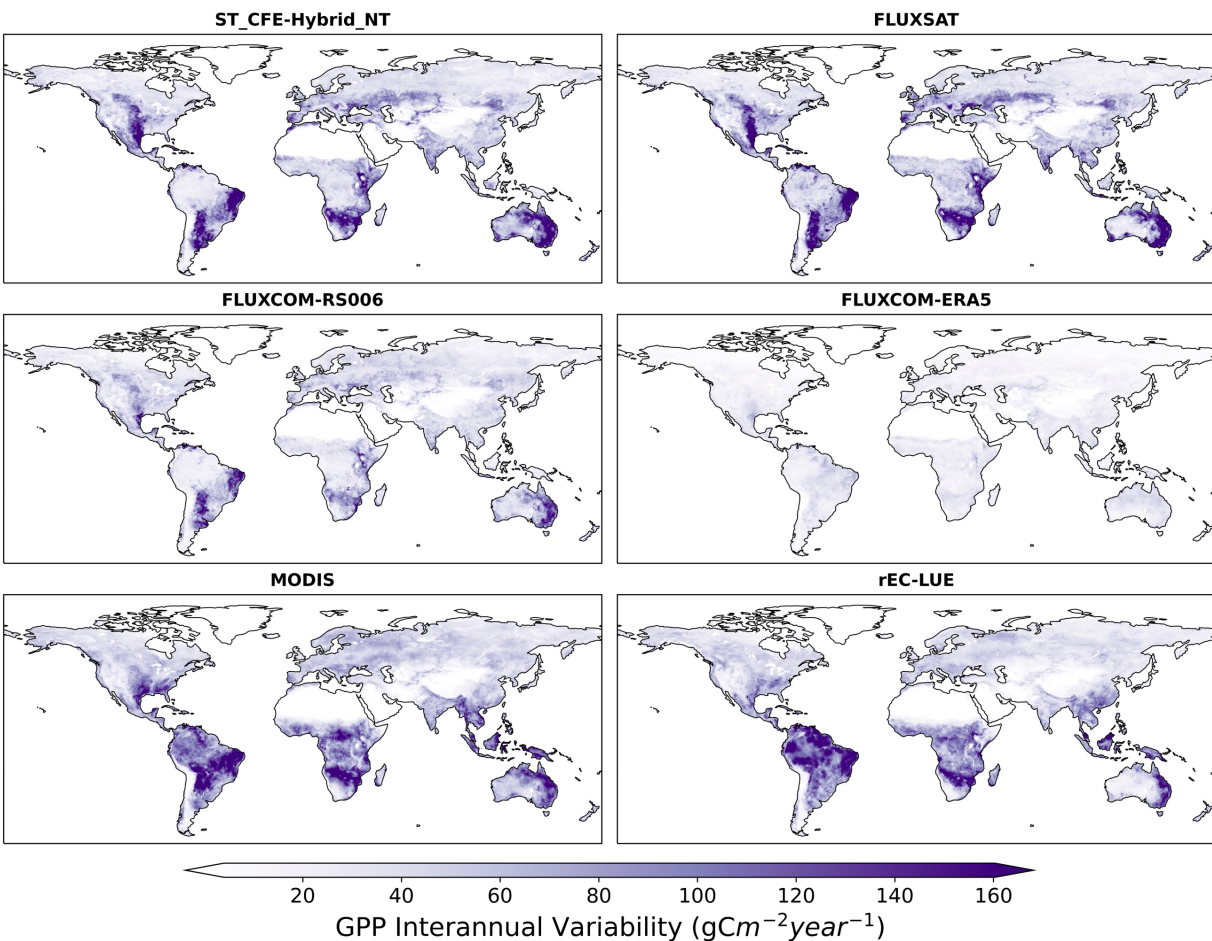
597 Figure 8. Spatial patterns of GPP interannual variability extracted over 2001 to 2018
598 for CEDAR-GPP (ST_CFE-Hybrid_NT), FLUXSAT, FLUXCOM-RS006, MODIS,
599 FLUXCOM-ERA5, and rEC-LUE.
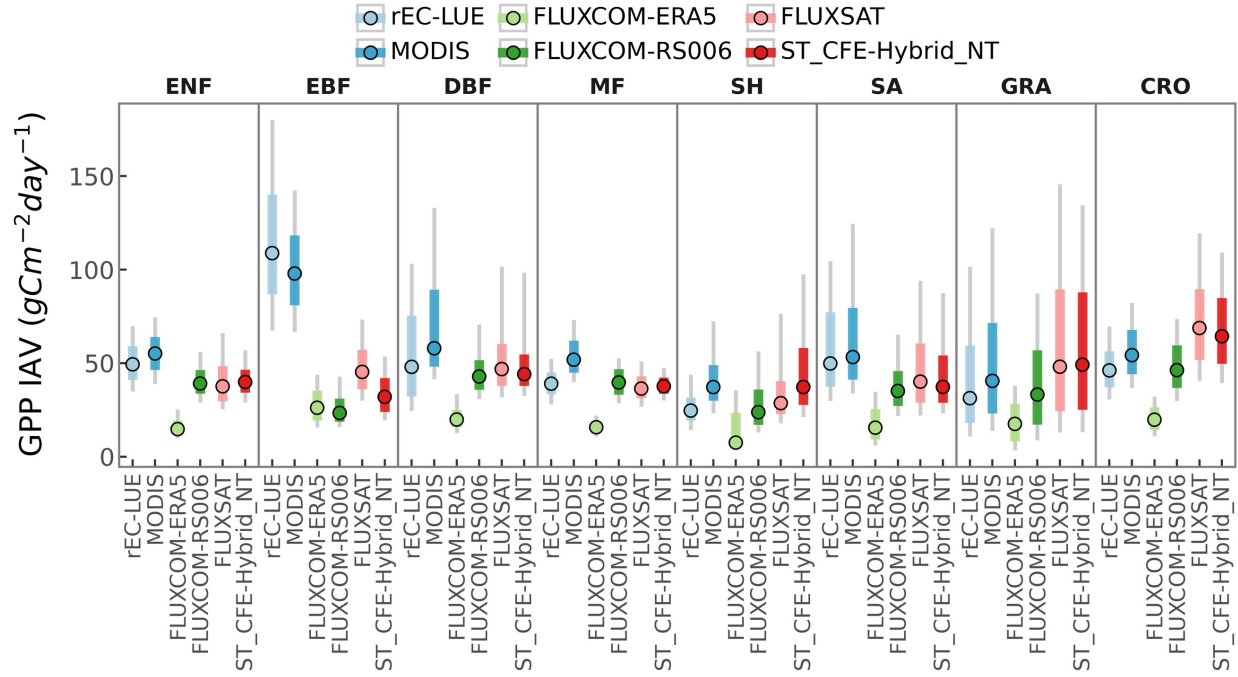
Figure 9. Comparison of GPP interannual variability (IAV) across global datasets by PFT. Colored dots represent the median IAV, thicker gray bars indicate the 25% to 75% percentiles of IAV distributions, and thinner grey bards show the 10% to 90% percentiles.

3.2.4 Trends

Differences in annual GPP trends among CEDAR-GPP model setups and other upscaled and LUE-based datasets mainly reflect the variability in the representation of CO_2 fertilization effects (Figure 10, Figure S15). From 2001 to 2018, the CEDAR-GPP Baseline model setups show spatial variations in GPP trends consistent with the other upscaled datasets without direct CO_2 fertilization effects, including FLUXSAT and FLUXCOM-RSv006. In these datasets, substantial increases are seen in southeastern China and India, western Europe, and part of North and South America. These increases are largely associated with rising LAI due to land use changes and indirect CO_2 fertilization effects, as identified by previous studies (Chen et al., 2019; Zhu et al., 2016). Although MODIS, which also does not include a direct CO_2 fertilization effect, generally agrees with these increasing trends, it also shows a declining GPP in the tropical Amazon and a stronger positive trend in central South America. After incorporating the direct CO_2 fertilization effects, both the CFE-Hybrid and CFE-ML setups predict positive trends in tropical forests, an observation absent in all other datasets. Furthermore, the CFE-Hybrid and CFE-ML models also reveal increasing GPP in temperate and

boreal forests of North America and Eurasia. Notably, all datasets agree on a pronounced GPP decrease in eastern Brazil.

From 2001 to 2018, a positive trend in global annual GPP is uniformly detected by all datasets, albeit with varying magnitudes (Figure 11a-b). The ST_Baseline_NT model predicts a GPP growth rate of 0.35 (±0.02) Pg C per year, aligning with FLUXCOM-RS, but lower than FLUXSAT (0.51 Pg C yr^{-2}) and MODIS (0.39 Pg C yr^{-2}) (Figure 11b). The CFE-hybrid models estimate a notably faster GPP growth at 0.58 (±0.03) Pg C yr^{-2}. The CFE-ML models predict the highest trends, up to 0.76 (±0.15) Pg C yr^{-2} from the ST_CFE-ML_NT model and 0.59 (±0.13) Pg C yr^{-2} from the ST_CFE-ML_DT model. Also, a higher variance is observed among ensemble members in the ST_CFE-ML setups compared to the ST_Baseline and ST_CFE-Hybrid models.

The LT_Baseline_NT model identifies increasing GPP trends in large areas of Europe, East and South Asia, as well as the Northern Amazon from 1982 to 2020 (Figure 10b). The pattern from the LT_CFE-Hybrid_NT model aligns closely with the LT_Baseline_NT model but exhibit a stronger positive trend in global tropical areas as well as Eurasian boreal forests. In contrast, FLUXCOM-ERA5 shows overall negative trends in the tropics, with a small magnitude. Lastly, rEC-LUE agrees with positive GPP trends identified in CEDAR-GPP in the extratropical areas, but predictes a pronounced negative trend in the tropics. At the global scale, all the CEDAR-GPP long-term models predict a positive global GPP trend (Figure 11d). The LT_Baseline_NT and LT_Baseline_DT models show a trend of 0.13 (±0.02) and 0.15 (±0.02) Pg C yr^{-2} respectively, while the LT_CFE-Hybrid_NT and LT_CFE-Hybrid_DT models double these rates with 0.33 (±0.02) and 0.31 (±0.03) Pg C yr^{-2} respectively. rEC-LUE shows a two-phased pattern with a strong increase in GPP from 1982 to 2000 (0.54 Pg C yr^{-2}), followed by a decreasing trend after 2001 (-0.20 Pg C yr^{-2}) (Figure S16). This results in an overall positive change at a rate comparable to that of the Baseline model. FLUXCOM-ERA5 exhibited a small negative trend.
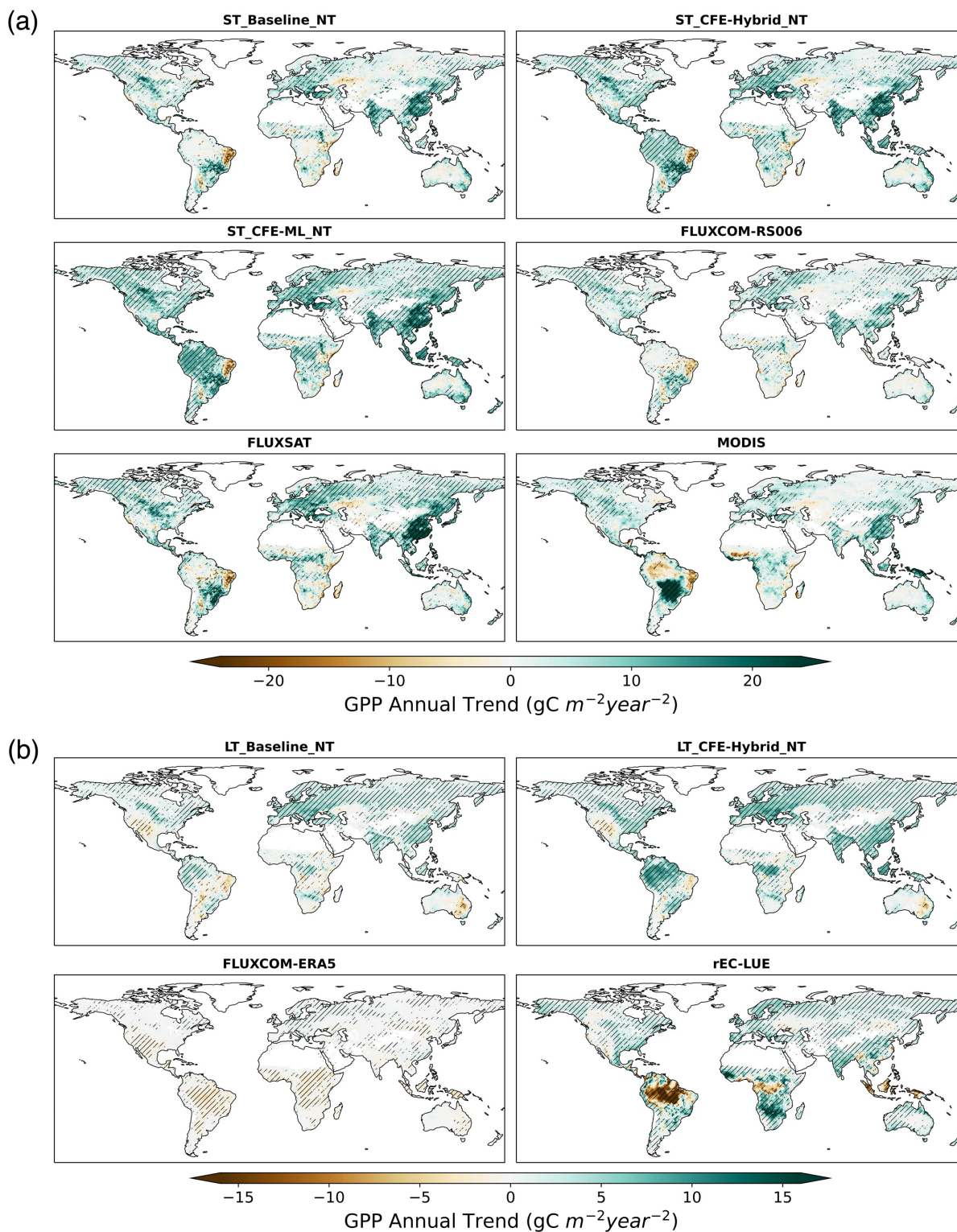
Figure 10. Annual GPP trend over 2001 – 2018 for short-term CEDAR-GPP, FLUXCOM-RS006, FLUXSAT, and MODIS datasets (a) and over 1982 – 2018 for long-term CEDAR-GPP, FLUXCOM-ERA5 and rEC-LUE datasets (b). Hatched

647 areas indicate the GPP trend that is statistically significant at p < 0.05 level under the
648 Mann-Kendall test.

649
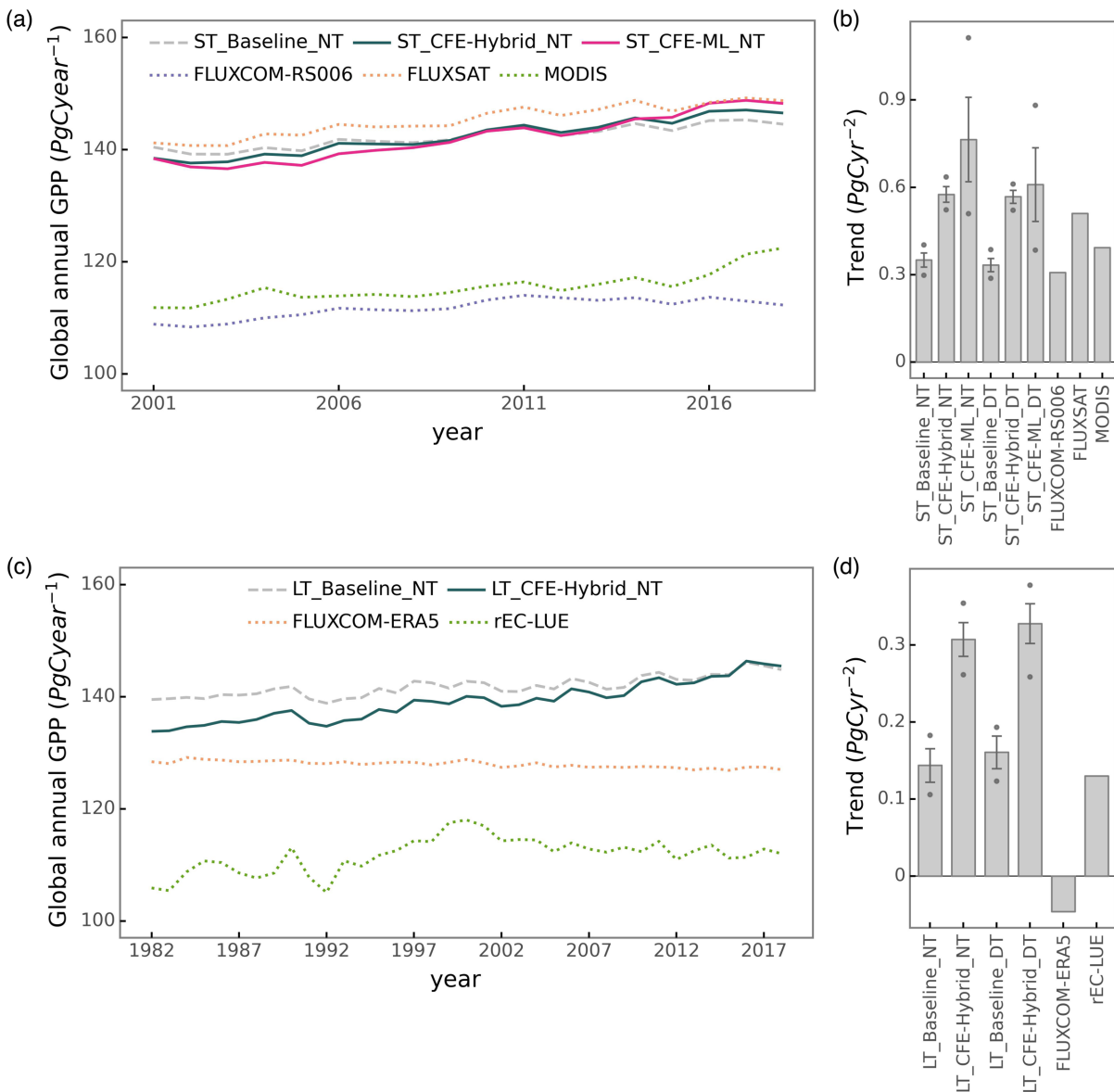
650 Figure 11. Global annual GPP variations (a) and trends (b) from 2001 to 2018 for
651 short-term CEDAR-GPP, FLUXCOM-RS006, FLUXSAT, and MODIS datasets.
652 Global annual GPP variations (c) and trends (d) over 1982 to 2018 for long-term for
653 long-term CEDAR-GPP, FLUXCOM-ERA5, and rEC-LUE datasets. Error bars in
654 (b) and (d) represent the 25% to 75% percentile from the model ensembles of
655 CEDAR-GPP. Dots in (b) and (d) indicate the minimum and maximum from the
656 model ensembles of CEDAR-GPP.

657 Among the process-based models forced by remote sensing data, CEDAR-GPP aligns closely
658 with BESS v2 and BEPS, showing widespread positive GPP trends in the boreal and temperate regions

659   of the Northern Hemisphere, as well as across tropical areas (Figure S17, S18). In contrast, PML V2

660   presents minimal GPP changes in tropics and substantial reduction in Africa. The CEDAR-GPP CFE-

661   ML model exhibits higher trends in tropical and northern hemisphere temperate regions, while BEPS

662   shows more pronounced trends in boreal regions. None of the products indicates significant GPP

663   trends in Australia. Globally, trends from BEPS and BESS V2 are around 0.55 PgC year^{-1}, consistent

664   with CEDAR's ST_CFE-Hybrid_NT model at 0.58 PgC year^{-1}, while PML V2 displays a neutral trend

665   of 0.08 PgC year^{-1}.

666   ## 3.3 GPP estimation uncertainties

667   We analyzed the spread between the 30 model ensemble members in CEDAR-GPP as an

668   indicator of uncertainties in GPP estimations. The spatial pattern of uncertainty in estimating annual

669   mean GPP largely resembles that of the mean map (Figure 12, Figure 6a). The largest model spread is

670   found in highly productive tropical forests, and this uncertainty decrease in temperate and cold areas

671   (Figure 12a). Tropical ecosystems, with a mean annual GPP between 1000 to 3500 PgC year^{-1}, only

672   exhibit a 2% and 6% variation within the model ensemble (Figure 12b). Ecosystems in the temperate

673   and cold climates have a smaller annual GPP and proportionally small uncertainties of up to 6%.

674   However, ecosystems in Arid and Polar climates, despite their similarly low GPP, show higher model

675   uncertainty, reaching 10% to 40% of the ensemble mean.

676   The estimation uncertainty of GPP trends is generally below 15% to 20% in the CEDAR-GPP

677   datasets under the ST_Baseline and ST_CFE-Hybrid setups (Figure 12c). However, in the ST_CFE-

678   ML setup, the estimation increases substantially, with model spread reaching up to 40% in tropical

679   areas. Figure S20 further illustrates the trend uncertainties with the ensemble mean error range based

680   on one standard deviation. Both the CFE-ML models show large discrepancies between the upper

681   and lower uncertainty ranges particularly within the tropics. Additionally, the long-term models also

682   show a higher uncertainty compared to the short-term models.

683
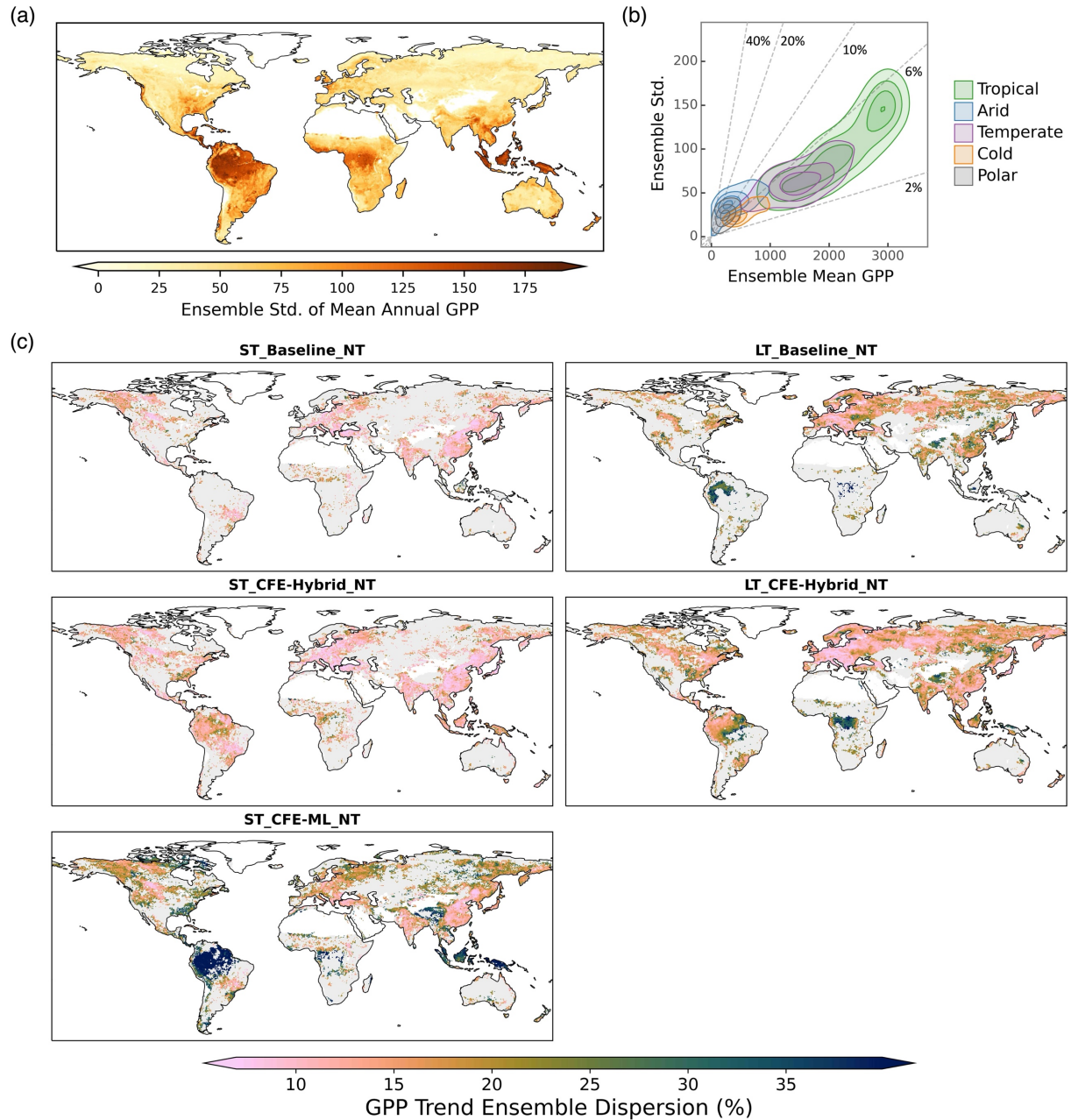
Figure 12. CEDAR-GPP estimation uncertainty derived from ensemble spread (standard deviation of 30 model predictions). (a) Spatial patterns of the absolute standard deviation from ensemble members in estimating the mean annual GPP from 2001 to 2018, using data from the ST_CFE-Hybrid_NT setup. (b) Relationships between ensemble standard deviation and ensemble mean in mean annual GPP. Colored contours denote clusters of Koppen climate zones. Dashed lines indicate the ratio between the ensemble standard deviation and the ensemble mean with values shown in percentage. (c) Spatial patterns of model uncertainty in GPP long-term trend estimation. Only areas where 90% of the ensemble members showed a statistically significant trend (p<0.05) are shown in the maps. The trend for the short-term datasets

694 (left column) was computed between 2001 to 2018. The trend for the long-term
695 datasets (right column) was computed between 1982 to 2018.

4. Discussion

4.1 Reducing uncertainties in GPP upscaling

Here we examine the three predominant sources of uncertainties in machine learning upscaling of GPP: eddy covariance measurements, input datasets, and the machine learning model. We discuss strategies used in CEDAR-GPP to reduce the impacts of these uncertainties and highlight potential future research directions.

4.1.1 Eddy covariance data

Uncertainties associated with eddy covariance measurement and data processing can propagate through the upscaling process. CEDAR-GPP was produced using monthly aggregated eddy covariance data, where the impact of random errors in half-hourly measurements was minimized due to the temporal aggregation (Jung et al., 2020). Our stringent quality screening further reduced data processing uncertainties such as those associated with gap-filling. Yet, the discrepancy in GPP patterns between the CEDAR-GPP NT and DT setups is indicative of systematic biases linked to the partitioning approaches used to derive GPP from the NEE measurements (Keenan et al., 2019; Pastorello et al., 2020). Interestingly, the mean annual GPP from the DT setup is slightly higher than that from the NT setup (Figure 6), and the DT setup also predicts a higher GPP trend in the long-term dataset (Figure 11). While these discrepancies are relatively small compared to the predominant spatiotemporal patterns, the separate DT and NT setups in CEDAR-GPP offer an interesting quantification of the GPP partitioning uncertainties over space and time, providing insights for future methodology improvements.

The unbalanced spatial representativeness of the eddy covariance data constitutes a more significant source of uncertainty, as highlighted by previous studies (Jung et al., 2020; Tramontana et al., 2015). Effective generalization of machine learning models requires a substantial volume of training data that adequately represents and balances varied conditions. In CEDAR-GPP, this issue was mitigated with a large set of eddy covariance data (~18000 site-months) integrating FLUXNET2015 and two regional networks. However, data availability remains limited in critical carbon exchange hotspots such as tropics, subtropics, drylands, and boreal regions, as well as in

723 mountainous areas (Figure 1). Contrary to widespread perception that sparse training data leads to
724 high upscaling uncertainties, our findings from the bootstrapped model spread indicates modest
725 uncertainties in tropical areas relative to their high GPP magnitude (Figure 12). This observation aligns
726 with findings from the FLUXCOM product, revealing low extrapolation uncertainty in humid tropical
727 regions (Jung et al., 2020). Nevertheless, to fully understand the upscaling uncertainty, it is essential to
728 evaluate the generalization or extrapolation errors within the predictor space and consider the
729 potential limitations of model structures (van der Horst et al., 2019; Villarreal and Vargas, 2021).
730 Additionally, data limitations in mountainous areas and the absence of topology information in the
731 predictor space in our models suggest potential uncertainties related to topographical effects on GPP
732 (Hao et al., 2022; Xie et al., 2023).

733   Furthermore, our analysis suggests that the estimated global GPP magnitudes were related to
734 the specific eddy covariance GPP data used in upscaling. Notably, global GPP magnitudes derived
735 from CEDAR-GPP closely align with those from FLUXSAT, while the estimates from FLUXCOM
736 were considerably lower (Figure 6, Figure 11). FLUXSAT used eddy covariance data from
737 FLUXNET2015, which largely overlapped with that included in CEDAR-GPP (Joiner and Yoshida,
738 2020). FLUXCOM utilized data from FLUXNET La Thuile set and CarboAfrica network, which
739 consists of a distinct set of sites (Tramontana et al., 2016). The influence from the predictor datasets
740 is minimal since all three datasets relied on MODIS-derived products. For a more in-depth evaluation
741 of the impacts of flux site representativeness on upscaling, future research directions could include
742 conducting synthetic experiments with simulations of ensembles of terrestrial biosphere models.

743 4.1.2   Input predictors and controlling factors

744   Upscaled GPP inherent uncertainties from the input predictors, including satellite and climate
745 datasets. First, satellite remote sensing data contains noises resulting from sun-earth geometry,
746 atmospheric conditions, soil background, and geolocation inaccuracies. The models or algorithms
747 used for retrieving LAI, fAPAR, LST, and soil moisture, also contain random errors and systematic
748 biases specific to certain regions, biome types, or climatic conditions (Fang et al., 2019; Ma et al., 2019;
749 Yan et al., 2016b). Moreover, satellite observations frequently contain missing values due to clouds,
750 aerosols, snow, and algorithm failure, leading to both systematic and random uncertainties. In
751 producing CEDAR-GPP, we mitigated these uncertainties through comprehensive preprocessing
752 procedures. Our temporal gap-filling strategy exploits both the temporal dependency of vegetation
753 status and long-term climatology, to reduce biases from missing values. Temporal and spatial

754   aggregation further reduced the remaining data gaps and random noises. Nevertheless, considerable
755   uncertainties likely remain in satellite datasets impacting the upscaled estimations.

756   A potentially more impactful source of uncertainty is the mismatch between the footprint of
757   the eddy covariance measurements and the coarse resolution of satellite observations. While flux
758   towers typically have a footprint of around ~1 km^2 (Chu et al., 2021), satellite observations employed
759   in CEDAR-GPP and most other upscaled datasets are at 5 km or lower resolution. Systematic and
760   random errors could be introduced due to this mismatch, particularly in heterogenous biomes and
761   areas with a mixture of vegetation and non-vegetated land covers. One mitigation strategy is to
762   generate upscaled datasets at a higher spatial resolution (e.g. 500m). Alternatively, models could be
763   trained at a high resolution and applied to the coarse resolution to reduce computation and storage
764   requirements (Dannenberg et al., 2023; Gaber et al., 2024). However, this approach does not address
765   inherent scaling errors in coarse-resolution satellite images (Dong et al., 2023; Yan et al., 2016a).

766   Besides the quality of predictors, successful machine learning upscaling also requires a
767   comprehensive set of features representing all controlling factors. For example, the lack of GPP
768   interannual variabilities in FLUXCOM-ERA5 manifests the importance of incorporating dynamic
769   vegetation signals from remote sensing in the upscaling framework. CEDAR-GPP used satellite
770   observations from optical, thermal, and microwave systems as well as climate variables thoroughly
771   representing GPP dynamics. Particularly, the inclusion of LST and soil moisture data provides
772   important information about resource limitations and stress factors, which are crucial for certain
773   biomes and/or under specific conditions (Green et al., 2022; Stocker et al., 2018, 2019). Dannenberg
774   et al. (2023) showed that incorporating LST from MODIS and soil moisture from the SMAP satellite
775   datasets substantially improved the machine learning estimation accuracy of GPP in North American
776   drylands. Nevertheless, accurately capturing interannual anomalies remains challenging for certain
777   biomes, such as evergreen needleleaf forest, cropland, and wetland (Figure 4), as acknowledged by
778   previous studies (Tramontana et al., 2016; Jung et al., 2020). High prediction uncertainties (Figure 12)
779   in drylands also suggest the machine learning models did not sufficiently represent the mechanisms of
780   water stress and drought responses. Potential improvement may be achieved by incorporating datasets
781   related to agricultural management practices (crop type, cultivar, irrigation, fertilization) (Xie et al.,
782   2021), plant hydraulic and physiological properties (Liu et al., 2021), dynamic C4 plant distributions
783   (Luo et al., 2024), root and soil characteristics (Stocker et al., 2023), as well as topography (Xie et al.,
784   2023).

4.1.3 Machine learning models and uncertainty quantification

The choice of machine learning models and their parameterization has been found to have a relatively minor impact on GPP upscaling uncertainties (Tramontana et al., 2015). CEDAR used the state-of-the-art boosting algorithm, XGBoost, which provided high performance given the current data availability. Further reduction of model uncertainty will likely rely on additional information, such as increasing the number of eddy covariance sites or incorporating more high-quality predictors. Additionally, temporal dependency of carbon fluxes responses to atmospheric controls may also be exploited with specialized deep neural networks such as recurrent neural networks or transformers (Besnard et al., 2019; Ma and Liang, 2022).

A key challenge, however, is the quantification of uncertainties in machine learning upscaling (Reichstein et al., 2019). The limited availability of eddy covariance data hinders a comprehensive assessment of the extrapolation errors; consequently, metrics of predictive performance from cross-validation are inherently biased. CEDAR derived estimation uncertainty for each GPP prediction using bootstrapping model ensemble, which naturally mimics the sampling bias associated with flux tower locations. Notably, the choice of input climate reanalysis datasets could also induce systematic differences in GPP spatial and temporal patterns (Tramontana et al., 2015). As a result, the FLUXCOM product generates model ensembles based on different reanalysis datasets to capture these uncertainties. Additionally, different satellite datasets of vegetation structural proxies, such as LAI, also exhibited significant discrepancies (Jiang et al., 2017). Thus, an ensemble approach combining site-level bootstrapping with multiple sources of input predictors could potentially provide a more comprehensive quantification of uncertainties. Furthermore, tree-based models do not generalize well to unseen conditions, and the uncertainty estimates derived from bootstrapping of XGBoost models may underrepresent actual biases stemming from limitations in training data representation. Future work may explore Bayesian neural networks, which provide uncertainty along with predictions and, at the same time, present high predictive power comparable to ensemble tree-based algorithms (Ma et al., 2021).

4.2 Long-term GPP changes and CO_2 fertilization effect

CEDAR-GPP was constructed using a comprehensive set of climate variables and multi-source satellite observations, thus encapsulating long-term GPP dynamics from both direct and indirect effects of climate controls. Particularly, CEDAR-GPP included the direct CO_2 fertilization effect,

815   which has been shown to dominate the increasing trend of global photosynthesis (Chen et al., 2022).

816   Incorporating these effects substantially improved long-term trends of GPP from site to global scales

817   (Figure 5, 10, 11). CEDAR's CFE-Hybrid setup offers a conservative estimation of the direct CO_2

818   effects by simulating the CO_2 sensitivity of light-limited LUE for C3 plants (Walker et al., 2021).

819   However, the model does not account for the impacts of nutrient availability, which could potentially

820   constrain CO_2 fertilization (Peñuelas et al., 2017; Reich et al., 2014; Terrer et al., 2019). Robust

821   modeling of LUE responses to rising CO_2 under various environmental conditions remains

822   challenging (Wang et al., 2017). Future work is needed to better understand how these factors affect

823   the quantification of GPP and its long-term temporal variations.

824   The CFE-ML model adopted a data-driven approach to infer CO_2 effects directly from eddy

825   covariance data. This strategy allows the model to potentially capture multiple physiological pathways

826   of the CO_2 impact evidenced in the eddy covariance measurements, including the increases of the

827   biochemical rates and enhancements in the water use efficiency (Keenan et al., 2013). The model

828   detects a strong positive effect of CO_2 on eddy covariance measured GPP, consistent with previous

829   studies based on process-based and statistical models (Chen et al., 2022; Fernández-Martínez et al.,

830   2017; Ueyama et al., 2020). Moreover, spatial patterns of GPP trends derived from the CFE-ML model

831   reflected a strong temperature dependency, aligning with the anticipated temperature sensitivity of

832   photosynthetic biochemical processes (Keenan et al., 2023). Yet, the considerable ensemble spread in

833   the CO_2 trends from the CFE-ML model and discrepancies between the CFE setups (Figure 11, Figure

834   13) underscores a high level of uncertainty in the machine learning quantified CO_2 effects.

835   Several limitations should be noted regarding GPP trend estimation and validation. First, the

836   CFE-ML model may not fully capture the intricate mechanisms of plant physiological responses to

837   CO_2. For example, eddy covariance towers, especially long-term sites, are typically located in

838   homogeneous and undisturbed ecosystems, not representative of the full diversity of ecosystems

839   globally. Thus, interactions between CO_2 and natural or human-induced disturbance, as well as many

840   other stresses, are likely underrepresented in the models. Ultimately, the model's capacity to robustly

841   quantify CO_2 fertilization is constrained by the scope and diversity of the eddy covariance data.

842   Additionally, the use of spatially invariant CO_2 data may not fully represent the actual CO_2 variations

843   that plants experience across different environments.

844   Secondly, CO_2 effects inferred by the CFE-ML models may be confounded by other factors

845   that correlate with CO_2 over time. Industrialization-induced nitrogen deposition could synergistically

846   boost GPP alongside CO_2 (O'Sullivan et al., 2019). Technological and management improvements in

847 agriculture that contribute to a global enhancement of crop photosynthesis (Zeng et al., 2014), might
848 also be indirectly reflected in the model estimates. Moreover, interactions with the other input features
849 that exhibit long-term trends, such as those induced by non-biological factors (e.g. sensor orbital
850 drifts), also affect the CO_2 effects inference. Additionally, other factors that could lead to long-term
851 GPP trends (e.g. forest aging, disturbances) might also be underrepresented in our models.

852 Finally, direct validation of GPP trends is limited, particularly in tropical regions, constrained
853 by the availability of long-term records. Detecting and evaluating trends is challenging and typically
854 requires long monitoring records (e.g. over 10 to 15 years), since long-term changes, such as those
855 induced by CO_2, are very small relative to large interannual variations. Evaluating aggregated GPP
856 trends across multiple sites presents an alternative approach; however, there were still insufficient sites
857 in tropical and evergreen broadleaf forest areas to robustly validate our estimates for those ecosystems
858 (Figure 5). Partly due to data limitations, uncertainties in GPP estimated from bootstrapped samples
859 are very high in tropical areas (Figure 12). Thus, trend estimates in these areas should be interpreted
860 in the context of associated uncertainties and limitations.

861 Our results also suggested that variations in the estimated GPP long-term trends from different
862 products are largely related to the representation of CO_2 fertilization. Products that do not consider
863 the direct CO_2 effect, including our Baseline models, FLUXSAT, FLUXCOM, and MODIS, show
864 minimal long-term changes in tropical GPP, while the CEDAR CFE-ML and CFE-Hybrid models
865 demonstrate significant GPP increases aligning with predictions from the terrestrial biosphere models
866 (Anav et al., 2015). FLUXCOM-ERA5, not accounting for dynamics changes in vegetation structures
867 and CO_2, does not capture either the direct or indirect CO_2 fertilization resulting in a slight negative
868 GPP trend attributable to shifted climate patterns. Notably, rEC-LUE exhibit contrasting trends
869 before and after circa 2000, primarily attributed to changes in vapor pressure deficit, PAR, and LAI,
870 while the direct CO_2 fertilization effect remains consistent (Zheng et al., 2020). CEDAR CFE-ML and
871 CFE-Hybrid models align well with two process-based models forced with remote sensing data which
872 consider direct CO_2 effects (BESS and BEPS). Nevertheless, considerable differences between
873 CEDAR-GPP and other remote sensing products that include direct CO_2 effects (rEC-LUE and PML
874 V2) warrant more in-depth investigations into long-term GPP responses to changes in atmospheric
875 CO_2 and climate patterns.

876 Lastly, quantifications of GPP trends and their causes remain highly uncertain from site to
877 global scales. Trend detection is often complicated by data noises and interannual variabilities, thus
878 requiring long-term records which are limited in certain areas, biomes, and environmental conditions,

879 such as tropics, polar regions, wetlands, as well as ecosystems with regular or anthropogenic
880 disturbances (Baldocchi et al., 2018; Zhan et al., 2022). Moreover, isolating the effect of CO_2 is
881 challenging, as it is confounded by other factors, such as forest regrowth, land cover change, and
882 disturbances, which also significantly impacts long-term GPP variations. To this end, continued
883 efforts in expanding ecosystem flux measurements and standardizing data processing present new
884 opportunities to assess ecosystem productivity responses to changing climate conditions (Delwiche et
885 al., 2024; Pastorello et al., 2020). Future research could also leverage novel machine learning techniques,
886 such as knowledge-guided machine learning (Liu et al., 2024) and hybrid modeling that combines
887 process-based and machine learning approaches (Kraft et al., 2022; Reichstein et al., 2019).

5. Data availability and usage note

889 The CEDAR-GPP product, comprising ten GPP datasets, can be accessed at
890 https://zenodo.org/doi/10.5281/zenodo.8212706 (Kang et al., 2024). These datasets were generated
891 at a spatial resolution of 0.05º and monthly time steps. Each dataset includes an ensemble mean GPP
892 ("GPP_mean") and an ensemble standard deviation ("GPP_std"). Data is formatted in netCDF with
893 the following naming convention: "CEDAR-GPP_<version>_<model setup>_<YYYYMM>.nc".
894 The CEDAR GPP product offers GPP estimates derived from ten different models. Models
895 are characterized by 1) temporal coverage, 2) configuration of CO_2 fertilization, and 3) GPP
896 partitioning approach (Table 2). We provide a structured approach to selecting the most appropriate
897 dataset for research or applications.
898 1) Study period considerations: the Short-Term (ST) setup is ideal for studies focusing on
899 periods after 2000. These models are constructed using a broader range of explanatory predictors,
900 offering higher precision and smaller random errors. The Long-Term (LT) datasets shall be used for
901 research assessing GPP dynamics over a longer time period (before 2001). It is important to note that
902 trends from the ST and LT datasets are not directly comparable, as they were derived from different
903 satellite remote sensing data.
904 2) CO_2 Fertilization Effect (CFE) configurations: the CFE-Hybrid and CFE-ML setups are
905 preferable when assessing temporal GPP dynamics, especially long-term trends. The CFE-Hybrid
906 setup includes a hypothetical trend from the direct CO_2 effect, while CFE-ML is purely data-driven
907 and does not make any specific assumption about the sensitivity of photosynthesis to CO_2. Averaging
908 the CFE-Hybrid and CFE-ML estimates is acceptable, with the difference between them reflecting

909 the uncertainty surrounding the direct CO_2 effect. Note that the Baseline setup should not be used to
910 study long-term GPP dynamics, especially those induced by elevated CO_2. The Baseline setup may be
911 useful to compare with other remote sensing-derived GPP datasets that do not consider the direct
912 CO_2 effect. Differences between these setups regarding mean GPP spatial patterns, seasonal and
913 interannual variations are considered to be minor.

914   3) GPP partitioning methods: We recommend using the mean value derived from both the "NT"
915 (Nighttime) and "DT" (Daytime). The difference between these two provides insight into the
916 uncertainties arising from the partitioning approaches used in GPP estimation from eddy covariance
917 measurements.

918   Finally, like other upscaled or remote sensing-based GPP datasets, CEDAR-GPP should not
919 be regarded as "observations" but rather as model estimates informed by remote sensing and ground-
920 based data. The extent of assumptions or structural constraints varies across such datasets. CEDAR-
921 GPP, particularly in its CFE-Baseline and CFE-ML configurations, is entirely data-driven and
922 incorporates no explicit assumptions regarding the biological and environmental processes underlying
923 photosynthesis, apart from the generic assumptions inherent in machine learning models.
924 Consequently, the usage and interpretation of this dataset should be carefully framed within the
925 context of the input eddy covariance and environmental data as well as their limitations.

6. Code availability

927   The code for upscaling and generating global GPP datasets can be accessed at
928 https://doi.org/10.5281/zenodo.8400968.

7. Conclusions

930   We present the CEDAR-GPP product generated by upscaling global eddy covariance
931 measurements with machine learning and a broad range of satellite and climate variables. CEDAR-
932 GPP comprises four long-term datasets from 1982 to 2020 and six short-term datasets from 2001 to
933 2020. These datasets encompass three configurations regarding the incorporation of direct CO_2
934 fertilization effects and two partitioning approaches to derive GPP from eddy covariance data. The
935 machine learning models of CEDAR-GPP demonstrated high capability in predicting monthly GPP,
936 its seasonal cycles, and spatial variability within the global eddy covariance sites, with cross-validated

937 R^2 between 0.56 to 0.79. Short-term model setups consistently outperformed long-term models due
938 to considerably more and higher-quality information from multi-source satellite observations.

939 CEDAR-GPP advances satellite-based GPP estimations, as the first upscaled dataset that
940 considered the direct biochemical effects of elevated atmospheric CO_2 on photosynthesis, which is
941 responsible for an increasing land carbon sink over the past decades. We show that incorporating this
942 effect in our CFE-ML and CFE-Hybrid models substantially improved the estimation of GPP trends
943 at eddy covariance sites. Global patterns of long-term GPP trends in the CFE-ML setups show a
944 strong temperature dependency consistent with biophysical theories. However, trend estimation and
945 validation remain particularly challenging in data-scarce regions, such as the tropics, emphasizing the
946 need for enhanced data availability and methodological advancements. Beyond trends, global spatial
947 and temporal GPP patterns from CEDAR generally align with other satellite-based GPP datasets.

948 In conclusion, CEDAR-GPP, informed by global eddy covariance measurements and a broad
949 range of multi-source remote sensing observations and climatic variables, offers a comprehensive
950 representation of global GPP spatial and temporal dynamics over the past four decades. The different
951 CO_2 fertilization configurations integrated in CEDAR-GPP offer new opportunities for
952 understanding global ecosystem photosynthesis's response to increases in atmospheric CO_2 along
953 different pathways over space and time. CEDAR-GPP is expected to serve as a valuable tool for
954 benchmarking process-based modeling and constraining the global carbon cycle.

955

 Appendix A: List of eddy covariance sites

Site ID	IGBP	Data Range	Citation
AR-SLu	MF	2010 - 2011	(Garcia et al., 2016)
AR-Vir	ENF	2010 - 2012	(Posse et al., 2016)
AT-Neu	GRA	2002 - 2012	(Wohlfahrt et al., 2016)
AU-Ade	SAV	2010 - 2014	(Beringer and Hutley, 2016a)
AU-ASM	WSA	2007 - 2009	(Cleverly et al., 2016)
AU-Cpr	SAV	2010 - 2014	(Meyer et al., 2016)
AU-Cum	EBF	2012 - 2014	(Pendall et al., 2016)
AU-DaP	GRA	2007 - 2013	(Beringer and Hutley, 2016b)
AU-DaS	SAV	2008 - 2014	(Beringer and Hutley, 2016g)
AU-Dry	SAV	2008 - 2014	(Beringer and Hutley, 2016c)
AU-Emr	GRA	2011 - 2013	(Schroder et al., 2016)
AU-Fog	WET	2006 - 2008	(Beringer and Hutley, 2016d)
AU-Gin	WSA	2011 - 2014	(Macfarlane et al., 2016)
AU-How	WSA	2001 - 2014	(Beringer and Hutley, 2016e)
AU-RDF	WSA	2011 - 2013	(Beringer and Hutley, 2016f)
AU-Rig	GRA	2011 - 2014	(Beringer et al., 2016a)
AU-Tum	EBF	2001 - 2014	(Woodgate et al., 2016)
AU-Wac	EBF	2005 - 2008	(Beringer et al., 2016b)
AU-Whr	EBF	2011 - 2014	(Beringer et al., 2016c)
AU-Wom	EBF	2010 - 2014	(Arndt et al., 2016)
AU-Ync	GRA	2012 - 2014	(Beringer and Walker, 2016)
BE-Bra	MF	2001 - 2020	(Warm Winter 2020 Team, 2022)
BE-Dor	GRA	2011 - 2020	(Warm Winter 2020 Team, 2022)
BE-Lon	CRO	2004 - 2020	(Warm Winter 2020 Team, 2022)
BE-Maa	CSH	2016 - 2020	(Warm Winter 2020 Team, 2022)
BE-Vie	MF	2001 - 2020	(Warm Winter 2020 Team, 2022)
BR-Sa1	EBF	2002 - 2011	(Saleska, 2016)
BR-Sa3	EBF	2001 - 2004	(Goulden, 2016a)
CA-Ca1	ENF	2001 - 2002	(Black, 2023a)
CA-Ca2	ENF	2001 - 2010	(Black, 2023b)
CA-Ca3	ENF	2001 - 2010	(Black, 2018)
CA-Cbo	DBF	2001 - 2003	(Staebler, 2022)
CA-Gro	MF	2003 - 2014	(McCaughey, 2022)
CA-Man	ENF	2001 - 2008	(Amiro, 2016a)
CA-NS1	ENF	2002 - 2005	(Goulden, 2022a)
CA-NS2	ENF	2001 - 2005	(Goulden, 2022b)
CA-NS3	ENF	2001 - 2005	(Goulden, 2022c)
CA-NS4	ENF	2002 - 2005	(Goulden, 2016b)
CA-NS5	ENF	2001 - 2005	(Goulden, 2022d)
CA-NS6	OSH	2001 - 2005	(Goulden, 2022e)
CA-NS7	OSH	2002 - 2005	(Goulden, 2016c)
CA-Oas	DBF	2001 - 2010	(Black, 2016a)
CA-Obs	ENF	2001 - 2010	(Black, 2016b)
CA-Qc2	MF	2008 - 2010	(Margolis, 2018)
CA-Qfo	ENF	2003 - 2010	(Margolis, 2023)
CA-SF1	ENF	2003 - 2006	(Amiro, 2016b)
CA-SF2	ENF	2003 - 2005	(Amiro, 2023)
CA-SF3	OSH	2003 - 2006	(Amiro, 2016c)

CA-SJ2	ENF	2003 - 2007	(Barr and Black, 2018)
CA-TP1	ENF	2003 - 2014	(Arain, 2016b)
CA-TP2	ENF	2003 - 2007	(Arain, 2016c)
CA-TP3	ENF	2003 - 2014	(Arain, 2016d)
CA-TP4	ENF	2003 - 2017	(Arain, 2016a)
CA-TPD	DBF	2012 - 2014	(Arain, 2016e)
CA-WP1	WET	2003 - 2009	(Flanagan, 2018a)
CA-WP2	WET	2004 - 2006	(Flanagan, 2018b)
CA-WP3	WET	2004 - 2006	(Flanagan, 2018c)
CG-Tch	SAV	2006 - 2009	(Nouvellon, 2016)
CH-Aws	GRA	2006 - 2020	(Warm Winter 2020 Team, 2022)
CH-Cha	GRA	2005 - 2020	(Warm Winter 2020 Team, 2022)
CH-Dav	ENF	2001 - 2020	(Warm Winter 2020 Team, 2022)
CH-Fru	GRA	2005 - 2020	(Warm Winter 2020 Team, 2022)
CH-Lae	MF	2004 - 2020	(Warm Winter 2020 Team, 2022)
CH-Oe1	GRA	2002 - 2008	(Ammann, 2016)
CH-Oe2	CRO	2004 - 2020	(Warm Winter 2020 Team, 2022)
CN-Cha	MF	2003 - 2005	(Zhang and Han, 2016)
CN-Cng	GRA	2007 - 2010	(Dong, 2016)
CN-Din	EBF	2003 - 2005	(Zhou and Yan, 2016)
CN-Du2	GRA	2007 - 2008	(Chen, 2016c)
CN-Ha2	WET	2003 - 2005	(Li, 2016)
CN-HaM	GRA	2002 - 2004	(Tang et al., 2016)
CN-Qia	ENF	2003 - 2005	(Wang and Fu, 2016)
CN-Sw2	GRA	2011 - 2012	(Shao, 2016)
CZ-BK1	ENF	2004 - 2020	(Warm Winter 2020 Team, 2022)
CZ-BK2	GRA	2006 - 2012	(Sigut et al., 2016)
CZ-KrP	CRO	2014 - 2020	(Warm Winter 2020 Team, 2022)
CZ-Lnz	DBF	2015 - 2020	(Warm Winter 2020 Team, 2022)
CZ-RAJ	ENF	2012 - 2020	(Warm Winter 2020 Team, 2022)
CZ-Stn	DBF	2010 - 2020	(Warm Winter 2020 Team, 2022)
CZ-wet	WET	2006 - 2020	(Warm Winter 2020 Team, 2022)
DE-Akm	WET	2009 - 2020	(Warm Winter 2020 Team, 2022)
DE-Geb	CRO	2001 - 2020	(Warm Winter 2020 Team, 2022)
DE-Gri	GRA	2004 - 2020	(Warm Winter 2020 Team, 2022)
DE-Hai	DBF	2001 - 2020	(Warm Winter 2020 Team, 2022)
DE-HoH	DBF	2015 - 2020	(Warm Winter 2020 Team, 2022)
DE-Hte	WET	2009 - 2018	(Drought 2018 Team, 2020)
DE-Hzd	DBF	2010 - 2020	(Warm Winter 2020 Team, 2022)
DE-Kli	CRO	2004 - 2020	(Warm Winter 2020 Team, 2022)
DE-Lkb	ENF	2009 - 2013	(Lindauer et al., 2016)
DE-Lnf	DBF	2002 - 2012	(Knohl et al., 2016)
DE-Obe	ENF	2008 - 2020	(Warm Winter 2020 Team, 2022)
DE-RuR	GRA	2011 - 2020	(Warm Winter 2020 Team, 2022)
DE-RuS	CRO	2011 - 2020	(Warm Winter 2020 Team, 2022)
DE-RuW	ENF	2012 - 2020	(Warm Winter 2020 Team, 2022)
DE-Seh	CRO	2007 - 2010	(Schneider and Schmidt, 2016)
DE-SfN	WET	2012 - 2014	(Klatt et al., 2016)
DE-Spw	WET	2010 - 2014	(Bernhofer et al., 2016)
DE-Tha	ENF	2001 - 2020	(Warm Winter 2020 Team, 2022)
DK-Eng	GRA	2005 - 2007	(Pilegaard and Ibrom, 2016)
DK-Sor	DBF	2001 - 2020	(Warm Winter 2020 Team, 2022)

ES-Abr	WSA	2015 - 2020	(Warm Winter 2020 Team, 2022)
ES-Agu	OSH	2006 - 2019	(Warm Winter 2020 Team, 2022)
ES-Amo	OSH	2007 - 2012	(Poveda et al., 2016)
ES-LgS	OSH	2005 - 2020	(Reverter et al., 2016)
ES-LJu	WSA	2014 - 2020	(Warm Winter 2020 Team, 2022)
ES-LM1	WSA	2014 - 2020	(Warm Winter 2020 Team, 2022)
ES-LM2	OSH	2007 - 2009	(Warm Winter 2020 Team, 2022)
FI-Hyy	ENF	2001 - 2020	(Warm Winter 2020 Team, 2022)
FI-Jok	CRO	2001 - 2003	(Lohila et al., 2016)
FI-Ken	ENF	2018 - 2020	(Warm Winter 2020 Team, 2022)
FI-Let	ENF	2009 - 2020	(Warm Winter 2020 Team, 2022)
FI-Lom	WET	2007 - 2009	(Aurela et al., 2016a)
FI-Qvd	CRO	2018 - 2020	(Warm Winter 2020 Team, 2022)
FI-Sii	GRA	2016 - 2020	(Warm Winter 2020 Team, 2022)
FI-Sod	ENF	2001 - 2014	(Aurela et al., 2016b)
FI-Var	ENF	2016 - 2020	(Warm Winter 2020 Team, 2022)
FR-Aur	CRO	2005 - 2020	(Warm Winter 2020 Team, 2022)
FR-Bil	ENF	2014 - 2020	(Warm Winter 2020 Team, 2022)
FR-FBn	MF	2008 - 2020	(Warm Winter 2020 Team, 2022)
FR-Fon	DBF	2005 - 2020	(Warm Winter 2020 Team, 2022)
FR-Gri	CRO	2004 - 2020	(Warm Winter 2020 Team, 2022)
FR-Hes	DBF	2014 - 2020	(Warm Winter 2020 Team, 2022)
FR-Lam	ENF	2001 - 2008	(Warm Winter 2020 Team, 2022)
FR-LBr	WET	2017 - 2020	(Berbigier et al., 2016)
FR-LGt	CRO	2005 - 2020	(Warm Winter 2020 Team, 2022)
FR-Pue	EBF	2001 - 2014	(Ourcival et al., 2016)
FR-Tou	GRA	2018 - 2020	(Warm Winter 2020 Team, 2022)
GF-Guy	EBF	2015 - 2015	(Warm Winter 2020 Team, 2022)
GH-Ank	EBF	2011 - 2014	(Valentini et al., 2016a)
GL-NuF	WET	2008 - 2014	(Hansen, 2016)
GL-ZaF	WET	2009 - 2011	(Lund et al., 2016a)
GL-ZaH	GRA	2001 - 2014	(Lund et al., 2016b)
IL-Yat	ENF	2001 - 2020	(Warm Winter 2020 Team, 2022)
IT-CA1	DBF	2011 - 2014	(Sabbatini et al., 2016a)
IT-CA2	CRO	2011 - 2014	(Sabbatini et al., 2016b)
IT-CA3	DBF	2011 - 2014	(Sabbatini et al., 2016c)
IT-Col	DBF	2001 - 2014	(Matteucci, 2016)
IT-Cp2	EBF	2012 - 2020	(Warm Winter 2020 Team, 2022)
IT-Cpz	EBF	2001 - 2008	(Valentini et al., 2016b)
IT-La2	ENF	2001 - 2002	(Cescatti et al., 2016)
IT-Lav	ENF	2003 - 2020	(Warm Winter 2020 Team, 2022)
IT-Lsn	OSH	2016 - 2020	(Warm Winter 2020 Team, 2022)
IT-MBo	GRA	2003 - 2020	(Warm Winter 2020 Team, 2022)
IT-Noe	CSH	2004 - 2014	(Spano et al., 2016)
IT-PT1	DBF	2002 - 2004	(Manca and Goded, 2016)
IT-Ren	ENF	2001 - 2020	(Warm Winter 2020 Team, 2022)
IT-Ro1	DBF	2001 - 2008	(Valentini et al., 2016c)
IT-Ro2	DBF	2002 - 2012	(Papale et al., 2016)
IT-SR2	ENF	2013 - 2020	(Warm Winter 2020 Team, 2022)
IT-SRo	ENF	2001 - 2012	(Gruening et al., 2016)
IT-Tor	GRA	2008 - 2020	(Warm Winter 2020 Team, 2022)
JP-MBF	DBF	2004 - 2005	(Kotani, 2016a)

JP-SMF	MF	2002 - 2006	(Kotani, 2016b)
MY-PSO	EBF	2003 - 2009	(Kosugi and Takanashi, 2016)
NL-Hor	GRA	2004 - 2011	(Dolman et al., 2016a)
NL-Loo	ENF	2001 - 2018	(Drought 2018 Team, 2020)
PA-SPn	DBF	2007 - 2009	(Wolf et al., 2016)
RU-Che	WET	2002 - 2005	(Merbold et al., 2016)
RU-Cok	OSH	2003 - 2013	(Dolman et al., 2016b)
RU-Fy2	ENF	2015 - 2020	(Warm Winter 2020 Team, 2022)
RU-Fyo	ENF	2001 - 2020	(Warm Winter 2020 Team, 2022)
RU-Ha1	GRA	2002 - 2004	(Belelli et al., 2016)
SD-Dem	SAV	2007 - 2009	(Ardö et al., 2016)
SE-Deg	WET	2001 - 2020	(Warm Winter 2020 Team, 2022)
SE-Htm	ENF	2015 - 2020	(Warm Winter 2020 Team, 2022)
SE-Lnn	CRO	2014 - 2018	(Drought 2018 Team, 2020)
SE-Nor	ENF	2014 - 2020	(Warm Winter 2020 Team, 2022)
SE-Ros	ENF	2014 - 2020	(Warm Winter 2020 Team, 2022)
SE-Svb	ENF	2014 - 2020	(Warm Winter 2020 Team, 2022)
SJ-Adv	WET	2013 - 2014	(Christensen, 2016)
SN-Dhr	SAV	2010 - 2013	(Tagesson et al., 2016)
US-ARM	CRO	2004 - 2018	(Biraud et al., 2022)
US-Atq	WET	2003 - 2008	(Zona and Oechel, 2016a)
US-Bar	DBF	2005 - 2017	(Richardson and Hollinger, 2023)
US-Blo	ENF	2001 - 2007	(Goldstein, 2016)
US-Cop	CRO	2011 - 2013	(Bowling, 2016)
US-CRT	GRA	2001 - 2007	(Chen and Chu, 2023)
US-Dk1	GRA	2004 - 2008	(Oishi et al., 2016a)
US-Dk2	DBF	2004 - 2008	(Oishi et al., 2016b)
US-Dk3	ENF	2004 - 2008	(Oishi et al., 2016c)
US-Fmf	WSA	2005 - 2008	(Dore and Kolb, 2023a)
US-FR2	ENF	2005 - 2010	(Litvak, 2016)
US-Fuf	ENF	2005 - 2010	(Dore and Kolb, 2023b)
US-GBT	ENF	2001 - 2003	(Massman, 2016a)
US-GLE	ENF	2005 - 2014	(Massman, 2016b)
US-Goo	GRA	2002 - 2006	(Meyers, 2016)
US-Ha1	DBF	2001 - 2012	(Munger, 2016)
US-Ho1	ENF	2012 - 2018	(Hollinger, 2016)
US-Ivo	WET	2004 - 2007	(Zona and Oechel, 2016b)
US-KFS	GRA	2009 - 2017	(Brunsell, 2022)
US-KS2	CSH	2003 - 2006	(Drake and Hinkle, 2016)
US-Los	WET	2001 - 2014	(Desai, 2016a)
US-Me2	DBF	2001 - 2017	(Law, 2022)
US-Me3	ENF	2003 - 2017	(Law, 2016a)
US-Me5	ENF	2004 - 2009	(Law, 2016b)
US-Me6	ENF	2001 - 2002	(Law, 2016c)
US-MMS	ENF	2010 - 2014	(Novick and Phillips, 2022)
US-Mpj	OSH	2008 - 2017	(Litvak, 2021)
US-Myb	WET	2011 - 2014	(Sturtevant et al., 2016)
US-Ne1	ENF	2001 - 2014	(Suyker, 2016a)
US-Ne2	CRO	2001 - 2013	(Suyker, 2016b)
US-Ne3	CRO	2001 - 2013	(Suyker, 2016c)
US-NR1	CRO	2001 - 2013	(Blanken et al., 2016)
US-Oho	DBF	2004 - 2013	(Chen et al., 2023)

US-PFa	MF	2001 - 2014	(Desai, 2016b)
US-Prr	ENF	2010 - 2016	(Iwahana et al., 2016)
US-Rls	CSH	2014 - 2017	(Flerchinger, 2023)
US-Rms	CSH	2014 - 2017	(Flerchinger, 2022a)
US-Ro1	CRO	2004 - 2016	(Baker et al., 2022)
US-Rws	OSH	2014 - 2017	(Flerchinger, 2022b)
US-Seg	MF	2008 - 2014	(Litvak, 2023a)
US-Ses	WSA	2004 - 2014	(Litvak, 2023b)
US-SRC	GRA	2007 - 2017	(Kurc, 2016)
US-SRM	OSH	2007 - 2017	(Scott, 2016a)
US-Sta	OSH	2005 - 2009	(Ewers and Pendall, 2016)
US-Syv	MF	2001 - 2014	(Desai, 2016c)
US-Ton	WSA	2001 - 2014	(Baldocchi and Ma, 2016)
US-Tw1	WET	2011 - 2017	(Valach et al., 2021)
US-Tw4	WET	2014 - 2017	(Eichelmann et al., 2023)
US-Twt	CRO	2009 - 2014	(Baldocchi, 2016)
US-Uaf	DBF	2007 - 2017	(Ueyama et al., 2018)
US-UMB	DBF	2008 - 2017	(Gough et al., 2023)
US-UMd	ENF	2003 - 2017	(Gough et al., 2022)
US-Var	GRA	2001 - 2014	(Baldocchi et al., 2016)
US-Vcm	ENF	2008 - 2017	(Litvak, 2023c)
US-Vcp	ENF	2007 - 2017	(Litvak, 2023d)
US-WCr	DBF	2001 - 2014	(Desai, 2016d)
US-Whs	WET	2011 - 2013	(Scott, 2016b)
US-Wi3	OSH	2007 - 2014	(Chen, 2016a)
US-Wi4	DBF	2002 - 2004	(Chen, 2016b)
US-Wjs	ENF	2002 - 2005	(Litvak, 2022)
US-WPT	SAV	2007 - 2017	(Chen and Chu, 2016)
ZM-Mon	DBF	2007 - 2009	(Kutsch et al., 2016)

957
958

 Appendix B: CO₂ sensitivity function of Light Use Efficiency

960   In the CFE-Hybrid model, the direct CO_2 fertilization effect was prescribed onto machine
961 learning estimated GPP at a reference CO_2 level using a theoretical CO_2 sensitivity function of LUE.
962 The sensitivity function, which describes the fractional change in LUE due to CO_2 relative to the
963 reference period, is described below.

964   The Light Use Efficiency (LUE) model (Monteith, 1972) of GPP states that,

965 $$GPP = APAR \times LUE = PAR \times fAPAR \times LUE \tag{A1}$$

966 where PAR is the photosynthetic active radiation, $fAPAR$ is the fraction of PAR that plant canopy
967 has absorbed, and $APAR$ is the absorbed PAR. Eco-evolutionary theory, specifically the optimal
968 coordination hypothesis, predicts that the electron-transport-limited (light-limited) (A_j) and Rubisco-
969 limited (A_c) rates of photosynthesis converge on the time scale of physiological acclimation, which is
970 in the order of a few weeks (Harrison et al., 2021; Haxeltine and Prentice, 1996; Wang et al., 2017).
971 Thus, at a monthly time scale, we assume that

972 $$A = A_c = A_j \tag{A2}$$

973 where A is the gross photosynthetic rate, here equivalent to GPP.

974   In the following, we derive our sensitivity function based on A_j, which has a smaller response
975 to CO_2 than A_c, thus providing conservative estimates of the direct CO_2 fertilization effect (Walker
976 et al., 2021). According to the Fauquhar, von Caemmerer and Berry (FvCB) model (Farquhar et al.,
977 1980),

978 $$A_j = \varphi_0 I \frac{c_i - \Gamma^*}{c_i + 2\Gamma^*} \tag{A3}$$

979 where φ_0 is the intrinsic quantum efficiency of photosynthesis, I is the absorbed PAR ($I = APAR$),
980 c_i is the leaf-internal partial pressure of CO_2, and Γ^* is the photorespiratory compensation point that
981 depends on temperature:

982 $$\Gamma^* = r_{25} e^{\frac{\Delta H(T - 298.15)}{298.15RT}} \tag{A4}$$

983 where $r_{25} = 4.22 \, Pa$ is the photorespiratory point at 25 °C, ΔH is the activation energy ($37.83 \cdot 10^3$
984 J mol⁻¹), T is the air temperature in Kelvin, and R is the molar gas constant (8.314 J mol⁻¹ K⁻¹). We
985 denote atmospheric CO_2 concentration as c_a, and χ is the ratio of leaf internal and external CO_2, so

986 $$c_i = \chi c_a \tag{A5}$$

987 Combing (A1), (A3), (A5), and assuming (A2), LUE can be written as,

$$LUE = \varphi_0 \frac{c_i - \Gamma^*}{c_i + 2\Gamma^*} = \varphi_0 \frac{\chi c_a - \Gamma^*}{\chi c_a + 2\Gamma^*} \tag{A6}$$

988

989 We can therefore show that under constant absorbed light (I or $APAR$), the sensitivity of GPP to CO_2

990 is proportional to that of LUE,

$$\frac{\partial GPP}{\partial c_a} = \frac{\partial \varphi_0 I \frac{\chi c_a - \Gamma^*}{\chi c_a + 2\Gamma^*}}{\partial c_a} = I \frac{\partial LUE}{\partial c_a} \tag{A7}$$

991

992 Thus from (A7), we can express the actual GPP at the time t and a CO_2 level c_a^t as the product of a

993 reference GPP with a CO_2 level c_a^0 and the ratio between actual and reference LUE (A8-9). We denote

994 the actual GPP as time t as $GPP^t_{c_a = c_a^t}$, and the reference GPP at time t as $GPP^t_{c_a = c_a^0}$.

$$\frac{GPP^t_{c_a = c_a^t}}{GPP^t_{c_a = c_a^0}} = \frac{LUE^t_{c_a = c_a^t}}{LUE^t_{c_a = c_a^0}} = \frac{\frac{\chi c_a^t - \Gamma^*}{\chi c_a^t + 2\Gamma^*}}{\frac{\chi c_a^0 - \Gamma^*}{\chi c_a^0 + 2\Gamma^*}} = \frac{\phi^t_{CO2}}{\phi^{t0}_{CO2}} \tag{A8}$$

995

$$GPP^t_{c_a = c_a^t} = GPP^t_{c_a = c_a^0} \times \frac{\phi^t_{CO2}}{\phi^{t0}_{CO2}} \tag{A9}$$

996

997 The reference GPP represents the GPP value at time t if the CO_2 were at the level of a reference

998 level, while all other factors, such as PAR, $fAPAR$, temperature, and other environmental controls

999 remain unchanged. Here the CO_2 impacts on LUE depend on atmospheric CO_2 (c_a), χ, and air

1000 temperature. We fixed χ to the global long-term average value 0.7 typical to C3 plants (Prentice et al.,

1001 2014; Wang et al., 2017). We further tested a dynamic model that quantified χ as a function of air

1002 temperature and vapor pressure deficit following an eco-evolutionary theory across global flux sites

1003 (Keenan et al., 2023). The estimated χ had a mean and median of 0.7 and a standard deviation of 0.04

1004 (Figure S21a). Differences in the direct CO_2 effect between the dynamic and fixed χ approaches were

1005 minimal, with an R^2 of 0.99 and a slope of 0.99 from a least squares linear regression line (Figure S21b).

1006 GPP trends across flux towers were also highly consistent between the two approaches, with a

1007 difference less than 0.1 gC m^{-2} year^{-2} (Figure S21b, c). Since these results indicated that χ is relatively

1008 stable, we used the fixed χ approach to produce the CEDAR-GPP dataset.

1009 In the CFE-Hybrid model, we estimated the reference GPP by fixing the CO_2 at the level of the

1010 year 2001 while keeping all other variables dynamic in the CFE-ML model. Then the actual GPP can

1011 be estimated following (A9). Fixing CO_2 values to the 2001 level, the start year of eddy covariance

1012 data used in model training, essentially removed the effects of CO_2 inferred by the CFE-ML model.

Supplement

The supplement related to this article is available online.

Author contributions

T. K. and Y. K. conceptualized the study. Y. K. performed the formal analysis and generated the final product. Y. K., T. K., M. B., and M. G. contributed to the development and investigation of the research. Y. K., M. G., and X. L. contributed to data curation and processing. Y. K. prepared the manuscript with contributions from all co-authors. T. K. supervised the project.

Competing interests

The authors declare that they have no conflict of interest.

Acknowledgments

We are grateful to Dr. Youngryel Ryu for providing the BESS_Rad dataset and Dr. Martin Jung for sharing the FLUXCOM-RS006 dataset. We also thank Dr. Muyi Li, Dr. Zaichun Zhu, and Dr. Sen Cao for sharing early versions of the PKU GIMMS NDVI4g and LAI4g datasets with us. We extend our gratitude to four reviewers for their constructive feedback for improving this paper.

Financial support

This research was supported by the U.S. Department of Energy Office of Science Early Career Research Program award #DE-SC0021023 and a NASA Award 80NSSC21K1705. YK acknowledges additional support from a NASA award 80NSSC24K1562. TFK acknowledges further support from the LEMONTREE (Land Ecosystem Models based On New Theory, obseRvations and ExperimEnts) project, funded through the generosity of Eric and Wendy Schmidt by recommendation of the Schmidt Futures programme, support from the RUBISCO SFA, which is sponsored by the Regional and Global Model Analysis (RGMA) Program in the Climate and Environmental Sciences Division (CESD) of the Office of Biological and Environmental Research (BER) in the U.S. Department of Energy Office of Science, and NASA awards 80NSSC20K1801 and 80NSSC25K7327. MB acknowledges additional support from the U.S. Department of Agriculture NIFA award #2023-67012-40086.

References

1040 Amiro, B.: FLUXNET2015 CA-Man Manitoba - Northern Old Black Spruce (former BOREAS
1041 Northern Study Area), https://doi.org/10.18140/FLX/1440035, 2016a.

1042 Amiro, B.: FLUXNET2015 CA-SF1 Saskatchewan - Western Boreal, forest burned in 1977,
1043 https://doi.org/10.18140/FLX/1440046, 2016b.

1044 Amiro, B.: FLUXNET2015 CA-SF3 Saskatchewan - Western Boreal, forest burned in 1998,
1045 https://doi.org/10.18140/FLX/1440048, 2016c.

1046 Amiro, B.: AmeriFlux FLUXNET-1F CA-SF2 Saskatchewan - Western Boreal, forest burned in 1989,
1047 https://doi.org/10.17190/AMF/2006961, 2023.

1048 Ammann, C.: FLUXNET2015 CH-Oe1 Oensingen grassland,
1049 https://doi.org/10.18140/FLX/1440135, 2016.

1050 Anav, A., Friedlingstein, P., Beer, C., Ciais, P., Harper, A., Jones, C., Murray-Tortarolo, G., Papale, D.,
1051 Parazoo, N. C., Peylin, P., Piao, S., Sitch, S., Viovy, N., Wiltshire, A., and Zhao, M.: Spatiotemporal
1052 patterns of terrestrial gross primary production: A review, Reviews of Geophysics, 1–34,
1053 https://doi.org/10.1002/2015RG000483, 2015.

1054 Apley, D. W. and Zhu, J.: Visualizing the Effects of Predictor Variables in Black Box Supervised
1055 Learning Models, Journal of the Royal Statistical Society Series B: Statistical Methodology, 82, 1059–
1056 1086, https://doi.org/10.1111/rssb.12377, 2020.

1057 Arain, M. A.: AmeriFlux AmeriFlux CA-TP4 Ontario - Turkey Point 1939 Plantation White Pine,
1058 https://doi.org/10.17190/AMF/1246012, 2016a.

1059 Arain, M. A.: FLUXNET2015 CA-TP1 Ontario - Turkey Point 2002 Plantation White Pine,
1060 https://doi.org/10.18140/FLX/1440050, 2016b.

1061 Arain, M. A.: FLUXNET2015 CA-TP2 Ontario - Turkey Point 1989 Plantation White Pine,
1062 https://doi.org/10.18140/FLX/1440051, 2016c.

1063 Arain, M. A.: FLUXNET2015 CA-TP3 Ontario - Turkey Point 1974 Plantation White Pine,
1064 https://doi.org/10.18140/FLX/1440052, 2016d.

1065 Arain, M. A.: FLUXNET2015 CA-TPD Ontario - Turkey Point Mature Deciduous,
1066 https://doi.org/10.18140/FLX/1440112, 2016e.

1067 Ardö, J., El Tahir, B. A., and ElKhidir, H. A. M.: FLUXNET2015 SD-Dem Demokeya,
1068 https://doi.org/10.18140/FLX/1440186, 2016.

1069 Arndt, S., Hinko-Najera, N., Griebel, A., Beringer, J., and Livesley, S. J.: FLUXNET2015 AU-Wom
1070 Wombat, https://doi.org/10.18140/FLX/1440207, 2016.

1071 Aurela, M., Lohila, A., Tuovinen, J.-P., Hatakka, J., Rainne, J., Mäkelä, T., and Lauria, T.:
1072 FLUXNET2015 FI-Lom Lompolojankka, https://doi.org/10.18140/FLX/1440228, 2016a.

1073 Aurela, M., Tuovinen, J.-P., Hatakka, J., Lohila, A., Mäkelä, T., Rainne, J., and Lauria, T.:
1074 FLUXNET2015 FI-Sod Sodankyla, https://doi.org/10.18140/FLX/1440160, 2016b.

1075 Badgley, G., Anderegg, L. D. L., Berry, J. A., and Field, C. B.: Terrestrial gross primary production:
1076 Using NIRV to scale from site to globe, Global Change Biology, 25, 3731–3740,
1077 https://doi.org/10.1111/gcb.14729, 2019.

1078 Baker, J., Griffis, T., and Griffis, T.: AmeriFlux FLUXNET-1F US-Ro1 Rosemount- G21,
1079 https://doi.org/10.17190/AMF/1881588, 2022.

1080 Baldocchi, D.: FLUXNET2015 US-Twt Twitchell Island, https://doi.org/10.18140/FLX/1440106,
1081 2016.

1082 Baldocchi, D. and Ma, S.: FLUXNET2015 US-Ton Tonzi Ranch,
1083 https://doi.org/10.18140/FLX/1440092, 2016.

1084 Baldocchi, D., Ma, S., and Xu, L.: FLUXNET2015 US-Var Vaira Ranch- Ione,
1085 https://doi.org/10.18140/FLX/1440094, 2016.

1086 Baldocchi, D., Chu, H., and Reichstein, M.: Inter-annual variability of net and gross ecosystem carbon
1087 fluxes: A review, Agricultural and Forest Meteorology, 249, 520–533,
1088 https://doi.org/10.1016/j.agrformet.2017.05.015, 2018.

1089 Baldocchi, D. D.: How eddy covariance flux measurements have contributed to our understanding of
1090 Global Change Biology, Global Change Biology, 26, 242–260, https://doi.org/10.1111/gcb.14807,
1091 2020.

1092 Baniecki, H., Kretowicz, W., Piątyszek, P., Wiśniewski, J., and Biecek, P.: dalex: Responsible Machine
1093 Learning with Interactive Explainability and Fairness in Python, Journal of Machine Learning
1094 Research, 22, 1–7, 2021.

1095 Barr, A. and Black, A. T.: AmeriFlux AmeriFlux CA-SJ2 Saskatchewan - Western Boreal, Jack Pine
1096 forest harvested in 2002, https://doi.org/10.17190/AMF/1436321, 2018.

1097 Beck, H. E., Zimmermann, N. E., McVicar, T. R., Vergopolan, N., Berg, A., and Wood, E. F.: Present
1098 and future köppen-geiger climate classification maps at 1-km resolution, Scientific Data, 5, 1–12,
1099 https://doi.org/10.1038/sdata.2018.214, 2018.

1100 Beer, C., Reichstein, M., Tomelleri, E., Ciais, P., Jung, M., Carvalhais, N., Rödenbeck, C., Arain, M.
1101 A., Baldocchi, D., Bonan, G. B., Bondeau, A., Cescatti, A., Lasslop, G., Lindroth, A., Lomas, M.,
1102 Luyssaert, S., Margolis, H., Oleson, K. W., Roupsard, O., Veenendaal, E., Viovy, N., Williams, C.,
1103 Woodward, F. I., and Papale, D.: Terrestrial gross carbon dioxide uptake: Global distribution and
1104 covariation with climate, Science, 329, 834–838, https://doi.org/10.1126/science.1184984, 2010.

1105 Belelli, L., Papale, D., and Valentini, R.: FLUXNET2015 RU-Ha1 Hakasia steppe,
1106 https://doi.org/10.18140/FLX/1440184, 2016.

1107 Berbigier, P., Loustau, D., Bonnefond, J. M., Bosc, A., and Trichet, P.: FLUXNET2015 FR-LBr Le
1108 Bray, https://doi.org/10.18140/FLX/1440163, 2016.

Berdugo, M., Gaitán, J. J., Delgado-Baquerizo, M., Crowther, T. W., and Dakos, V.: Prevalence and drivers of abrupt vegetation shifts in global drylands, Proceedings of the National Academy of Sciences, 119, e2123393119, https://doi.org/10.1073/pnas.2123393119, 2022.

Beringer, J. and Hutley, L.: FLUXNET2015 AU-Ade Adelaide River, https://doi.org/10.18140/FLX/1440193, 2016a.

Beringer, J. and Hutley, L.: FLUXNET2015 AU-DaP Daly River Savanna, https://doi.org/10.18140/FLX/1440123, 2016b.

Beringer, J. and Hutley, L.: FLUXNET2015 AU-Dry Dry River, https://doi.org/10.18140/FLX/1440197, 2016c.

Beringer, J. and Hutley, L.: FLUXNET2015 AU-Fog Fogg Dam, https://doi.org/10.18140/FLX/1440124, 2016d.

Beringer, J. and Hutley, L.: FLUXNET2015 AU-How Howard Springs, https://doi.org/10.18140/FLX/1440125, 2016e.

Beringer, J. and Hutley, L.: FLUXNET2015 AU-RDF Red Dirt Melon Farm, Northern Territory, https://doi.org/10.18140/FLX/1440201, 2016f.

Beringer, J. and Hutley, P. L.: FLUXNET2015 AU-DaS Daly River Cleared, https://doi.org/10.18140/FLX/1440122, 2016g.

Beringer, J. and Walker, J.: FLUXNET2015 AU-Ync Jaxa, https://doi.org/10.18140/FLX/1440208, 2016.

Beringer, J., Cunningham, S., Baker, P., Cavagnaro, T., MacNally, R., Thompson, R., and McHugh, I.: FLUXNET2015 AU-Rig Riggs Creek, https://doi.org/10.18140/FLX/1440202, 2016a.

Beringer, J., Hutley, L., McGuire, D., U, P., and McHugh, I.: FLUXNET2015 AU-Wac Wallaby Creek, https://doi.org/10.18140/FLX/1440127, 2016b.

Beringer, J., Cunningham, S., Baker, P., Cavagnaro, T., MacNally, R., Thompson, R., and McHugh, I.: FLUXNET2015 AU-Whr Whroo, https://doi.org/10.18140/FLX/1440206, 2016c.

Bernhofer, C., Grünwald, T., Moderow, U., Hehn, M., Eichelmann, U., Prasse, H., and Postel, U.: FLUXNET2015 DE-Spw Spreewald, https://doi.org/10.18140/FLX/1440220, 2016.

Besnard, S., Carvalhais, N., Altaf Arain, M., Black, A., Brede, B., Buchmann, N., Chen, J., Clevers, J. G. P. W., Dutrieux, L. P., Gans, F., Herold, M., Jung, M., Kosugi, Y., Knohl, A., Law, B. E., Paul-Limoges, E., Lohila, A., Merbold, L., Roupsard, O., Valentini, R., Wolf, S., Zhang, X., and Reichstein, M.: Memory effects of climate and vegetation affecting net ecosystem CO_2 fluxes in global forests, PLoS ONE, 14, 1–22, https://doi.org/10.1371/journal.pone.0211510, 2019.

Biraud, S., Fischer, M., Chan, S., and Torn, M.: AmeriFlux FLUXNET-1F US-ARM ARM Southern Great Plains site- Lamont, https://doi.org/10.17190/AMF/1854366, 2022.

Black, T. A.: FLUXNET2015 CA-Oas Saskatchewan - Western Boreal, Mature Aspen, https://doi.org/10.18140/FLX/1440043, 2016a.

Black, T. A.: FLUXNET2015 CA-Obs Saskatchewan - Western Boreal, Mature Black Spruce, https://doi.org/10.18140/FLX/1440044, 2016b.

Black, T. A.: AmeriFlux AmeriFlux CA-Ca3 British Columbia - Pole sapling Douglas-fir stand, https://doi.org/10.17190/AMF/1480302, 2018.

Black, T. A.: AmeriFlux FLUXNET-1F CA-Ca1 British Columbia - 1949 Douglas-fir stand, https://doi.org/10.17190/AMF/2007163, 2023a.

Black, T. A.: AmeriFlux FLUXNET-1F CA-Ca2 British Columbia - Clearcut Douglas-fir stand (harvested winter 1999/2000), https://doi.org/10.17190/AMF/2007164, 2023b.

Blanken, P. D., Monson, R. K., Burns, S. P., Bowling, D. R., and Turnipseed, A. A.: FLUXNET2015 US-NR1 Niwot Ridge Forest (LTER NWT1), https://doi.org/10.18140/FLX/1440087, 2016.

Bloomfield, K. J., Stocker, B. D., Keenan, T. F., and Prentice, I. C.: Environmental controls on the light use efficiency of terrestrial gross primary production, Global Change Biology, 29, 1037–1053, https://doi.org/10.1111/gcb.16511, 2023.

Bowling, D.: FLUXNET2015 US-Cop Corral Pocket, https://doi.org/10.18140/FLX/1440100, 2016.

Brunsell, N.: AmeriFlux FLUXNET-1F US-KFS Kansas Field Station, https://doi.org/10.17190/AMF/1881585, 2022.

Campbell, J. E., Berry, J. A., Seibt, U., Smith, S. J., Montzka, S. A., Launois, T., Belviso, S., Bopp, L., and Laine, M.: Large historical growth in global terrestrial gross primary production, Nature, 544, 84–87, https://doi.org/10.1038/nature22030, 2017.

Camps-Valls, G., Campos-Taberner, M., Moreno-Martínez, Á., Walther, S., Duveiller, G., Cescatti, A., Mahecha, M. D., Muñoz-Marí, J., García-Haro, F. J., Guanter, L., Jung, M., Gamon, J. A., Reichstein, M., and Running, S. W.: A unified vegetation index for quantifying the terrestrial biosphere, Science Advances, 7, eabc7447, https://doi.org/10.1126/sciadv.abc7447, 2021.

Cao, S., Li, M., Zhu, Z., Zha, J., Zhao, W., Duanmu, Z., Chen, J., Zheng, Y., and Chen, Y.: Spatiotemporally consistent global dataset of the GIMMS Leaf Area Index (GIMMS LAI4g) from 1982 to 2020, Earth System Science Data Discussions, 1–31, https://doi.org/10.5194/essd-2023-68, 2023.

Cescatti, A., Marcolla, B., Zorer, R., and Gianelle, D.: FLUXNET2015 IT-La2 Lavarone2, https://doi.org/10.18140/FLX/1440235, 2016.

Chen, C., Park, T., Wang, X., Piao, S., Xu, B., Chaturvedi, R. K., Fuchs, R., Brovkin, V., Ciais, P., Fensholt, R., Tømmervik, H., Bala, G., Zhu, Z., Nemani, R. R., and Myneni, R. B.: China and India lead in greening of the world through land-use management, Nature Sustainability, 2, 122–129, https://doi.org/10.1038/s41893-019-0220-7, 2019.

Chen, C., Riley, W. J., Prentice, I. C., and Keenan, T. F.: CO2 fertilization of terrestrial photosynthesis inferred from site to global scales, Proceedings of the National Academy of Sciences, 119, 1–8, https://doi.org/10.1073/pnas.2115627119/, 2022.

Chen, J.: FLUXNET2015 US-Wi3 Mature hardwood (MHW), https://doi.org/10.18140/FLX/1440057, 2016a.

Chen, J.: FLUXNET2015 US-Wi4 Mature red pine (MRP), https://doi.org/10.18140/FLX/1440058, 2016b.

Chen, J. and Chu, H.: FLUXNET2015 US-WPT Winous Point North Marsh, https://doi.org/10.18140/FLX/1440116, 2016.

Chen, J. and Chu, H.: AmeriFlux FLUXNET-1F US-CRT Curtice Walter-Berger cropland, https://doi.org/10.17190/AMF/2006974, 2023.

Chen, J., Chu, H., and Noormets, A.: AmeriFlux FLUXNET-1F US-Oho Oak Openings, https://doi.org/10.17190/AMF/2229385, 2023.

Chen, S.: FLUXNET2015 CN-Du2 Duolun_grassland (D01), https://doi.org/10.18140/FLX/1440140, 2016c.

Chen, T. and Guestrin, C.: XGBoost: a scalable tree boosting system, in: Proceedings of the 22nd ACM SIGKDD International Conference on Knowledge Discovery and Data Mining - KDD '16, 785–794, https://doi.org/10.1145/2939672.2939785, 2016.

Christensen, T.: FLUXNET2015 SJ-Adv Adventdalen, https://doi.org/10.18140/FLX/1440241, 2016.

Chu, H., Luo, X., Ouyang, Z., Chan, W. S., Dengel, S., Biraud, S. C., Torn, M. S., Metzger, S., Kumar, J., Arain, M. A., Arkebauer, T. J., Baldocchi, D., Bernacchi, C., Billesbach, D., Black, T. A., Blanken, P. D., Bohrer, G., Bracho, R., Brown, S., Brunsell, N. A., Chen, J., Chen, X., Clark, K., Desai, A. R., Duman, T., Durden, D., Fares, S., Forbrich, I., Gamon, J. A., Gough, C. M., Griffis, T., Helbig, M., Hollinger, D., Humphreys, E., Ikawa, H., Iwata, H., Ju, Y., Knowles, J. F., Knox, S. H., Kobayashi, H., Kolb, T., Law, B., Lee, X., Litvak, M., Liu, H., Munger, J. W., Noormets, A., Novick, K., Oberbauer, S. F., Oechel, W., Oikawa, P., Papuga, S. A., Pendall, E., Prajapati, P., Prueger, J., Quinton, W. L., Richardson, A. D., Russell, E. S., Scott, R. L., Starr, G., Staebler, R., Stoy, P. C., Stuart-Haëntjens, E., Sonnentag, O., Sullivan, R. C., Suyker, A., Ueyama, M., Vargas, R., Wood, J. D., and Zona, D.: Representativeness of Eddy-Covariance flux footprints for areas surrounding AmeriFlux sites, Agricultural and Forest Meteorology, 301–302, https://doi.org/10.1016/j.agrformet.2021.108350, 2021.

Cleverly, J., Eamus, D., and Isaac, P.: FLUXNET2015 AU-ASM Alice Springs, https://doi.org/10.18140/FLX/1440194, 2016.

Dannenberg, M. P., Barnes, M. L., Smith, W. K., Johnston, M. R., Meerdink, S. K., Wang, X., Scott, R. L., and Biederman, J. A.: Upscaling dryland carbon and water fluxes with artificial neural networks of optical, thermal, and microwave satellite remote sensing, Biogeosciences, 20, 383–404, https://doi.org/10.5194/bg-20-383-2023, 2023.

1217 De Kauwe, M. G., Keenan, T. F., Medlyn, B. E., Prentice, I. C., and Terrer, C.: Satellite based estimates
1218 underestimate the effect of CO2 fertilization on net primary productivity, Nature Climate Change, 6,
1219 892–893, https://doi.org/10.1038/nclimate3105, 2016.

1220 Delwiche, K. B., Nelson, J., Kowalska, N., Moore, C. E., Shirkey, G., Tarin, T., Cleverly, J. R., and
1221 Keenan, T. F.: Charting the Future of the FLUXNET Network, Bulletin of the American
1222 Meteorological Society, 105, E466–E473, https://doi.org/10.1175/BAMS-D-23-0316.1, 2024.

1223 Desai, A.: FLUXNET2015 US-Los Lost Creek, https://doi.org/10.18140/FLX/1440076, 2016a.

1224 Desai, A.: FLUXNET2015 US-PFa Park Falls/WLEF, https://doi.org/10.18140/FLX/1440089,
1225 2016b.

1226 Desai, A.: FLUXNET2015 US-Syv Sylvania Wilderness Area,
1227 https://doi.org/10.18140/FLX/1440091, 2016c.

1228 Desai, A.: FLUXNET2015 US-WCr Willow Creek, https://doi.org/10.18140/FLX/1440095, 2016d.

1229 Dolman, H., Hendriks, D., Parmentier, F.-J., Marchesini, L. B., Dean, J., and van Huissteden, K.:
1230 FLUXNET2015 NL-Hor Horstermeer, https://doi.org/10.18140/FLX/1440177, 2016a.

1231 Dolman, H., van der Molen, M., Parmentier, F.-J., Marchesini, L. B., Dean, J., van Huissteden, K., and
1232 Maximov, T.: FLUXNET2015 RU-Cok Chokurdakh, https://doi.org/10.18140/FLX/1440182,
1233 2016b.

1234 Dong, G.: FLUXNET2015 CN-Cng Changling, https://doi.org/10.18140/FLX/1440209, 2016.

1235 Dong, Y., Li, J., Jiao, Z., Liu, Q., Zhao, J., Xu, B., Zhang, H., Zhang, Z., Liu, C., Knyazikhin, Y., and
1236 Myneni, R. B.: A Method for Retrieving Coarse-Resolution Leaf Area Index for Mixed Biomes Using
1237 a Mixed-Pixel Correction Factor, IEEE Transactions on Geoscience and Remote Sensing, 61, 1–17,
1238 https://doi.org/10.1109/TGRS.2023.3235949, 2023.

1239 Dore, S. and Kolb, T.: AmeriFlux FLUXNET-1F US-Fmf Flagstaff - Managed Forest,
1240 https://doi.org/10.17190/AMF/2007173, 2023a.

1241 Dore, S. and Kolb, T.: AmeriFlux FLUXNET-1F US-Fuf Flagstaff - Unmanaged Forest,
1242 https://doi.org/10.17190/AMF/2007174, 2023b.

1243 Dorigo, W., Wagner, W., Albergel, C., Albrecht, F., Balsamo, G., Brocca, L., Chung, D., Ertl, M.,
1244 Forkel, M., Gruber, A., Haas, E., Hamer, P. D., Hirschi, M., Ikonen, J., de Jeu, R., Kidd, R., Lahoz,
1245 W., Liu, Y. Y., Miralles, D., Mistelbauer, T., Nicolai-Shaw, N., Parinussa, R., Pratola, C., Reimer, C.,
1246 van der Schalie, R., Seneviratne, S. I., Smolander, T., and Lecomte, P.: ESA CCI Soil Moisture for
1247 improved Earth system understanding: State-of-the art and future directions, Remote Sensing of
1248 Environment, 203, 185–215, https://doi.org/10.1016/j.rse.2017.07.001, 2017.

1249 Dorigo, W. A., Gruber, A., De Jeu, R. A. M., Wagner, W., Stacke, T., Loew, A., Albergel, C., Brocca,
1250 L., Chung, D., Parinussa, R. M., and Kidd, R.: Evaluation of the ESA CCI soil moisture product using
1251 ground-based observations, Remote Sensing of Environment, 162,
1252 https://doi.org/10.1016/j.rse.2014.07.023, 2015.

Drake, B. and Hinkle, R.: FLUXNET2015 US-KS2 Kennedy Space Center (scrub oak), https://doi.org/10.18140/FLX/1440075, 2016.

Drought 2018 Team: Drought-2018 ecosystem eddy covariance flux product for 52 stations in FLUXNET-Archive format, https://doi.org/10.18160/YVR0-4898, 2020.

Ehlers, I., Augusti, A., Betson, T. R., Nilsson, M. B., Marshall, J. D., and Schleucher, J.: Detecting long-term metabolic shifts using isotopomers: CO2-driven suppression of photorespiration in C3 plants over the 20th century, Proceedings of the National Academy of Sciences, 112, 15585–15590, https://doi.org/10.1073/pnas.1504493112, 2015.

Eichelmann, E., Shortt, R., Knox, S., Sanchez, C. R., Valach, A., Sturtevant, C., Szutu, D., Verfaillie, J., and Baldocchi, D.: AmeriFlux FLUXNET-1F US-Tw4 Twitchell East End Wetland, https://doi.org/10.17190/AMF/2204881, 2023.

Ewers, B. and Pendall, E.: FLUXNET2015 US-Sta Saratoga, https://doi.org/10.18140/FLX/1440115, 2016.

Fang, H., Baret, F., Plummer, S., and Schaepman-Strub, G.: An overview of global leaf area index (LAI): Methods, products, validation, and applications, Reviews of Geophysics, 2018RG000608, https://doi.org/10.1029/2018RG000608, 2019.

Farquhar, G. D., von Caemmerer, S., and Berry, J. A.: A biochemical model of photosynthetic CO2 assimilation in leaves of C3 species, Planta, 149, 78–90, https://doi.org/10.1007/BF00386231, 1980.

Fernández-Martínez, M., Vicca, S., Janssens, I. A., Ciais, P., Obersteiner, M., Bartrons, M., Sardans, J., Verger, A., Canadell, J. G., Chevallier, F., Wang, X., Bernhofer, C., Curtis, P. S., Gianelle, D., Grünwald, T., Heinesch, B., Ibrom, A., Knohl, A., Laurila, T., Law, B. E., Limousin, J. M., Longdoz, B., Loustau, D., Mammarella, I., Matteucci, G., Monson, R. K., Montagnani, L., Moors, E. J., Munger, J. W., Papale, D., Piao, S. L., and Peñuelas, J.: Atmospheric deposition, CO2, and change in the land carbon sink, Sci Rep, 7, 9632, https://doi.org/10.1038/s41598-017-08755-8, 2017.

Flanagan, L. B.: AmeriFlux AmeriFlux CA-WP1 Alberta - Western Peatland - LaBiche River,Black Spruce/Larch Fen, https://doi.org/10.17190/AMF/1436323, 2018a.

Flanagan, L. B.: AmeriFlux AmeriFlux CA-WP2 Alberta - Western Peatland - Poor Fen (Sphagnum moss), https://doi.org/10.17190/AMF/1436324, 2018b.

Flanagan, L. B.: AmeriFlux AmeriFlux CA-WP3 Alberta - Western Peatland - Rich Fen (Carex), https://doi.org/10.17190/AMF/1436325, 2018c.

Flerchinger, G.: AmeriFlux FLUXNET-1F US-Rms RCEW Mountain Big Sagebrush, https://doi.org/10.17190/AMF/1881587, 2022a.

Flerchinger, G.: AmeriFlux FLUXNET-1F US-Rws Reynolds Creek Wyoming big sagebrush, https://doi.org/10.17190/AMF/1881592, 2022b.

Flerchinger, G.: AmeriFlux FLUXNET-1F US-Rls RCEW Low Sagebrush, https://doi.org/10.17190/AMF/2229387, 2023.

Friedl, M. and Sulla-Menashe, D.: MCD12Q1 MODIS/Terra+Aqua Land Cover Type Yearly L3 Global 500m SIN Grid V006 [Data set], NASA EOSDIS Land Processes DAAC, https://doi.org/10.5067/MODIS/MCD12Q1.006, 2019.

Friedlingstein, P., Meinshausen, M., Arora, V. K., Jones, C. D., Anav, A., Liddicoat, S. K., and Knutti, R.: Uncertainties in CMIP5 climate projections due to carbon cycle feedbacks, Journal of Climate, 27, 511–526, https://doi.org/10.1175/JCLI-D-12-00579.1, 2014.

Friedlingstein, P., O'Sullivan, M., Jones, M. W., Andrew, R. M., Gregor, L., Hauck, J., Le Quéré, C., Luijkx, I. T., Olsen, A., Peters, G. P., Peters, W., Pongratz, J., Schwingshackl, C., Sitch, S., Canadell, J. G., Ciais, P., Jackson, R. B., Alin, S. R., Alkama, R., Arneth, A., Arora, V. K., Bates, N. R., Becker, M., Bellouin, N., Bittig, H. C., Bopp, L., Chevallier, F., Chini, L. P., Cronin, M., Evans, W., Falk, S., Feely, R. A., Gasser, T., Gehlen, M., Gkritzalis, T., Gloege, L., Grassi, G., Gruber, N., Gürses, Ö., Harris, I., Hefner, M., Houghton, R. A., Hurtt, G. C., Iida, Y., Ilyina, T., Jain, A. K., Jersild, A., Kadono, K., Kato, E., Kennedy, D., Klein Goldewijk, K., Knauer, J., Korsbakken, J. I., Landschützer, P., Lefèvre, N., Lindsay, K., Liu, J., Liu, Z., Marland, G., Mayot, N., McGrath, M. J., Metzl, N., Monacci, N. M., Munro, D. R., Nakaoka, S.-I., Niwa, Y., O'Brien, K., Ono, T., Palmer, P. I., Pan, N., Pierrot, D., Pocock, K., Poulter, B., Resplandy, L., Robertson, E., Rödenbeck, C., Rodriguez, C., Rosan, T. M., Schwinger, J., Séférian, R., Shutler, J. D., Skjelvan, I., Steinhoff, T., Sun, Q., Sutton, A. J., Sweeney, C., Takao, S., Tanhua, T., Tans, P. P., Tian, X., Tian, H., Tilbrook, B., Tsujino, H., Tubiello, F., van der Werf, G. R., Walker, A. P., Wanninkhof, R., Whitehead, C., Willstrand Wranne, A., et al.: Global Carbon Budget 2022, Earth System Science Data, 14, 4811–4900, 2023.

Gaber, M., Kang, Y., Schurgers, G., and Keenan, T.: Using automated machine learning for the upscaling of gross primary productivity, Biogeosciences, 21, 2447–2472, https://doi.org/10.5194/bg-21-2447-2024, 2024.

Gampe, D., Zscheischler, J., Reichstein, M., Sullivan, M. O., Smith, W. K., Sitch, S., and Buermann, W.: Increasing impact of warm droughts on northern ecosystem productivity over recent decades, Nature Climate Change, https://doi.org/10.1038/s41558-021-01112-8, 2021.

Gao, B. C.: NDWI - A normalized difference water index for remote sensing of vegetation liquid water from space, Remote Sensing of Environment, 58, 257–266, https://doi.org/10.1016/S0034-4257(96)00067-3, 1996.

Garcia, A., Di Bella, C., Houspanossian, J., Magliano, P., Jobbágy, E., Posse, G., Fernández, R., and Nosetto, M.: FLUXNET2015 AR-SLu San Luis, 2016.

Gitelson, A. A.: Remote estimation of leaf area index and green leaf biomass in maize canopies, Geophysical Research Letters, 30, 1248, https://doi.org/10.1029/2002GL016450, 2003.

Goldstein, A.: FLUXNET2015 US-Blo Blodgett Forest, https://doi.org/10.18140/FLX/1440068, 2016.

Gough, C., Bohrer, G., and Curtis, P.: AmeriFlux FLUXNET-1F US-UMd UMBS Disturbance, https://doi.org/10.17190/AMF/1881597, 2022.

Gough, C., Bohrer, G., and Curtis, P.: AmeriFlux FLUXNET-1F US-UMB Univ. of Mich. Biological Station, https://doi.org/10.17190/AMF/2204882, 2023.

Goulden, M.: FLUXNET2015 BR-Sa3 Santarem-Km83-Logged Forest, https://doi.org/10.18140/FLX/1440033, 2016a.

Goulden, M.: FLUXNET2015 CA-NS4 UCI-1964 burn site wet, https://doi.org/10.18140/FLX/1440039, 2016b.

Goulden, M.: FLUXNET2015 CA-NS7 UCI-1998 burn site, https://doi.org/10.18140/FLX/1440042, 2016c.

Goulden, M.: AmeriFlux FLUXNET-1F CA-NS1 UCI-1850 burn site, https://doi.org/10.17190/AMF/1902824, 2022a.

Goulden, M.: AmeriFlux FLUXNET-1F CA-NS2 UCI-1930 burn site, https://doi.org/10.17190/AMF/1902825, 2022b.

Goulden, M.: AmeriFlux FLUXNET-1F CA-NS3 UCI-1964 burn site, https://doi.org/10.17190/AMF/1902826, 2022c.

Goulden, M.: AmeriFlux FLUXNET-1F CA-NS5 UCI-1981 burn site, https://doi.org/10.17190/AMF/1902828, 2022d.

Goulden, M.: AmeriFlux FLUXNET-1F CA-NS6 UCI-1989 burn site, https://doi.org/10.17190/AMF/1902829, 2022e.

Green, J. K., Ballantyne, A., Abramoff, R., Gentine, P., Makowski, D., and Ciais, P.: Surface temperatures reveal the patterns of vegetation water stress and their environmental drivers across the tropical Americas, Global Change Biology, 28, 2940–2955, https://doi.org/10.1111/gcb.16139, 2022.

Gruber, A., Scanlon, T., Van Der Schalie, R., Wagner, W., and Dorigo, W.: Evolution of the ESA CCI Soil Moisture climate data records and their underlying merging methodology, Earth System Science Data, 11, 717–739, https://doi.org/10.5194/essd-11-717-2019, 2019.

Gruening, C., Goded, I., Cescatti, A., Manca, G., and Seufert, G.: FLUXNET2015 IT-SRo San Rossore, https://doi.org/10.18140/FLX/1440176, 2016.

Hansen, B. U.: FLUXNET2015 GL-NuF Nuuk Fen, https://doi.org/10.18140/FLX/1440222, 2016.

Hao, D., Bisht, G., Huang, M., Ma, P.-L., Tesfa, T., Lee, W.-L., Gu, Y., and Leung, L. R.: Impacts of Sub-Grid Topographic Representations on Surface Energy Balance and Boundary Conditions in the E3SM Land Model: A Case Study in Sierra Nevada, Journal of Advances in Modeling Earth Systems, 14, e2021MS002862, https://doi.org/10.1029/2021MS002862, 2022.

Harrison, S. P., Cramer, W., Franklin, O., Prentice, I. C., Wang, H., Brännström, Å., de Boer, H., Dieckmann, U., Joshi, J., Keenan, T. F., Lavergne, A., Manzoni, S., Mengoli, G., Morfopoulos, C., Peñuelas, J., Pietsch, S., Rebel, K. T., Ryu, Y., Smith, N. G., Stocker, B. D., and Wright, I. J.: Eco-evolutionary optimality as a means to improve vegetation and land-surface models, New Phytologist, https://doi.org/10.1111/nph.17558, 2021.

Haverd, V., Smith, B., Canadell, J. G., Cuntz, M., Mikaloff-Fletcher, S., Farquhar, G., Woodgate, W., Briggs, P. R., and Trudinger, C. M.: Higher than expected CO2 fertilization inferred from leaf to global observations, Global Change Biology, 26, 2390–2402, https://doi.org/10.1111/gcb.14950, 2020.

Haxeltine, A. and Prentice, I. C.: A General Model for the Light-Use Efficiency of Primary Production, Functional Ecology, 10, 551–561, https://doi.org/10.2307/2390165, 1996.

Hollinger, D.: AmeriFlux AmeriFlux US-Ho1 Howland Forest (main tower), https://doi.org/10.17190/AMF/1246061, 2016.

van der Horst, S. V. J., Pitman, A. J., De Kauwe, M. G., Ukkola, A., Abramowitz, G., and Isaac, P.: How representative are FLUXNET measurements of surface fluxes during temperature extremes?, Biogeosciences, 16, 1829–1844, https://doi.org/10.5194/bg-16-1829-2019, 2019.

Iwahana, G., Kobayashi, H., Ikawa, H., and Suzuki, R.: AmeriFlux AmeriFlux US-Prr Poker Flat Research Range Black Spruce Forest, https://doi.org/10.17190/AMF/1246153, 2016.

Jiang, C., Ryu, Y., Fang, H., Myneni, R., Claverie, M., and Zhu, Z.: Inconsistencies of interannual variability and trends in long-term satellite leaf area index products, Global Change Biology, 23, 4133–4146, https://doi.org/10.1111/gcb.13787, 2017.

Joiner, J. and Yoshida, Y.: Satellite-based reflectances capture large fraction of variability in global gross primary production (GPP) at weekly time scales, Agricultural and Forest Meteorology, 291, 108092, https://doi.org/10.1016/j.agrformet.2020.108092, 2020.

Jung, M., Reichstein, M., Margolis, H. A., Cescatti, A., Richardson, A. D., Arain, M. A., Arneth, A., Bernhofer, C., Bonal, D., Chen, J., Gianelle, D., Gobron, N., Kiely, G., Kutsch, W., Lasslop, G., Law, B. E., Lindroth, A., Merbold, L., Montagnani, L., Moors, E. J., Papale, D., Sottocornola, M., Vaccari, F., and Williams, C.: Global patterns of land-atmosphere fluxes of carbon dioxide , latent heat , and sensible heat derived from eddy covariance , satellite , and meteorological observations, Journal of Geophysical Research: Biogeosciences, 116, 1–16, https://doi.org/10.1029/2010JG001566, 2011.

Jung, M., Reichstein, M., Schwalm, C. R., Huntingford, C., Sitch, S., Ahlström, A., Arneth, A., Camps-Valls, G., Ciais, P., Friedlingstein, P., Gans, F., Ichii, K., Jain, A. K., Kato, E., Papale, D., Poulter, B., Raduly, B., Rödenbeck, C., Tramontana, G., Viovy, N., Wang, Y. P., Weber, U., Zaehle, S., and Zeng, N.: Compensatory water effects link yearly global land CO 2 sink changes to temperature, Nature, 541, 516–520, https://doi.org/10.1038/nature20780, 2017.

Jung, M., Schwalm, C., Migliavacca, M., Walther, S., Camps-Valls, G., Koirala, S., Anthoni, P., Besnard, S., Bodesheim, P., Carvalhais, N., Chevallier, F., Gans, F., S Goll, D., Haverd, V., Köhler, P., Ichii, K., K Jain, A., Liu, J., Lombardozzi, D., E M S Nabel, J., A Nelson, J., O'Sullivan, M., Pallandt, M., Papale, D., Peters, W., Pongratz, J., Rödenbeck, C., Sitch, S., Tramontana, G., Walker, A., Weber, U., and Reichstein, M.: Scaling carbon fluxes from eddy covariance sites to globe: Synthesis and evaluation of the FLUXCOM approach, Biogeosciences, 17, 1343–1365, https://doi.org/10.5194/bg-17-1343-2020, 2020.

Kang, Y., Ozdogan, M., Zhu, X., Ye, Z., Hain, C., and Anderson, M.: Comparative assessment of environmental variables and machine learning algorithms for maize yield prediction in the US Midwest, Environmental Research Letters, 15, https://doi.org/10.1088/1748-9326/ab7df9, 2020.

Kang, Y., Bassiouni, M., Gaber, M., Lu, X., and Keenan, T.: CEDAR-GPP: A Spatiotemporally Upscaled Dataset of Gross Primary Productivity Incorporating CO2 Fertilization (v1.0), https://doi.org/10.5281/zenodo.8212706, 2024.

Keeling, R. F., Graven, H. D., Welp, L. R., Resplandy, L., Bi, J., Piper, S. C., Sun, Y., Bollenbacher, A., and Meijer, H. A. J.: Atmospheric evidence for a global secular increase in carbon isotopic discrimination of land photosynthesis, Proceedings of the National Academy of Sciences of the United States of America, 114, 10361–10366, https://doi.org/10.1073/pnas.1619240114, 2017.

Keenan, T. F., Hollinger, D. Y., Bohrer, G., Dragoni, D., Munger, J. W., Schmid, H. P., and Richardson, A. D.: Increase in forest water-use efficiency as atmospheric carbon dioxide concentrations rise, Nature, 499, 324–327, https://doi.org/10.1038/nature12291, 2013.

Keenan, T. F., Prentice, I. C., Canadell, J. G., Williams, C. A., Wang, H., Raupach, M., and Collatz, G. J.: Recent pause in the growth rate of atmospheric CO2 due to enhanced terrestrial carbon uptake, Nature Communications, 7, 1–9, https://doi.org/10.1038/ncomms13428, 2016.

Keenan, T. F., Migliavacca, M., Papale, D., Baldocchi, D., Reichstein, M., Torn, M., and Wutzler, T.: Widespread inhibition of daytime ecosystem respiration, Nature Ecology and Evolution, 3, 407–415, https://doi.org/10.1038/s41559-019-0809-2, 2019.

Keenan, T. F., Luo, X., Stocker, B. D., De Kauwe, M. G., Medlyn, B. E., Prentice, I. C., Smith, N. G., Terrer, C., Wang, H., Zhang, Y., and Zhou, S.: A constraint on historic growth in global photosynthesis due to rising CO2, Nat. Clim. Chang., 1–6, https://doi.org/10.1038/s41558-023-01867-2, 2023.

Klatt, J., Schmid, H. P., Mauder, M., and Steinbrecher, R.: FLUXNET2015 DE-SfN Schechenfilz Nord, https://doi.org/10.18140/FLX/1440219, 2016.

Knohl, A., Tiedemann, F., Kolle, O., Schulze, E.-D., Anthoni, P., Kutsch, W., Herbst, M., and Siebicke, L.: FLUXNET2015 DE-Lnf Leinefelde, https://doi.org/10.18140/FLX/1440150, 2016.

Kosugi, Y. and Takanashi, S.: FLUXNET2015 MY-PSO Pasoh Forest Reserve (PSO), https://doi.org/10.18140/FLX/1440240, 2016.

Kotani, A.: FLUXNET2015 JP-MBF Moshiri Birch Forest Site, https://doi.org/10.18140/FLX/1440238, 2016a.

Kotani, A.: FLUXNET2015 JP-SMF Seto Mixed Forest Site, https://doi.org/10.18140/FLX/1440239, 2016b.

Kraft, B., Jung, M., Körner, M., Koirala, S., and Reichstein, M.: Towards hybrid modeling of the global hydrological cycle, Hydrology and Earth System Sciences, 26, 1579–1614, https://doi.org/10.5194/hess-26-1579-2022, 2022.

Kurc, S.: FLUXNET2015 US-SRC Santa Rita Creosote, https://doi.org/10.18140/FLX/1440098, 2016.

1436   Kutsch, W. L., Merbold, L., and Kolle, O.: FLUXNET2015 ZM-Mon Mongu,
1437   https://doi.org/10.18140/FLX/1440189, 2016.

1438   Law, B.: FLUXNET2015 US-Me3 Metolius-second young aged pine,
1439   https://doi.org/10.18140/FLX/1440080, 2016a.

1440   Law, B.: FLUXNET2015 US-Me5 Metolius-first young aged pine,
1441   https://doi.org/10.18140/FLX/1440082, 2016b.

1442   Law, B.: FLUXNET2015 US-Me6 Metolius Young Pine Burn,
1443   https://doi.org/10.18140/FLX/1440099, 2016c.

1444   Law, B.: AmeriFlux FLUXNET-1F US-Me2 Metolius mature ponderosa pine,
1445   https://doi.org/10.17190/AMF/1854368, 2022.

1446   Leng, J., Chen, J. M., Li, W., Luo, X., Xu, M., Liu, J., Wang, R., Rogers, C., Li, B., and Yan, Y.: Global
1447   datasets of hourly carbon and water fluxes simulated using a satellite-based process model with
1448   dynamic parameterizations, Earth System Science Data, 16, 1283–1300,
1449   https://doi.org/10.5194/essd-16-1283-2024, 2024.

1450   Li, B., Ryu, Y., Jiang, C., Dechant, B., Liu, J., Yan, Y., and Li, X.: BESSv2.0: A satellite-based and
1451   coupled-process model for quantifying long-term global land–atmosphere fluxes, Remote Sensing of
1452   Environment, 295, 113696, https://doi.org/10.1016/j.rse.2023.113696, 2023a.

1453   Li, M., Cao, S., and Zhu, Z.: Spatiotemporally consistent global dataset of the GIMMS Normalized
1454   Difference Vegetation Index (PKU GIMMS NDVI) from 1982 to 2020, Earth System Science Data
1455   Discussions, 1–31, https://doi.org/10.5194/essd-2023-1, 2023b.

1456   Li, Y.: FLUXNET2015 CN-Ha2 Haibei Shrubland, https://doi.org/10.18140/FLX/1440211, 2016.

1457   Lindauer, M., Steinbrecher, R., Wolpert, B., Mauder, M., and Schmid, H. P.: FLUXNET2015 DE-
1458   Lkb Lackenberg, https://doi.org/10.18140/FLX/1440214, 2016.

1459   Litvak, M.: AmeriFlux AmeriFlux US-FR2 Freeman Ranch- Mesquite Juniper,
1460   https://doi.org/10.17190/AMF/1246054, 2016.

1461   Litvak, M.: AmeriFlux FLUXNET-1F US-Mpj Mountainair Pinyon-Juniper Woodland,
1462   https://doi.org/10.17190/AMF/1832161, 2021.

1463   Litvak, M.: AmeriFlux FLUXNET-1F US-Wjs Willard Juniper Savannah,
1464   https://doi.org/10.17190/AMF/1871146, 2022.

1465   Litvak, M.: AmeriFlux FLUXNET-1F US-Seg Sevilleta grassland,
1466   https://doi.org/10.17190/AMF/1984572, 2023a.

1467   Litvak, M.: AmeriFlux FLUXNET-1F US-Ses Sevilleta shrubland,
1468   https://doi.org/10.17190/AMF/1984573, 2023b.

1469 Litvak, M.: AmeriFlux FLUXNET-1F US-Vcm Valles Caldera Mixed Conifer,
1470 https://doi.org/10.17190/AMF/2229391, 2023c.

1471 Litvak, M.: AmeriFlux FLUXNET-1F US-Vcp Valles Caldera Ponderosa Pine,
1472 https://doi.org/10.17190/AMF/2229392, 2023d.

1473 Liu, L., Zhou, W., Guan, K., Peng, B., Xu, S., Tang, J., Zhu, Q., Till, J., Jia, X., Jiang, C., Wang, S.,
1474 Qin, Z., Kong, H., Grant, R., Mezbahuddin, S., Kumar, V., and Jin, Z.: Knowledge-guided machine
1475 learning can improve carbon cycle quantification in agroecosystems, Nat Commun, 15, 357,
1476 https://doi.org/10.1038/s41467-023-43860-5, 2024.

1477 Liu, Y., Holtzman, N. M., and Konings, A. G.: Global ecosystem-scale plant hydraulic traits retrieved
1478 using model–data fusion, Hydrology and Earth System Sciences, 25, 2399–2417,
1479 https://doi.org/10.5194/hess-25-2399-2021, 2021.

1480 Lohila, A., Aurela, M., Tuovinen, J.-P., Hatakka, J., and Laurila, T.: FLUXNET2015 FI-Jok Jokioinen,
1481 https://doi.org/10.18140/FLX/1440159, 2016.

1482 Lund, M., Jackowicz-Korczyński, M., and Abermann, J.: FLUXNET2015 GL-ZaF Zackenberg Fen,
1483 https://doi.org/10.18140/FLX/1440223, 2016a.

1484 Lund, M., Jackowicz-Korczyński, M., and Abermann, J.: FLUXNET2015 GL-ZaH Zackenberg Heath,
1485 https://doi.org/10.18140/FLX/1440224, 2016b.

1486 Lundberg, S. M. and Lee, S.-I.: A Unified Approach to Interpreting Model Predictions, in: Advances
1487 in Neural Information Processing Systems, 2017.

1488 Luo, X., Zhou, H., Satriawan, T. W., Tian, J., Zhao, R., Keenan, T. F., Griffith, D. M., Sitch, S., Smith,
1489 N. G., and Still, C. J.: Mapping the global distribution of C4 vegetation using observations and
1490 optimality theory, Nat Commun, 15, 1219, https://doi.org/10.1038/s41467-024-45606-3, 2024.

1491 Ma, H. and Liang, S.: Development of the GLASS 250-m leaf area index product (version 6) from
1492 MODIS data using the bidirectional LSTM deep learning model, Remote Sensing of Environment,
1493 273, 112985, https://doi.org/10.1016/j.rse.2022.112985, 2022.

1494 Ma, H., Zeng, J., Chen, N., Zhang, X., Cosh, M. H., and Wang, W.: Satellite surface soil moisture from
1495 SMAP, SMOS, AMSR2 and ESA CCI: A comprehensive assessment using global ground-based
1496 observations, Remote Sensing of Environment, 231, 111215,
1497 https://doi.org/10.1016/j.rse.2019.111215, 2019.

1498 Ma, Y., Zhang, Z., Kang, Y., and Özdoğan, M.: Corn yield prediction and uncertainty analysis based
1499 on remotely sensed variables using a Bayesian neural network approach, Remote Sensing of
1500 Environment, 259, 112408, https://doi.org/10.1016/j.rse.2021.112408, 2021.

1501 Macfarlane, C., Lambert, P., Byrne, J., Johnstone, C., and Smart, N.: FLUXNET2015 AU-Gin Gingin,
1502 https://doi.org/10.18140/FLX/1440199, 2016.

1503 Manca, G. and Goded, I.: FLUXNET2015 IT-PT1 Parco Ticino forest,
1504 https://doi.org/10.18140/FLX/1440172, 2016.

Margolis, H.: AmeriFlux AmeriFlux CA-Qc2 Quebec - 1975 Harvested Black Spruce (HBS75), https://doi.org/10.17190/AMF/1419514, 2018.

Margolis, H. A.: AmeriFlux FLUXNET-1F CA-Qfo Quebec - Eastern Boreal, Mature Black Spruce, https://doi.org/10.17190/AMF/2006960, 2023.

Massman, B.: FLUXNET2015 US-GBT GLEES Brooklyn Tower, https://doi.org/10.18140/FLX/1440118, 2016a.

Massman, B.: FLUXNET2015 US-GLE GLEES, https://doi.org/10.18140/FLX/1440069, 2016b.

Matteucci, G.: FLUXNET2015 IT-Col Collelongo, https://doi.org/10.18140/FLX/1440167, 2016.

McCaughey, H.: AmeriFlux FLUXNET-1F CA-Gro Ontario - Groundhog River, Boreal Mixedwood Forest, https://doi.org/10.17190/AMF/1902823, 2022.

Merbold, L., Rebmann, C., and Corradi, C.: FLUXNET2015 RU-Che Cherski, https://doi.org/10.18140/FLX/1440181, 2016.

Meyer, W., Cale, P., Koerber, G., Ewenz, C., and Sun, Q.: FLUXNET2015 AU-Cpr Calperum, https://doi.org/10.18140/FLX/1440195, 2016.

Meyers, T.: FLUXNET2015 US-Goo Goodwin Creek, https://doi.org/10.18140/FLX/1440070, 2016.

Munger, J. W.: FLUXNET2015 US-Ha1 Harvard Forest EMS Tower (HFR1), https://doi.org/10.18140/FLX/1440071, 2016.

Myneni, R., Knyazikhin, Y., and Park, T.: MCD15A3H MODIS/Terra+Aqua Leaf Area Index/FPAR 4-day L4 Global 500m SIN Grid V006 [Data set], NASA EOSDIS Land Processes DAAC., https://doi.org/10.5067/MODIS/MCD15A3H.006, 2015a.

Myneni, R., Knyazikhin, Y., and Park, T.: MOD15A2H MODIS/Terra Leaf Area Index/FPAR 8-Day L4 Global 500m SIN Grid V006 [Data set], NASA EOSDIS Land Processes DAAC, https://doi.org/10.5067/MODIS/MOD15A2H.006, 2015b.

Nelson, J. A., Walther, S., Gans, F., Kraft, B., Weber, U., Novick, K., Buchmann, N., Migliavacca, M., Wohlfahrt, G., Šigut, L., Ibrom, A., Papale, D., Göckede, M., Duveiller, G., Knohl, A., Hörtnagl, L., Scott, R. L., Zhang, W., Hamdi, Z. M., Reichstein, M., Aranda-Barranco, S., Ardö, J., Op de Beeck, M., Billdesbach, D., Bowling, D., Bracho, R., Brümmer, C., Camps-Valls, G., Chen, S., Cleverly, J. R., Desai, A., Dong, G., El-Madany, T. S., Euskirchen, E. S., Feigenwinter, I., Galvagno, M., Gerosa, G., Gielen, B., Goded, I., Goslee, S., Gough, C. M., Heinesch, B., Ichii, K., Jackowicz-Korczynski, M. A., Klosterhalfen, A., Knox, S., Kobayashi, H., Kohonen, K.-M., Korkiakoski, M., Mammarella, I., Mana, G., Marzuoli, R., Matamala, R., Metzger, S., Montagnani, L., Nicolini, G., O'Halloran, T., Ourcival, J.-M., Peichl, M., Pendall, E., Ruiz Reverter, B., Roland, M., Sabbatini, S., Sachs, T., Schmidt, M., Schwalm, C. R., Shekhar, A., Silberstein, R., Silveira, M. L., Spano, D., Tagesson, T., Tramontana, G., Trotta, C., Turco, F., Vesala, T., Vincke, C., Vitale, D., Vivoni, E. R., Wang, Y., Woodgate, W., Yepez, E. A., Zhang, J., Zona, D., and Jung, M.: X-BASE: the first terrestrial carbon and water flux products

from an extended data-driven scaling framework, FLUXCOM-X, EGUsphere, 1–51, https://doi.org/10.5194/egusphere-2024-165, 2024.

Nouvellon, Y.: FLUXNET2015 CG-Tch Tchizalamou, https://doi.org/10.18140/FLX/1440142, 2016.

Novick, K. and Phillips, R.: AmeriFlux FLUXNET-1F US-MMS Morgan Monroe State Forest, https://doi.org/10.17190/AMF/1854369, 2022.

Oishi, C., Novick, K., and Stoy, P.: AmeriFlux AmeriFlux US-Dk1 Duke Forest-open field, https://doi.org/10.17190/AMF/1246046, 2016a.

Oishi, C., Novick, K., and Stoy, P.: AmeriFlux AmeriFlux US-Dk2 Duke Forest-hardwoods, https://doi.org/10.17190/AMF/1246047, 2016b.

Oishi, C., Novick, K., and Stoy, P.: AmeriFlux AmeriFlux US-Dk3 Duke Forest - loblolly pine, https://doi.org/10.17190/AMF/1246048, 2016c.

O'Sullivan, M., Spracklen, D. V., Batterman, S. A., Arnold, S. R., Gloor, M., and Buermann, W.: Have Synergies Between Nitrogen Deposition and Atmospheric CO_2 Driven the Recent Enhancement of the Terrestrial Carbon Sink?, Global Biogeochemical Cycles, 33, 163–180, https://doi.org/10.1029/2018GB005922, 2019.

O'Sullivan, M., Smith, W. K., Sitch, S., Friedlingstein, P., Arora, V. K., Haverd, V., Jain, A. K., Kato, E., Kautz, M., Lombardozzi, D., Nabel, J. E. M. S., Tian, H., Vuichard, N., Wiltshire, A., Zhu, D., and Buermann, W.: Climate-Driven Variability and Trends in Plant Productivity Over Recent Decades Based on Three Global Products, Global Biogeochemical Cycles, 34, https://doi.org/10.1029/2020GB006613, 2020.

Ourcival, J.-M., Piquemal, K., Joffre, R., and Jean-Marc, L.: FLUXNET2015 FR-Pue Puechabon, https://doi.org/10.18140/FLX/1440164, 2016.

Ozflux, P.: FluxNet Data OzFlux: Australian and New Zealand Flux Research and Monitoring, https://data.ozflux.org.au/portal/pub/viewColDetails.jspx?collection.id=1882723&collection.owne r.id=450&viewType=anonymous, 2024.

Papale, D., Tirone, G., Valentini, R., Arriga, N., Belelli, L., Consalvo, C., Dore, S., Manca, G., Mazzenga, F., Sabbatini, S., Stefani, P., Boschi, A., and Tomassucci, M.: FLUXNET2015 IT-Ro2 Roccarespampani 2, https://doi.org/10.18140/FLX/1440175, 2016.

Pastorello, G., Trotta, C., Canfora, E., Chu, H., Christianson, D., Cheah, Y. W., Poindexter, C., Chen, J., Elbashandy, A., Humphrey, M., Isaac, P., Polidori, D., Ribeca, A., van Ingen, C., Zhang, L., Amiro, B., Ammann, C., Arain, M. A., Ardö, J., Arkebauer, T., Arndt, S. K., Arriga, N., Aubinet, M., Aurela, M., Baldocchi, D., Barr, A., Beamesderfer, E., Marchesini, L. B., Bergeron, O., Beringer, J., Bernhofer, C., Berveiller, D., Billesbach, D., Black, T. A., Blanken, P. D., Bohrer, G., Boike, J., Bolstad, P. V., Bonal, D., Bonnefond, J. M., Bowling, D. R., Bracho, R., Brodeur, J., Brümmer, C., Buchmann, N., Burban, B., Burns, S. P., Buysse, P., Cale, P., Cavagna, M., Cellier, P., Chen, S., Chini, I., Christensen, T. R., Cleverly, J., Collalti, A., Consalvo, C., Cook, B. D., Cook, D., Coursolle, C., Cremonese, E., Curtis, P. S., D'Andrea, E., da Rocha, H., Dai, X., Davis, K. J., De Cinti, B., de Grandcourt, A., De

1579   Ligne, A., De Oliveira, R. C., Delpierre, N., Desai, A. R., Di Bella, C. M., di Tommasi, P., Dolman,
1580   H., Domingo, F., Dong, G., Dore, S., Duce, P., Dufrêne, E., Dunn, A., Dušek, J., Eamus, D.,
1581   Eichelmann, U., ElKhidir, H. A. M., Eugster, W., Ewenz, C. M., Ewers, B., Famulari, D., Fares, S.,
1582   Feigenwinter, I., Feitz, A., Fensholt, R., Filippa, G., Fischer, M., Frank, J., Galvagno, M., Gharun, M.,
1583   Gianelle, D., et al.: The FLUXNET2015 dataset and the ONEFlux processing pipeline for eddy
1584   covariance data, Scientific data, 7, 225, https://doi.org/10.1038/s41597-020-0534-3, 2020.

1585   Pendall, E., Griebel, A., Barton, C., and Metzen, D.: FLUXNET2015 AU-Cum Cumberland Plains,
1586   https://doi.org/10.18140/FLX/1440196, 2016.

1587   Peñuelas, J., Ciais, P., Canadell, J. G., Janssens, I. A., Fernández-Martínez, M., Carnicer, J., Obersteiner,
1588   M., Piao, S., Vautard, R., and Sardans, J.: Shifting from a fertilization-dominated to a warming-
1589   dominated period, Nature Ecology and Evolution, 1, 1438–1445, https://doi.org/10.1038/s41559-
1590   017-0274-8, 2017.

1591   Piao, S., Wang, X., Park, T., Chen, C., Lian, X., He, Y., Bjerke, J. W., Chen, A., Ciais, P., Tømmervik,
1592   H., Nemani, R. R., and Myneni, R. B.: Characteristics, drivers and feedbacks of global greening, Nature
1593   Reviews Earth and Environment, 1, 14–27, https://doi.org/10.1038/s43017-019-0001-x, 2020.

1594   Pilegaard, K. and Ibrom, A.: FLUXNET2015 DK-Eng Enghave,
1595   https://doi.org/10.18140/FLX/1440153, 2016.

1596   Posse, G., Lewczuk, N., Richter, K., and Cristiano, P.: FLUXNET2015 AR-Vir Virasoro, FluxNet;
1597   Instituto Nacional de Tecnología Agropecuaria, https://doi.org/10.18140/FLX/1440192, 2016.

1598   Poveda, F. D., Ballesteros, A. L., Cañete, E. P. S., Ortiz, P. S., Jiménez, M. R. M., Priego, O. P., and
1599   Kowalski, A. S.: FLUXNET2015 ES-Amo Amoladeras, https://doi.org/10.18140/FLX/1440156,
1600   2016.

1601   Prentice, I. C., Dong, N., Gleason, S. M., Maire, V., and Wright, I. J.: Balancing the costs of carbon
1602   gain and water transport: testing a new theoretical framework for plant functional ecology, Ecology
1603   Letters, 17, 82–91, https://doi.org/10.1111/ele.12211, 2014.

1604   Reich, P. B., Hobbie, S. E., and Lee, T. D.: Plant growth enhancement by elevated CO2 eliminated by
1605   joint water and nitrogen limitation, Nature Geoscience, 7, 920–924,
1606   https://doi.org/10.1038/ngeo2284, 2014.

1607   Reichstein, M., Camps-Valls, G., Stevens, B., Jung, M., Denzler, J., Carvalhais, N., and Prabhat: Deep
1608   learning and process understanding for data-driven Earth system science, Nature, 566, 195–204,
1609   https://doi.org/10.1038/s41586-019-0912-1, 2019.

1610   Reverter, B. R., Perez-Cañete, E. S., and Kowalski, A. S.: FLUXNET2015 ES-LgS Laguna Seca,
1611   https://doi.org/10.18140/FLX/1440225, 2016.

1612   Richardson, A. and Hollinger, D.: AmeriFlux FLUXNET-1F US-Bar Bartlett Experimental Forest,
1613   https://doi.org/10.17190/AMF/2006969, 2023.

Ruehr, S., Keenan, T. F., Williams, C., Zhou, Y., Lu, X., Bastos, A., Canadell, J. G., Prentice, I. C., Sitch, S., and Terrer, C.: Evidence and attribution of the enhanced land carbon sink, Nat Rev Earth Environ, 1–17, https://doi.org/10.1038/s43017-023-00456-3, 2023.

Running, S., Mu, Q., and Zhao, M.: MOD17A2H MODIS/Terra Gross Primary Productivity 8-Day L4 Global 500m SIN Grid V006, https://doi.org/10.5067/MODIS/MOD17A2H.006, 2015.

Ryu, Y., Jiang, C., Kobayashi, H., and Detto, M.: MODIS-derived global land products of shortwave radiation and diffuse and total photosynthetically active radiation at 5 km resolution from 2000, Remote Sensing of Environment, 204, 812–825, https://doi.org/10.1016/j.rse.2017.09.021, 2018.

Ryu, Y., Berry, J. A., and Baldocchi, D. D.: What is global photosynthesis? History, uncertainties and opportunities, Remote Sensing of Environment, 223, 95–114, https://doi.org/10.1016/j.rse.2019.01.016, 2019.

Sabater, J. M.: ERA5-Land monthly averaged data from 1981 to present., Copernicus Climate Change Service (C3S) Climate Data Store (CDS), https://doi.org/doi:10.24381/cds.68d2bb30, 2019.

Sabbatini, S., Arriga, N., Papale, D., Boschi, A., and Tomassucci, M.: FLUXNET2015 IT-CA1 Castel d'Asso1, https://doi.org/10.18140/FLX/1440230, 2016a.

Sabbatini, S., Arriga, N., Gioli, B., Papale, D., Boschi, A., and Tomassucci, M.: FLUXNET2015 IT-CA2 Castel d'Asso2, https://doi.org/10.18140/FLX/1440231, 2016b.

Sabbatini, S., Arriga, N., Matteucci, G., Papale, D., Boschi, A., and Tomassucci, M.: FLUXNET2015 IT-CA3 Castel d'Asso 3, https://doi.org/10.18140/FLX/1440232, 2016c.

Saleska, S.: FLUXNET2015 BR-Sa1 Santarem-Km67-Primary Forest, https://doi.org/10.18140/FLX/1440032, 2016.

Schaaf, C. and Wang, Z.: MCD43C4 MODIS/Terra+Aqua BRDF/Albedo Nadir BRDF-Adjusted Ref Daily L3 Global 0.05Deg CMG V006 [Data set], NASA EOSDIS Land Processes DAAC., https://doi.org/10.5067/MODIS/MCD43C4.006, 2015.

Schneider, K. and Schmidt, M.: FLUXNET2015 DE-Seh Selhausen, https://doi.org/10.18140/FLX/1440217, 2016.

Schroder, I., Zegelin, S., Palu, T., and Feitz, A.: FLUXNET2015 AU-Emr Emerald, https://doi.org/10.18140/FLX/1440198, 2016.

Schwalm, C. R., Anderegg, W. R. L., Michalak, A. M., Fisher, J. B., Biondi, F., Koch, G., Litvak, M., Ogle, K., Shaw, J. D., Wolf, A., Huntzinger, D. N., Schaefer, K., Cook, R., Wei, Y., Fang, Y., Hayes, D., Huang, M., Jain, A., and Tian, H.: Global patterns of drought recovery, Nature, 548, 202–205, https://doi.org/10.1038/nature23021, 2017.

Scott, R.: FLUXNET2015 US-SRM Santa Rita Mesquite, https://doi.org/10.18140/FLX/1440090, 2016a.

1648 Scott, R.: FLUXNET2015 US-Whs Walnut Gulch Lucky Hills Shrub,
1649 https://doi.org/10.18140/FLX/1440097, 2016b.

1650 Shao, C.: FLUXNET2015 CN-Sw2 Siziwang Grazed (SZWG),
1651 https://doi.org/10.18140/FLX/1440212, 2016.

1652 Sigut, L., Havrankova, K., Jocher, G., Pavelka, M., Janouš, D., Czerny, R., Stanik, K., and Trusina, J.:
1653 FLUXNET2015 CZ-BK2 Bily Kriz grassland, https://doi.org/10.18140/FLX/1440144, 2016.

1654 Smith, W. K., Reed, S. C., Cleveland, C. C., Ballantyne, A. P., Anderegg, W. R. L., Wieder, W. R., Liu,
1655 Y. Y., and Running, S. W.: Large divergence of satellite and Earth system model estimates of global
1656 terrestrial CO2 fertilization, Nature Climate Change, 6, 306–310,
1657 https://doi.org/10.1038/nclimate2879, 2016.

1658 Spano, D., Duce, P., Marras, S., Sirca, C., Arca, A., Zara, P., Ventura, A., Mereu, S., and Sanna, L.:
1659 FLUXNET2015 IT-Noe Arca di Noe - Le Prigionette, https://doi.org/10.18140/FLX/1440171,
1660 2016.

1661 Staebler, R.: AmeriFlux FLUXNET-1F CA-Cbo Ontario - Mixed Deciduous, Borden Forest Site,
1662 https://doi.org/10.17190/AMF/1854365, 2022.

1663 Ștefan, V. and Levin, S.: plotbiomes: R package for plotting Whittaker biomes with ggplot2, ,
1664 https://doi.org/10.5281/zenodo.7145245, 2018.

1665 Still, C. J., Berry, J. A., Collatz, G. J., and DeFries, R. S.: Global distribution of C3 and C4 vegetation:
1666 Carbon cycle implications, Global Biogeochemical Cycles, 17,
1667 https://doi.org/10.1029/2001gb001807, 2003.

1668 Still, C. J., Berry, J. A., Collatz, G. J., and DeFries, R. S.: ISLSCP II C4 Vegetation Percentage, in: Hall,
1669 Forrest G., G. Collatz, B. Meeson, S. Los, E. Brown de Colstoun, and D. Landis (eds.). ISLSCP
1670 Initiative II Collection. Data set., http://dx.doi.org/10.3334/ORNLDAAC/932, 2009.

1671 Stocker, B. D., Zscheischler, J., Keenan, T. F., Prentice, I. C., Peñuelas, J., and Seneviratne, S. I.:
1672 Quantifying soil moisture impacts on light use efficiency across biomes, New Phytologist, 218, 1430–
1673 1449, https://doi.org/10.1111/nph.15123, 2018.

1674 Stocker, B. D., Zscheischler, J., Keenan, T. F., Prentice, I. C., Seneviratne, S. I., and Peñuelas, J.:
1675 Drought impacts on terrestrial primary production underestimated by satellite monitoring, Nature
1676 Geoscience, 12, 264–270, https://doi.org/10.1038/s41561-019-0318-6, 2019.

1677 Stocker, B. D., Tumber-Dávila, S. J., Konings, A. G., Anderson, M. C., Hain, C., and Jackson, R. B.:
1678 Global patterns of water storage in the rooting zones of vegetation, Nat. Geosci., 16, 250–256,
1679 https://doi.org/10.1038/s41561-023-01125-2, 2023.

1680 Sturtevant, C., Szutu, D., Baldocchi, D., Matthes, J. H., Oikawa, P., and Chamberlain, S. D.:
1681 FLUXNET2015 US-Myb Mayberry Wetland, https://doi.org/10.18140/FLX/1440105, 2016.

1682 Suyker, A.: FLUXNET2015 US-Ne1 Mead - irrigated continuous maize site,
1683 https://doi.org/10.18140/FLX/1440084, 2016a.

Suyker, A.: FLUXNET2015 US-Ne2 Mead - irrigated maize-soybean rotation site, https://doi.org/10.18140/FLX/1440085, 2016b.

Suyker, A.: FLUXNET2015 US-Ne3 Mead - rainfed maize-soybean rotation site, https://doi.org/10.18140/FLX/1440086, 2016c.

Tagesson, T., Ardö, J., and Fensholt, R.: FLUXNET2015 SN-Dhr Dahra, https://doi.org/10.18140/FLX/1440246, 2016.

Tang, Y., Kato, T., and Du, M.: FLUXNET2015 CN-HaM Haibei Alpine Tibet site, https://doi.org/10.18140/FLX/1440190, 2016.

Terrer, C., Jackson, R. B., Prentice, I. C., Keenan, T. F., Kaiser, C., Vicca, S., Fisher, J. B., Reich, P. B., Stocker, B. D., Hungate, B. A., Peñuelas, J., McCallum, I., Soudzilovskaia, N. A., Cernusak, L. A., Talhelm, A. F., Van Sundert, K., Piao, S., Newton, P. C. D., Hovenden, M. J., Blumenthal, D. M., Liu, Y. Y., Müller, C., Winter, K., Field, C. B., Viechtbauer, W., Van Lissa, C. J., Hoosbeek, M. R., Watanabe, M., Koike, T., Leshyk, V. O., Polley, H. W., and Franklin, O.: Nitrogen and phosphorus constrain the CO2 fertilization of global plant biomass, Nature Climate Change, 9, 684–689, https://doi.org/10.1038/s41558-019-0545-2, 2019.

Thoning, K. W., Crotwell, A. M., and Mund, J. W.: Atmospheric Carbon Dioxide Dry Air Mole Fractions from continuous measurements at Mauna Loa, Hawaii, Barrow, Alaska, American Samoa and South Pole. 1973-2020, Version 2021-08-09, National Oceanic and Atmospheric Administration (NOAA), Global Monitoring Laboratory (GML), Boulder, Colorado, USA, https://doi.org/10.15138/yaf1-bk21, 2021.

Tramontana, G., Ichii, K., Camps-Valls, G., Tomelleri, E., and Papale, D.: Uncertainty analysis of gross primary production upscaling using Random Forests, remote sensing and eddy covariance data, Remote Sensing of Environment, 168, 360–373, https://doi.org/10.1016/j.rse.2015.07.015, 2015.

Tramontana, G., Jung, M., Schwalm, C. R., Ichii, K., Camps-Valls, G., Ráduly, B., Reichstein, M., Arain, M. A., Cescatti, A., Kiely, G., Merbold, L., Serrano-Ortiz, P., Sickert, S., Wolf, S., and Papale, D.: Predicting carbon dioxide and energy fluxes across global FLUXNET sites with regression algorithms, Biogeosciences, 13, 4291–4313, https://doi.org/10.5194/bg-13-4291-2016, 2016.

Ueyama, M., Iwata, H., and Harazono, Y.: AmeriFlux AmeriFlux US-Uaf University of Alaska, Fairbanks, https://doi.org/10.17190/AMF/1480322, 2018.

Ueyama, M., Ichii, K., Kobayashi, H., Kumagai, T., Beringer, J., Merbold, L., Euskirchen, E. S., Hirano, T., Marchesini, L. B., Baldocchi, D., Saitoh, T. M., Mizoguchi, Y., Ono, K., Kim, J., Varlagin, A., Kang, M., Shimizu, T., Kosugi, Y., Bret-Harte, M. S., Machimura, T., Matsuura, Y., Ohta, T., Takagi, K., Takanashi, S., and Yasuda, Y.: Inferring CO2 fertilization effect based on global monitoring land-atmosphere exchange with a theoretical model, Environmental Research Letters, 15, 84009, https://doi.org/10.1088/1748-9326/ab79e5, 2020.

Valach, A., Shortt, R., Szutu, D., Eichelmann, E., Knox, S., Hemes, K., Verfaillie, J., and Baldocchi, D.: AmeriFlux FLUXNET-1F US-Tw1 Twitchell Wetland West Pond, https://doi.org/10.17190/AMF/1832165, 2021.

Valentini, R., Nicolini, G., Stefani, P., de Grandcourt, A., and Stivanello, S.: FLUXNET2015 GH-Ank Ankasa, https://doi.org/10.18140/FLX/1440229, 2016a.

Valentini, R., Dore, S., Mazzenga, F., Sabbatini, S., Stefani, P., Tirone, G., and Papale, D.: FLUXNET2015 IT-Cpz Castelporziano, https://doi.org/10.18140/FLX/1440168, 2016b.

Valentini, R., Tirone, G., Vitale, D., Papale, D., Arriga, N., Belelli, L., Dore, S., Manca, G., Mazzenga, F., Pegoraro, E., Sabbatini, S., Stefani, P., Boschi, A., and Tomassucci, M.: FLUXNET2015 IT-Ro1 Roccarespampani 1, https://doi.org/10.18140/FLX/1440174, 2016c.

Villarreal, S. and Vargas, R.: Representativeness of FLUXNET Sites Across Latin America, Journal of Geophysical Research: Biogeosciences, 126, e2020JG006090, https://doi.org/10.1029/2020JG006090, 2021.

Walker, A. P., De Kauwe, M. G., Bastos, A., Belmecheri, S., Georgiou, K., Keeling, R. F., McMahon, S. M., Medlyn, B. E., Moore, D. J. P., Norby, R. J., Zaehle, S., Anderson-Teixeira, K. J., Battipaglia, G., Brienen, R. J. W., Cabugao, K. G., Cailleret, M., Campbell, E., Canadell, J. G., Ciais, P., Craig, M. E., Ellsworth, D. S., Farquhar, G. D., Fatichi, S., Fisher, J. B., Frank, D. C., Graven, H., Gu, L., Haverd, V., Heilman, K., Heimann, M., Hungate, B. A., Iversen, C. M., Joos, F., Jiang, M., Keenan, T. F., Knauer, J., Körner, C., Leshyk, V. O., Leuzinger, S., Liu, Y., MacBean, N., Malhi, Y., McVicar, T. R., Penuelas, J., Pongratz, J., Powell, A. S., Riutta, T., Sabot, M. E. B., Schleucher, J., Sitch, S., Smith, W. K., Sulman, B., Taylor, B., Terrer, C., Torn, M. S., Treseder, K. K., Trugman, A. T., Trumbore, S. E., van Mantgem, P. J., Voelker, S. L., Whelan, M. E., and Zuidema, P. A.: Integrating the evidence for a terrestrial carbon sink caused by increasing atmospheric CO_2, New Phytologist, 229, 2413–2445, https://doi.org/10.1111/nph.16866, 2021.

Walther, S., Besnard, S., Nelson, J. A., El-Madany, T. S., Migliavacca, M., Weber, U., Carvalhais, N., Ermida, S. L., Brümmer, C., Schrader, F., Prokushkin, A. S., Panov, A. V., and Jung, M.: Technical note: A view from space on global flux towers by MODIS and Landsat: the FluxnetEO data set, Biogeosciences, 19, 2805–2840, https://doi.org/10.5194/bg-19-2805-2022, 2022.

Wan, Z., Hook, S., and Hulley, G.: MOD11A1 MODIS/Terra Land Surface Temperature/Emissivity Daily L3 Global 1km SIN Grid V006 [Data set], NASA EOSDIS Land Processes DAAC, https://doi.org/10.5067/MODIS/MOD11A1.006, 2015a.

Wan, Z., Hook, S., and Hulley, G.: MYD11A1 MODIS/Aqua Land Surface Temperature/Emissivity Daily L3 Global 1km SIN Grid V006 [Data set], NASA EOSDIS Land Processes DAAC, https://doi.org/10.5067/MODIS/MYD11A1.006, 2015b.

Wang, H. and Fu, X.: FLUXNET2015 CN-Qia Qianyanzhou, https://doi.org/10.18140/FLX/1440141, 2016.

Wang, H., Prentice, I. C., Keenan, T. F., Davis, T. W., Wright, I. J., Cornwell, W. K., Evans, B. J., and Peng, C.: Towards a universal model for carbon dioxide uptake by plants, Nature Plants, 3, 734–741, https://doi.org/10.1038/s41477-017-0006-8, 2017.

Warm Winter 2020 Team: Warm Winter 2020 ecosystem eddy covariance flux product for 73 stations in FLUXNET-Archive format—release 2022-1 (Version 1.0), https://doi.org/10.18160/2G60-ZHAK, 2022.

Wenzel, S., Cox, P. M., Eyring, V., and Friedlingstein, P.: Projected land photosynthesis constrained by changes in the seasonal cycle of atmospheric CO2, Nature, 538, 499–501, https://doi.org/10.1038/nature19772, 2016.

Wohlfahrt, G., Hammerle, A., and Hörtnagl, L.: FLUXNET2015 AT-Neu Neustift, https://doi.org/10.18140/FLX/1440121, 2016.

Wolf, S., Eugster, W., and Buchmann, N.: FLUXNET2015 PA-SPn Sardinilla Plantation, https://doi.org/10.18140/FLX/1440180, 2016.

Woodgate, W., van Gorsel, E., Leuning, R., Hughes, D., Kitchen, M., and Zegelin, S.: FLUXNET2015 AU-Tum Tumbarumba, https://doi.org/10.18140/FLX/1440126, 2016.

Xiao, J., Zhuang, Q., Baldocchi, D. D., Law, B. E., Richardson, A. D., Chen, J., Oren, R., Starr, G., Noormets, A., Ma, S., Verma, S. B., Wharton, S., Wofsy, S. C., Bolstad, P. V., Burns, S. P., Cook, D. R., Curtis, P. S., Drake, B. G., Falk, M., Fischer, M. L., Foster, D. R., Gu, L., Hadley, J. L., Hollinger, D. Y., Katul, G. G., Litvak, M., Martin, T. A., Matamala, R., McNulty, S., Meyers, T. P., Monson, R. K., Munger, J. W., Oechel, W. C., Paw U, K. T., Schmid, H. P., Scott, R. L., Sun, G., Suyker, A. E., and Torn, M. S.: Estimation of net ecosystem carbon exchange for the conterminous United States by combining MODIS and AmeriFlux data, Agricultural and Forest Meteorology, 148, 1827–1847, https://doi.org/10.1016/j.agrformet.2008.06.015, 2008.

Xie, X., Chen, J. M., Yuan, W., Guan, X., Jin, H., and Leng, J.: A Practical Algorithm for Correcting Topographical Effects on Global GPP Products, Journal of Geophysical Research: Biogeosciences, 128, e2023JG007553, https://doi.org/10.1029/2023JG007553, 2023.

Xie, Y., Gibbs, H. K., and Lark, T. J.: Landsat-based Irrigation Dataset (LANID): 30m resolution maps of irrigation distribution, frequency, and change for the US, 1997–2017, Earth System Science Data, 13, 5689–5710, https://doi.org/10.5194/essd-13-5689-2021, 2021.

Yan, K., Park, T., Yan, G., Chen, C., Yang, B., Liu, Z., Nemani, R. R., Knyazikhin, Y., and Myneni, R. B.: Evaluation of MODIS LAI/FPAR product collection 6. Part 1: Consistency and improvements, Remote Sensing, 8, 1–16, https://doi.org/10.3390/rs8050359, 2016a.

Yan, K., Park, T., Yan, G., Liu, Z., Yang, B., Chen, C., Nemani, R. R., Knyazikhin, Y., and Myneni, R. B.: Evaluation of MODIS LAI/FPAR product collection 6. Part 2: Validation and intercomparison, Remote Sensing, 8, 460, https://doi.org/10.3390/rs8060460, 2016b.

Yang, F., Ichii, K., White, M. A., Hashimoto, H., Michaelis, A. R., Votava, P., Zhu, A. X., Huete, A., Running, S. W., and Nemani, R. R.: Developing a continental-scale measure of gross primary production by combining MODIS and AmeriFlux data through Support Vector Machine approach, Remote Sensing of Environment, 110, 109–122, https://doi.org/10.1016/j.rse.2007.02.016, 2007.

Yang, R., Wang, J., Zeng, N., Sitch, S., Tang, W., McGrath, M. J., Cai, Q., Liu, D., Lombardozzi, D., Tian, H., Jain, A. K., and Han, P.: Divergent historical GPP trends among state-of-the-art multi-model simulations and satellite-based products, Earth System Dynamics, 13, 833–849, https://doi.org/10.5194/esd-13-833-2022, 2022.

1798 Yuan, H., Dai, Y., Xiao, Z., Ji, D., and Shangguan, W.: Reprocessing the MODIS Leaf Area Index
1799 products for land surface and climate modelling, Remote Sensing of Environment, 115, 1171–1187,
1800 https://doi.org/10.1016/j.rse.2011.01.001, 2011.

1801 Zeng, J., Matsunaga, T., Tan, Z.-H., Saigusa, N., Shirai, T., Tang, Y., Peng, S., and Fukuda, Y.: Global
1802 terrestrial carbon fluxes of 1999–2019 estimated by upscaling eddy covariance data with a random
1803 forest, Sci Data, 7, 313, https://doi.org/10.1038/s41597-020-00653-5, 2020.

1804 Zeng, N., Zhao, F., Collatz, G. J., Kalnay, E., Salawitch, R. J., West, T. O., and Guanter, L.: Agricultural
1805 Green Revolution as a driver of increasing atmospheric CO2 seasonal amplitude, Nature, 515, 394–
1806 397, https://doi.org/10.1038/nature13893, 2014.

1807 Zhan, C., Orth, R., Migliavacca, M., Zaehle, S., Reichstein, M., Engel, J., Rammig, A., and Winkler, A.
1808 J.: Emergence of the physiological effects of elevated CO2 on land–atmosphere exchange of carbon
1809 and water, Global Change Biology, 28, 7313–7326, https://doi.org/10.1111/gcb.16397, 2022.

1810 Zhang, J. and Han, S.: FLUXNET2015 CN-Cha Changbaishan,
1811 https://doi.org/10.18140/FLX/1440137, 2016.

1812 Zhang, Y.: A global spatially contiguous solar-induced fluorescence (CSIF) dataset using neural
1813 networks (2000-2020), National Tibetan Plateau Data Center,
1814 https://doi.org/10.11888/Ecolo.tpdc.271751., 2021.

1815 Zhang, Y., Joiner, J., Hamed Alemohammad, S., Zhou, S., and Gentine, P.: A global spatially
1816 contiguous solar-induced fluorescence (CSIF) dataset using neural networks, Biogeosciences, 15,
1817 5779–5800, https://doi.org/10.5194/bg-15-5779-2018, 2018.

1818 Zhang, Y., Kong, D., Gan, R., Chiew, F. H. S., McVicar, T. R., Zhang, Q., and Yang, Y.: Coupled
1819 estimation of 500 m and 8-day resolution global evapotranspiration and gross primary production in
1820 2002–2017, Remote Sensing of Environment, 222, 165–182,
1821 https://doi.org/10.1016/j.rse.2018.12.031, 2019.

1822 Zheng, Y., Shen, R., Wang, Y., Li, X., Liu, S., Liang, S., Chen, J. M., Ju, W., Zhang, L., and Yuan, W.:
1823 Improved estimate of global gross primary production for reproducing its long-Term variation, 1982-
1824 2017, Earth System Science Data, 12, 2725–2746, https://doi.org/10.5194/essd-12-2725-2020, 2020.

1825 Zhou, G. and Yan, J.: FLUXNET2015 CN-Din Dinghushan,
1826 https://doi.org/10.18140/FLX/1440139, 2016.

1827 Zhu, Z., Piao, S., Myneni, R. B., Huang, M., Zeng, Z., Canadell, J. G., Ciais, P., Sitch, S., Friedlingstein,
1828 P., Arneth, A., Cao, C., Cheng, L., Kato, E., Koven, C., Li, Y., Lian, X., Liu, Y., Liu, R., Mao, J., Pan,
1829 Y., Peng, S., Peuelas, J., Poulter, B., Pugh, T. A. M., Stocker, B. D., Viovy, N., Wang, X., Wang, Y.,
1830 Xiao, Z., Yang, H., Zaehle, S., and Zeng, N.: Greening of the Earth and its drivers, Nature Climate
1831 Change, 6, 791–795, https://doi.org/10.1038/nclimate3004, 2016.

1832 Zhuang, J., dussin, raphael, Huard, D., Bourgault, P., Banihirwe, A., Raynaud, S., Malevich, B.,
1833 Schupfner, M., Filipe, Levang, S., Gauthier, C., Jüling, A., Almansi, M., RichardScottOZ, RondeauG,
1834 Rasp, S., Smith, T. J., Stachelek, J., Plough, M., Pierre, Bell, R., Caneill, R., and Li, X.: xESMF: v0.8.2, ,
1835 https://doi.org/10.5281/zenodo.8356796, 2023.

1836 Zona, D. and Oechel, W.: FLUXNET2015 US-Atq Atqasuk, 1837 https://doi.org/10.18140/FLX/1440067, 2016a.

1838 Zona, D. and Oechel, W.: FLUXNET2015 US-Ivo Ivotuk, https://doi.org/10.18140/FLX/1440073, 1839 2016b.

1840